Prototype studies and CFD Simulations towards the CBM-RICH air cooling system

Master Thesis
zur Erlangung des akademischen Grades
Master of Science im Fach Physik

der Fakultät Mathematik und Naturwissenschaften
Fachgruppe Physik
der Bergischen Universität Wuppertal

vorgelegt von
Gianluca Boccarella
(geboren in Wuppertal)

November 2023

1. Gutachter:
Prof. Dr. Karl-Heinz Kampert
Bergische Universität Wuppertal

2. Gutachter:
Prof. Dr. Christian Zeitnitz
Bergische Universität Wuppertal

Betreuer:
Dr. Christian Pauly
Bergische Universität Wuppertal

Contents

List of Figures

List of Tables

Acronyms

ADP Air distribution plate. ii, iii, 23, 28, 30, 33, 36, 37, 40, 42, 44–49, 52–58, 60, 63, 65, 67, 68, 70

BKPL backplane. 50, 52, 59, 60, 63, 66

CBM Compressed Baryonic Matter. ii, 1–3, 5, 7, 19–22, 24, 25, 27, 28, 30, 62, 70

CFD Computational Fluid Dynamics. ii, 1, 14, 16–18, 23, 40, 42, 47, 70, 71

CTA Constant Temperature Anemometry. ii, 30, 31, 45

FAIR Facility for Antiproton and Ion Research. ii, 2–4, 70

FEB Front-end board. ii, iii, 24–26, 60, 63, 76, 78, 79, 84

FPGA Field programmable gate array. 25

FVM Finite Volume Method. 18, 73

GSI Gesellschaft für Schwerionenforschung. 1, 2, 70

GUI Graphical user interface. 27–29, 62

HADES High-Acceptance Dielectron Spectrometer. 1, 24

MAF Mass air flow. ii, iii, 1, 28–32, 34–39, 41, 42, 44–49, 52–54, 57, 58, 62–64, 66–68, 70–72

MAPMT MultiAnode Photomultiplier tube. 7, 8, 20–22, 24, 25, 64, 70

PMT Photomultiplier tube. 6–8, 24

QCD Quantum chromodynamics. ii, 1, 2, 4, 5

QGP Quark Gluon Plasma. 2, 4, 5

RANS Reynolds-averaged Navier-Stokes equations. 12, 13, 18

RICH Ring-imaging Cherenkov Detector. ii, 1, 3, 5, 7, 19–22, 24, 25, 27, 28, 30, 62, 70

TI Turbulent intensity. 71

TKE Turbulent kinetic energy. 41, 71

Abstract

This thesis describes the development and investigation of concepts for the CBM-RICH air cooling system by means of a full-size prototype. It includes the calibration of mass air flow sensors and their application to determine air flow at several locations inside the camera. Based on the experimental results, suggestions are made for a homogenization concept of the air flow which is accompanied by computational fluid dynamics (CFD) simulations. The cooling concept is assessed on the basis of the measured heat dissipation of a fully equipped and commissioned camera column.

Kurzfassung

Diese Thesis beschreibt die Entwicklung und die Untersuchung von Konzepten für das CBM-RICH Luftkühlungssystem anhand eines Kameraprototypen. Sie umfasst die Kalibrierung von sogenannten Luftmassenmessern und deren Anwendung zur Bestimmung des Luftstroms an verschiedenen Stellen im Inneren der Kamera. Basierend auf den experimentellen Ergebnissen werden Vorschläge für ein Homogenisierungskonzept des Luftstroms gemacht, welche auf Computational Fluid Dynamics (CFD) Simulationen gestützt sind. Das Kühlungskonzept wird auf Basis der gemessenen Wärmeabgabe einer vollständig bestückten und inbetriebgenommenen Kameraspalte bewertet.

„Kühner als das Unbekannte zu erforschen, kann es sein, das Bekannte zu bezweifeln.“

Alexander von Humboldt

1

Introduction and Motivation

The early Universe consisted of the smallest particles that make up our nowadays visible matter. The Standard Model of particle physics is one of the most successful theories at all. It describes the three fundamental interactions of elementary particles. Many unresolved questions about what matter looks like under extreme conditions, how hadrons formed and the intricacies of the mechanisms of the strong interaction can be studied in heavy ion collisions. Ring-imaging Cherenkov (RICH) detectors can play a crucial role in studying the hot and dense matter at very early stages after collision as they probe decay and even direct electrons that are principally unaffected by strong interactions. Hence, they come directly from the fireball and can therefore be called ideal messengers of the quark-gluon plasma. Particle detectors like the RICH need to be cooled as heat produced by the highly integrated readout electronics can lead to unwanted noise or even to damages. The HADES-RICH detector at GSI does not come with a sophisticated cooling system. One of the main motivations of this work is to remedy this shortcoming for the CBM-RICH detector. Close coordination between experiment and simulation work aims to design an optimized cooling concept that takes into account the largest possible number of effects.

Outline

The main goal of the Compressed Baryonic Matter experiment is to investigate a specific regime in the QCD phase diagram. The concept of the experiment, the main scientific objectives, and the role played by the Ring-Imaging Cherenkov (RICH) detector are presented in chapter 2. The detector will be cooled by a sophisticated closed-cycle air cooling system. In physics, air is considered a fluid. The statics and the dynamics of fluids is summed up in the research field of fluid mechanics. All types of fluid flows, a mathematical treatment of their motion and the connection to computational fluid dynamics (CFD) simulation is taken up in chapter 3. More details about the experimental setup, especially the RICH detector in the CBM cave and its prototype model at the test stand of the university, are discussed in chapter 4. Large scale experiments can be controlled and monitored by a dedicated slow control interface. The development of a slow control system for the test stand is discussed in chapter 5. The air flow in large-scale systems is a classical engineering problem. It is commonly measured with so-called mass air flow (MAF) sensors. Two types of MAF sensors are used to measure the inlet and the outlet MAF of the camera prototype. Their working principle, the calibration procedure and the results are shown in chapter 6. The results of all air flow measurements and simulations for different scenarios in the air distribution plate and in a single column, as well as the commissioning of one fully operated column of the camera and its heat dissipation, will be investigated and interpreted in chapter 7.

2

The Compressed Baryonic Matter Experiment

The Compressed Baryonic Matter (CBM) experiment at the Facility for Antiproton and Ion Research (FAIR), an expansion of the GSI Helmholtz Centre for Heavy Ion Research in Darmstadt (cf. Fig. 2.2b), aims to study the QCD phase diagram and especially rare observables at high net baryon densities in heavy ion collisions. This is of scientific interest since matter at these conditions is likely to be found in the interior of neutron stars and at the center of supernova explosions. Not being build yet and still under construction, the CBM detector setup shown in Fig. 2.2a will measure both hadrons (p, π, K, vector mesons like ρ, ω, ϕ, multistrange hyperons and charmed mesons) and leptons (e, μ) in a fixed target experiment. The central collision of two gold nuclei being accelerated takes place in the SIS100 synchrotron with beam energies of between 2 and 11 AGeV, whereas protons can reach up to 29 GeV. All these observables bear directly or indirectly information on quarkyonic matter created in the early phase of the collision: strangeness and charmness (Kaons, hyperons, D mesons/charmonium, existence of metastable dibaryons and more concretely the ratio of J/Ψ to open charm is interesting), the existence of a first order transition or the critical endpoint (direct photons) etc. The highly dense baryonic matter generated as a result of this collision, often referred as *fire ball*, consists, among other things, of vector mesons which decay themselves into dileptons (pairs of electrons and positrons, respectively positively and negatively charged muons). CBM will measure at high reaction rates of up to 10 MHz in order to provide high statistics for the low production cross section (about 1000 per event) of the rare probes that are of main interest, which is one of its specialties. Reason being is that di-leptons and direct photons probe the QGP in very early stages after the collision as they are emitted quite near the collision point and decouple from strong interaction processes which make them ideal messengers. Ultra fast triggering systems and electronics for data acquisition as well as extreme radiation hard detectors are crucial and they come along with online event selection and reconstruction tools. The particle tracks are measured by the Silicon Tracking System (STS), a system of eight layers of double-sided micro-strip sensors placed downstream of the target in a magnetic dipole field of 1 Tm bending power generated by a superconducting dipole magnet. The main task of the STS-system, achieving a momentum resolution of $\frac{\Delta p}{p} = 1\%$, is track reconstruction and momentum determination of charged particles with multiplicities up to 600 per event within detector acceptance. Hadrons are investigated by Multi-Gap Resistive Plate Chambers (MGRPC) via TOF measurements whereas short-lived secondary vertex particles like open charmed mesons such as D^0 which decay into kaons and pions via weak interaction are measured by a Micro-Vertex-Detector (MVD). It enables the requirement of extremely high vertex reconstruction resolution for an open charm detection that separates primary from short-lived decay vertices and comprises two layers of Monolithic Active Pixel Sensors (MAPS) before

Figure 2.1: Logo of CBM. [23]

the target and a third MAPS layer behind the target. Just as valid as for the STS system, the material budget has to be particularly low to increase the resolution and to minimize photon conversion for the dilepton measurements. The CBM experiment will be capable to measure both electrons and muons. A Ring-Imaging Cherenkov (RICH) detector will identify electrons and positrons and additionally suppress pions in the region below 8 GeV/c. It is additionally supported by Transition Radiation Detectors (TRD) in order to improve electron identification at high momenta of 5–6 GeV. The Muon Chamber (MUCH) system will analyze the muons, but in a separate experimental setup with no RICH detector in operation. Currently, an amount of six hadron absorber (iron) layers of different thicknesses are planned, as well as 15–18 gaseous tracking chambers placed in a triplet-like arrangement behind each iron layer. Muons have little energy loss when penetrating material because they are minimally ionizing particles that, unlike electrons and positrons, do not produce electromagnetic showers due to Bremsstrahlung and pair production at the energies considered. Hence they will be detected after the alternating system of segmented hadron absorbers and tracking detector planes in between the gaps. The huge particle density per event poses a major challenge for track reconstruction. The detector development therefore focuses on granular gaseous detector technologies: Gas Electron Multipliers (GEM) will be placed in between the absorber plates. Their operating principle is based on large electric fields created in small gas-filled holes of a thin polymer sheet where avalanches of electrons are initiated by ionizing radiation. Direct photons and photons from neutral meson decays (π^0, η) will be investigated by a shashlik-type Electromagnetic Calorimeter (ECAL). The particles lose their energy inside the scintillating material by atom excitation and subsequent light production. A Forward Spectator Detector (FSD) is installed to evaluate the reaction plane and looks for non-interacting nucleons of the collisions. It consists of a full-compensating modular lead-scintillator where the scintillation light is guided through wavelength shifting fibers (WLS) and read out by Multi-Avalanche Photo-Diodes (MAPD).

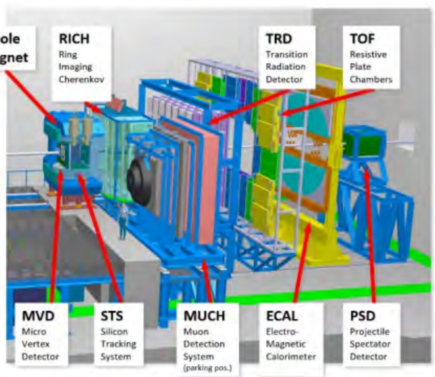

(a) As an initial phase of the dense QCD matter research the CBM detector will be operated alternatively with the HADES detector at low SIS100 energies which can provide reference measurements for the study of cold nuclear matter. HADES is a large-polar-angle acceptance detector optimized for high-precision measurements of electron-positron pairs but also photons, hadrons and strange hyperons. It is run at the SIS18 accelerator and will be shifted to the CBM cave for investigation of several observables in vicinity of the deconfinement phase transition by proton and heavy ion collisions. [9]

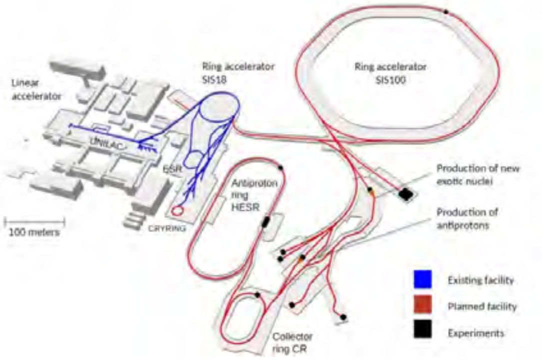

(b) The future Facility of Antiproton and Ion Research. With the new SIS100 ring accelerator, built at a depth of down to 17 meters and with a circumference of 1100 m, it will be able to accelerate ions of all natural elements. Superconducting magnets with liquid helium keep the particles on track. They are either led directly to the experiments or shot at a target to produce further exotic particles (secondary particles). They then enter experiment and storage rings, where they are either sorted and analyzed, or can make further circulations in the sense of multiple use. [26]

Figure 2.2: Layout of the CBM experiment and the FAIR facility in Darmstadt.

2.1 Quark-Gluon Plasma (QGP) and Color Superconductivity

There are several reasons for the importance and curiosity of scientists to study nuclear matter at extreme conditions. Some of them will be briefly discussed in the following, starting first with some theoretical aspects. Quantum chromodynamics (QCD) is a non-abelian gauge theory (quantum field theory) with symmetry group SU(3). It is a theoretical model of the strong interaction and describes how quarks and gluons, fundamentally color-charged particles, interact with each other. In hot and dense phases of matter the quarks and gluons of different colors become deconfined and are no longer confined within individual hadrons as the strong interaction weakens and no longer prohibits them to exist as free and isolated particles with long-range interaction.

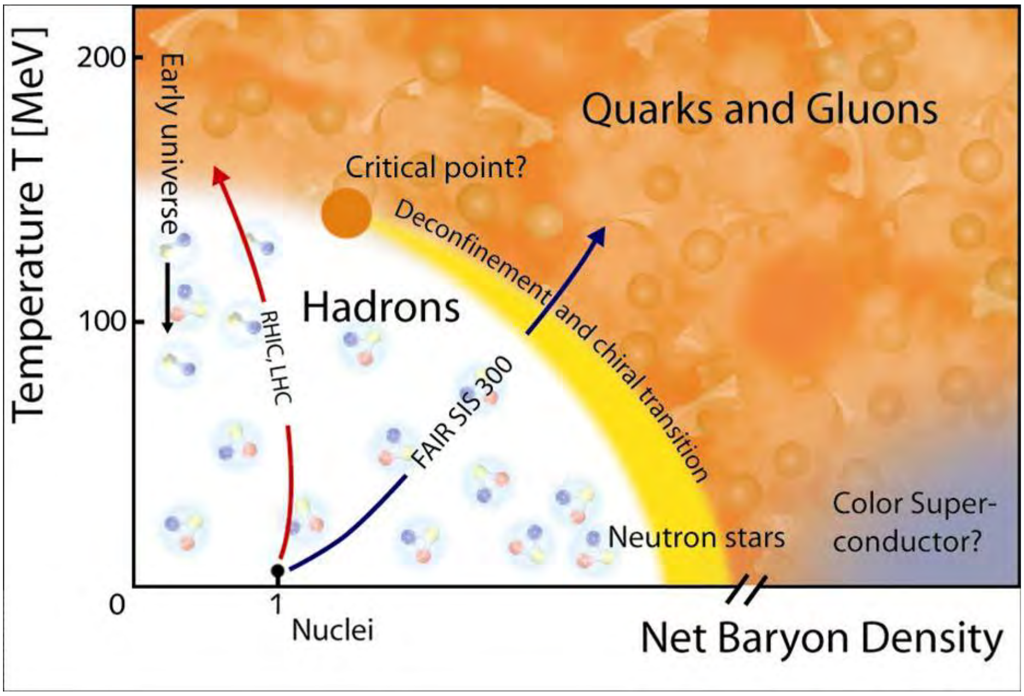

Figure 2.3: The QCD Phase Diagram: temperature plotted against net baryon density (or sometimes baryon chemical potential μ_B). Several phase transitions of different orders are to be expected between the phases of QCD matter. Normal nuclei are found at $\mu_{B,net} = 1$ ($\mu_B = 924$ MeV) and a temperature slightly above 0 MeV. From this point (black dot) experimentalists can start exploring the whole phase diagram. A smooth cross-over to the QGP (quarks are deconfined and chiral symmetry is restored) is expected from lattice calculations for vanishing baryon density and high temperatures and is investigated by RHIC and LHC research programs. Further, a first order phase transition is to be expected at moderate net baryon densities. Both phenomenons considered together, this inevitably leads to the prediction of a critical point (orange blob). Hadron gas and QGP can exist in coexisting phase. This is what SPS and FAIR experiments focus on and beam energies of 10-40 AGeV are required. In the asymptotically high net baryon density limit and low temperatures a color superconducting phase is awaited. [4]

In this region of the phase diagram a first order (deconfinement) phase transition between hadronic and partonic matter is conjectured and it would be of large scientific relevance to prove its existence [43]. Further, by studying hadrons in this dense matter regime it could provide insight into the alleged restoration of the chiral symmetry, the origin of hadron masses and the equation-of-state (EOS) of nuclear matter at neutron star core densities. Massless quark matter is considered to be totally symmetric with respect to chirality, i.e. matter is balanced with antimatter. However, in QCD vacuum (ground state) the chiral symmetry is spontaneously broken just as the moment of hadron freeze-out after the Big Bang. This results in the occurrence of Goldstone bosons (pions) with non-vanishing mass due to the explicit symmetry breaking by quark masses and large mass splitting of chiral-partner states in the light hadron spectrum [40]. But if $T \gg \Lambda_{QCD}$ there must occur a crossover (quantified by the expectation value of the antiquark-quark scalar or chiral condensate $\langle q\bar{q}\rangle$, which is the order parameter of broken chiral symmetry, cf. [8]) into an equilibrium state regime where chiral symmetry is not broken anymore. This occurs at $T_c \sim \Lambda_{QCD} \approx 170$ MeV, similar to the Curie point in ferromagnets. This critical temperature is produced in lead-on-lead collisions at the CERN-SPS. After this phase transition, the newly emerged state of matter is considered to be an assembly of nearly massless quarks and gluons at thermal and close to chemical equilibrium which is known as quark-gluon plasma (QGP) or quark soup in a more popular scientific way. Condensates of kaons and a large abundance of hyperons are expected within the QGP.

The extremely short-lived matter states can be probed in the QCD phase diagram (cf. Fig. 2.3) by varying the beam energy in heavy ion collisions (e.g. Au + Au) as the net baryon density is dependent upon temperature. First theories of the QGP were developed in the 1970s and first experiments were designed in the 1980s for the Large Hadron Collider (LHC) at CERN and the Relativistic Heavy Ion Collider (RHIC) at BNL. Finally in 2000, the quark gluon plasma was detected in an experiment for the first time at CERN [29]. To sum up: there are many reasons why the study of QGP and color superconductivity is interesting for scientists: a better understanding of the early Universe in its first fractions of seconds (hot QGP), the formation of matter and a better conception of the strong force. One of the only conceivable natural environments with these extreme temperature and density conditions required for this type of quark matter to occur is a neutron star and the core of a supernova explosion (cold QGP).

2.2 The Ring-Imaging Cherenkov (RICH) Detector

In order to identify electrically charged particles one can use a Ring-imaging Cherenkov (RICH) detector. The identification goes along with the characterisation of the particle velocity. When an electrically charged particle crosses a dielectric medium with a velocity $c_n = c_0/n$ that is greater than the speed of light in this medium, it emits photons in a certain angle with respect to its propagation path. The CBM-RICH camera will be filled with CO_2 radiator gas at room pressure in which photons achieve a velocity of $0.9995\,c$ which is slightly less than the velocity of the electrons ($v = 0.9999\,c$). Pions ($v = 0.90 - 0.99\,c$) below the Cherenkov threshold of 4.65 GeV/c are not fast enough to produce Cherenkov light, meaning that in case of its detection one can conclude the identity of the particle, namely electrons or positrons. On a microscopic scale, the charged particles polarize the atoms asymmetrically because their motion and the polarization effect are of the same order of magnitude in time (cf. Fig. 2.4a). This results in a continuous emission of conical electromagnetic shock waves of neighboring atoms that interfere constructively as the formation of the dipoles in the direction of flight can no longer develop fast enough. Contrarily, if the particle is comparably slow to the medium speed of light, the polarization is symmetric and the local polarizations shield each other on a global scale. This effect is known as Cherenkov effect,

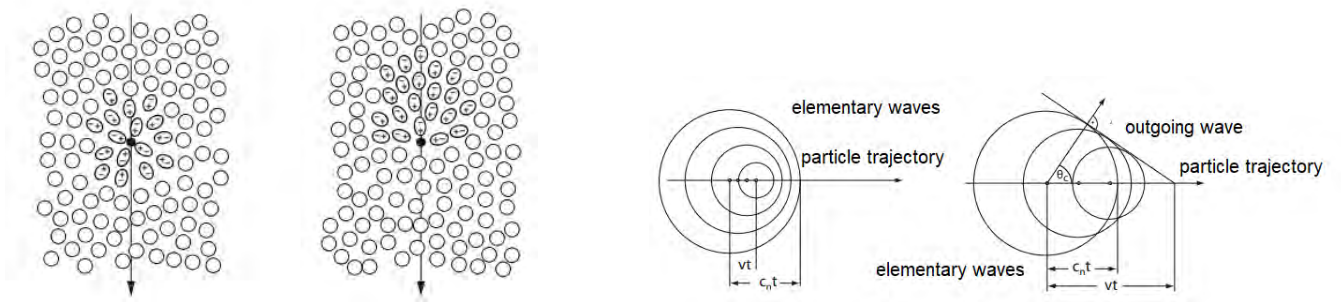

(a) (b)

Figure 2.4: The Cherenkov Effect. (a) shows the polarization of the atoms in the dielectric medium whereas (b) demonstrates the formation of Cherenkov light in the Huygen's principle of wavefronts. Modified and taken out of [31].

published by Pavel Alekseyevich Cherenkov in 1937 [15, 16] and quantum mechanically described by I. Frank and I. Tamm [25]. The so-called Cherenkov angle is a velocity-dependent measure for the size of the cone that is produced (cf. Fig. 2.4b):

$$\cos\theta_c = \frac{\frac{c_0}{n} \cdot t}{v \cdot t} = \frac{1}{n\beta} \Longleftrightarrow \beta = \frac{1}{n\cos\theta_c}, \tag{2.1}$$

where n is the refractive index of the optical transparent medium and $\beta = \frac{v}{c}$. An additional condition for Cherenkov radiation is that the radiation wavelength has to be smaller than the size of the radiator medium ($\lambda \ll L$). The emitted radiation is transversally and linearly polarized. Eq. 2.1 inherently defines a threshold velocity $\beta_{thr} = \frac{1}{n}$, a maximum angle $\cos(\theta_{max}) = \frac{1}{n}$ for the cone and thus a threshold energy $\frac{E_0}{m_0 c^2} = \gamma_{thr} = \frac{n}{\sqrt{n^2-1}} = \frac{1}{\beta_{thr}} = \frac{1}{\sin\theta_{max}}$ as well as a threshold momentum $P_{thr} = m_0 c^2 (\beta\gamma)_{thr} = \frac{mc^2}{\sqrt{n^2-1}}$. The cone can be mapped as a sharp ring onto a photon detector surface using parabolic focusing mirrors (cf. Fig. 2.5a & 2.5b). The ring radius can be influenced by the focal length f of the mirrors which itself depends on the mirror radius r_s and informs about the Cherenkov angle θ_c:

$$r_c = f \cdot \theta_c = \frac{r_s \cdot \theta_c}{2} \Longleftrightarrow \beta = \frac{1}{n\cos(\frac{2r_c}{r_s})}, \tag{2.2}$$

This means, by measuring the radius of the ring one can determine the velocity of the particle and through the momentum one can eventually identify the particle by its mass:

$$p = \beta\gamma \cdot mc \Longleftrightarrow m = \sqrt{\frac{1}{\beta^2} - 1} \cdot \frac{p}{c} \overset{(2.2)}{=} \frac{p}{c} \cdot \sqrt{n^2 \cos^2\left(\frac{2r_c}{r_s}\right) - 1} \tag{2.3}$$

where $\gamma = \frac{1}{\sqrt{1-\beta^2}}$ is the Lorentz factor. The Cherenkov radiation that is created inside the dielectric medium is slightly disperse. The light rays are focused by spherical mirrors to generate a sharp spot on the photo detector plane. For additional optimization of the ring sharpness the camera can also be built curved instead of being flat in order to more closely follow the spherical focal plane of the mirror system. A challenging aspect is that each electron traversing the RICH radiator emits in the order of 100 photons but due to limited quantum efficiency of the MAPMTs only around 25 photons are detected. Therefore they need to be resolved accurately in space and time. An efficient way to measure the Cherenkov photons is to use photomultiplier tubes (PMTs). They even allow single photon

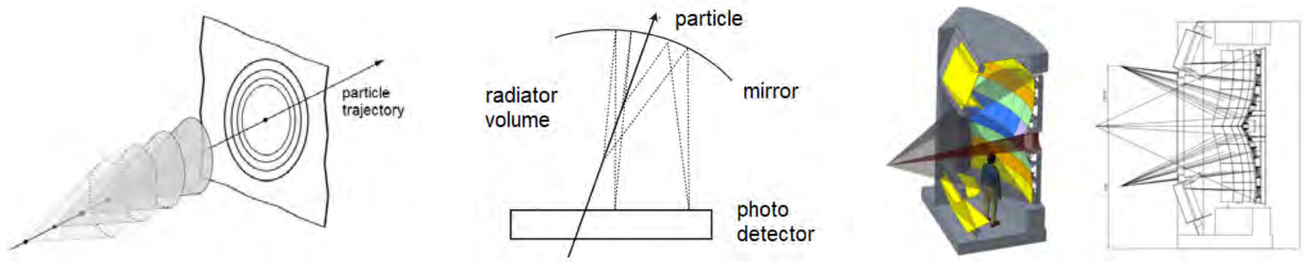

(a) Cherenkov cones with different opening angles θ_c can be mapped as rings with different radii onto a plane detector. Modified and taken out of [33].

(b) Focusing of the disperse Cherenkov radiation inside the radiator volume by a spherical or parabolic mirror onto a photo detector. Modified and taken out of [33].

(c) Model drawing of the upper and lower CBM-RICH cameras in side view and sketch of proximity focusing concept with parabolic mirrors. Taken out of [42].

Figure 2.5: Working principle of a RICH detector.

detection and are generally low-noise. The operating principle of a PMT is as follows: photons incident on the photocathode, which is vapor-deposited on a bialkali layer on the inside of the glass window in a vacuum tube, release electrons through the photoelectric effect. The photoelectrons are directed and focused by a high voltage onto a system of dynodes and an anode (a so-called secondary electron multiplier). Increasing voltages are applied to the electrodes by a voltage divider for proper acceleration of the electrons which impinge on the first dynode. This leads to an avalanche-like emission of secondary electrons successively at each dynode until they reach the anode and can be further processed as an electrical signal (cf. Fig. 2.6a). A single photo electron is typically amplified by 10^5–10^7, resulting in an electric pulse equivalent to a few hundred femto coulombs. The quantum efficiency (probability to produce a photoelectron) is settled around 10–30% and is dependent on wavelength, entry window material (often borosilicate) and photocathode (usually bialkali or multialkali compounds). However, a single photomultiplier is not sufficient to determine the ring radius. For a spatially resolved measurement of the photons, MultiAnode PhotoMultipliers (MAPMT) is used instead. They essentially differ from normal PMTs in the segmentation of the anode into several anode pads and the special metal channel structure of the dynode system. The focusing electrodes are now arranged as a focusing mesh. Fig. 2.6b shows the trajectory of the electrons inside a dynode channel.

The design of this detector type is quite compact: the spread of the secondary electrons is small. Additionally, the gap between the dynode stage is not too large and by having more dynode channels than anode pads one can reduce the track length of the electrons. This allows the detection of the incident light position with high accuracy and the amplification as well as the time resolution are independent on the incidence point of the photon. MAPMTs can have different anode patterns. The pads can either be aligned linearly or arranged in a matrix structure. The CBM experiment has chosen the 8×8 pixel H12700 MAPMT from HAMAMATSU as a photon detector for electron identification and pion suppression. The MAPMTs are coupled to a self-triggering readout electronics. Especially mentionable is that 428 pieces have already been installed in the HADES- RICH detector. The expected photon yield in the CBM-RICH detector is in the order of 20–25 detected photons per Cherenkov ring, with up to 50–100 simultaneous Cherenkov rings (mostly from conversion electrons) per central Au+Au collision. Pion suppression is at about 1000 for momenta $\leq$ 10 GeV/c and up to 10^4 when combining the RICH information with the TRD and MGRPC information. A total of 1100 units are used to equip the RICH

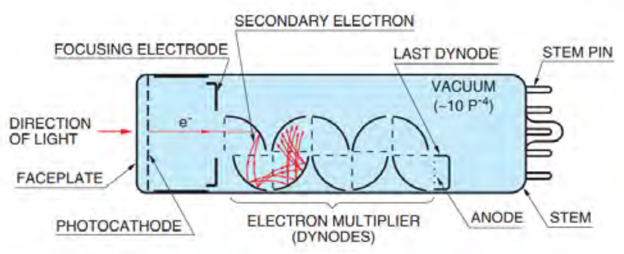

(a) PMT: a photon releases an electron of the photocathode which gets accelerated to the first dynode and produces an avalanche of secondary electrons at multiple dynodes.

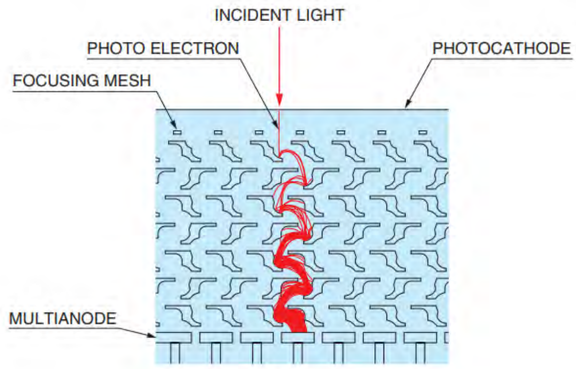

(b) MAPMT: using the same concept for secondary electron production, now the anode is segmented into multiple pads and the dynodes are now a system of several metal channels.

Figure 2.6: Working principle of photomultiplier tubes (a) and MultiAnode PhotoMultipliers (b). [50]

camera. They have a rectangular shape with a size of 52×52 mm^2 and a pixel size of 6×6 mm^2 which results in an effective area of 87% and a total of around 64.000 detection pixels. The photons can be measured with a precision of 300 picoseconds by each pixel and that 100.000 times per seconds. The quantum efficiency of the photocathode is around 33% at 350 nm. The entrance window is made up of UV glass instead of borosilicate glass leading to an enhancement in wavelength transmission down to 185 nm and a more robust radiation hardness. If one assumes a maximum hit rate of 700 kHz/pixel and a gain of 10^6 for single photons this results in a signal current of 0.1 µA/pixel or ∼ 5 µA per MAPMT. The special readout electronics were made in-house. It is made of 2000 electronic modules, each of them having 32 readout channels. This will be discussed more in detail in chapter 4.

The heat loss generated by the electronics is dissipated via a specially developed closed-cycle air cooling system which is the objective of this thesis. One part represents the development of air distribution masks specially made to suit the peculiarities of the system to homogenize the air flows, aiming to cool the electronics uniformly.

3

Fluid Mechanics

In the following chapter, some terminology of the different classifications of fluid flows is presented. Different turbulence models are discussed, as well as the implementation of the Navier-Stokes equations in CFD simulations.

3.1 Fluids

A fluid can be defined as a liquid, gas or some other material that, in comparison to a solid, continuously moves or deforms (flows) as long as an external force or shear stress is applied [20], hence lacking the ability to offer permanent resistance to a deforming force and to resume its original shape. The shear stress is defined as the force acting tangentially per unit area $\tau = F/A$ and causes a deformation which is measured by the angle ϕ (shear strain). It is developed by the movement of fluid particles with different velocities relative to each other and has different behavior for solids as for liquids and gases [39]. Moreover, it is related to the rate of the strain via the (dynamic) **viscosity** μ:

$$\tau = \mu \frac{du}{dy}, \tag{3.1}$$

where du/dy is the change of velocity u of a particle in a direction (y) perpendicular to the propagation. In general, μ is a function of temperature and pressure and no shear stress exists in rest state. Eq. 3.1 is also known as Newtons law of viscosity. The ratio of dynamic viscosity to mass ρ density is known as kinematic viscosity ν:

$$\nu = \frac{\mu}{\rho}. \tag{3.2}$$

All forces present in a fluid are perpendicular to the plane upon which they act. This means for example when a fluid is in contact with a boundary it will adapt to this layer and have the same velocity. Among fluids, there is a large variation of behaviors regarding shear stresses. Fluids obeying Eq. 3.1 are classified as Newtonian fluids whereas fluids with non-constant viscosity μ are so-called non-Newtonian fluids. An ideal fluid is assumed to have no viscosity and hence no shear stresses at all (cf. Fig, 3.1a). In some problems the consideration of an ideal fluid can be useful to find a realistic solution. Further, liquids and gases, both being fluids, can be distinguished with respect to their compressibility. Liquids are considered to be **incompressible** as they occupy fixed volumes whereas gases are regarded as **compressible** as they do not form a free surface and expand as long as they are not being restricted by any limiting vessel. Generally, a fluid is called compressible if its density changes with pressure. Sometimes (for steady air flows, see below), it can be useful to declare a compressible flow an incompressible one if

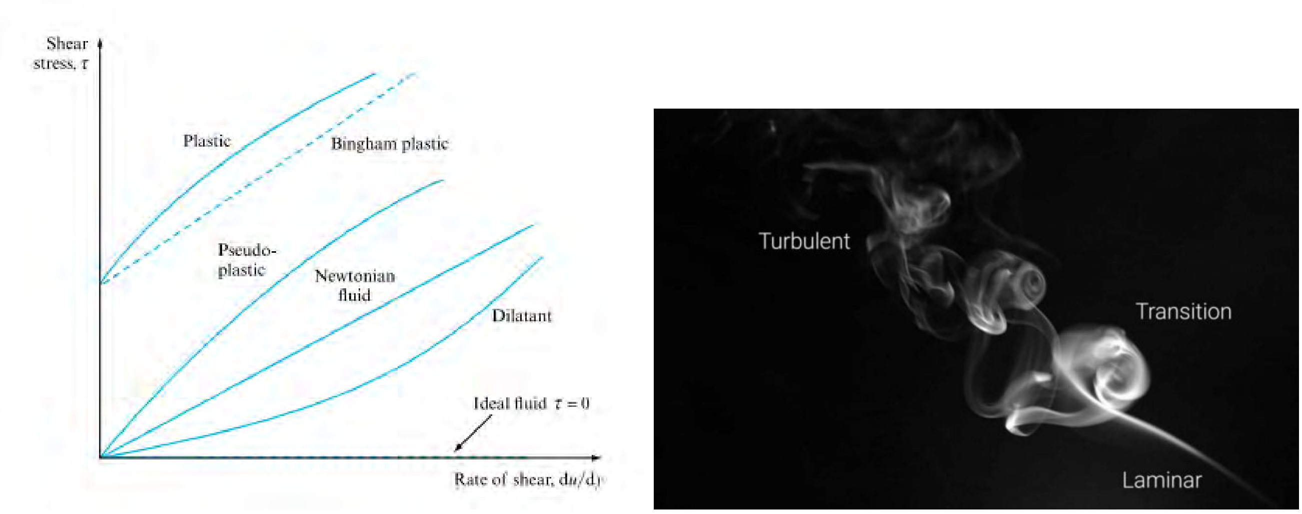

(a) Newtonian and non-Newtonian fluids in a shear stress versus rate of shear diagram. [20]

(b) Illustration of laminar, transition and turbulent flow in a smoke trail. [30]

Figure 3.1: Classification of flow types.

the changes in density are sufficiently small. Vice versa for unsteady liquid flows (see below), it can happen that the compressibility of liquids should be considered due to high pressure differences. One final thought has to be made about the general concept of fluids. Physicswise, they are built up of a large and complex molecular structure. Since it would be very idle to take into consideration all the effects coming along with molecular motion, fluids are hypothetically thought of a continuum. One can look at a point with fixed physical quantities (velocity, pressure) and its surrounding domain of air molecules, which should be larger than the intramolecular distance, and average each quantity over this exact domain. Variations can be regarded to occur smoothly from point to point. When analyzing fluid flow, one might stumble over the term streamlines. They are imaginary curves in the fluid at a given instant where there is no flow and their tangent vectors constitute the velocity field of the flow. Further, they either extend to infinity upstream and downstream or they build a closed curve. A streamtube is a collection of adjacent streamlines from where the fluid cannot escape as it behaves like an imaginary pipe. Looking at the statics and dynamics of the system, fluid flow can be further categorized. **Uniform** flows have the same direction and magnitude of velocity at any given point, whereas **non-uniform** flows do not. Moreover, if the change of velocity, pressure and cross-section depends not only on position but also on time the flow is described as **unsteady**, while **steady** flows are time-independent. If the fluid flows uninterruptedly in parallel layers then it is called **laminar** flow. However, if the changes in pressure and flow velocity are chaotic and excessive kinetic energy dominates the damping effect of the fluid's viscosity, the flow becomes **turbulent**. A distinction between viscous and turbulent flows can be made: disturbances in particle motion that lead the particle to change its direction are compensated by viscous forces of the surrounding fluid and hence the particles still tend to adapt the motion of the stream. For turbulent flows the viscous forces are outbid by inertial forces. For this reason, the ratio of inertial to viscous forces is a measure of whether the flow is turbulent or not. This measure is called Reynolds number Re. Turbulent flows usually are characterized by their unsteady vortices and eddies that by interacting with each other cause drag inside the fluid (cf. Fig, 3.1b). This would mean that more energy would be required to pump the fluid through a pipe. Turbulent flows have more characterizing features like diffusivity, rotationality and dissipation. Due to the irregularity of turbulent flows, their small fluctuations in velocity and pressure are treated statistically. This will be discussed in section 3.2. Fluid flows can be treated in different dimensions. The properties of one-dimensional flows depend only on the direction of flow propagation while two-dimensional flows additionally account for the direction perpendicular to it. In fluid mechanics the discharge is a measure of the amount of flow (either volume or mass) going through a cross-section. In pipe flows (cf. section 3.3 for more details) the fluid velocity at a wall will adapt the velocity of the wall itself and form a velocity profile with layers of different velocities towards the center in a so-called boundary layer. In these cases the velocity of the fluid u strongly depends on the radius r of the pipe. For some problems this might be not relevant and one can take the mean velocity $\bar{u}$ which is defined as the volume rate of discharge $Q = A \cdot u$ divided by the cross-section area A normal to the stream:

$$\bar{u} = \frac{Q}{A} \quad \text{or} \quad \bar{u} = \frac{\dot{m}}{\rho \cdot A} \tag{3.3}$$

The dynamics of a fluid is described by the stresses inside the fluid, and in contrast to the static case of frictionless fluids, additional tangential stresses are expected when friction is taken into account.

Navier-Stokes equations

The motion of fluids can be described by a set of three equations: mass conservation, momentum conservation and energy conservation. This set is known as Navier-Stokes equations. The energy equation describes the change of internal heat or temperature with time. The continuity equation describes the mass conservation of fluids. It states that all the mass of fluid entering in a control volume per unit time must equal the outgoing mass of fluid per unit time plus the increase of mass fluid in the control volume per unit time. It is

$$\frac{\partial}{\partial x}(\rho u_x) + \frac{\partial}{\partial y}(\rho u_y) + \frac{\partial}{\partial_z}(\rho u_z) = \nabla \cdot (\rho \mathbf{u}) = -\frac{\partial \rho}{\partial t} \tag{3.4}$$

for compressible and

$$\nabla \cdot \mathbf{u} = 0 \tag{3.5}$$

for incompressible flows due to $\nabla \rho = 0$, no matter if steady or unsteady. The momentum equations for compressible and incompressible flows are derived by considering two additional forces on an infinitesimal cuboid control volume acting parallel (shear stresses τ) and perpendicular (normal stresses σ) to the surface where air flow enters. Special assumptions for the shear stress tensor in the Cauchy equation lead finally to:

$$\rho \frac{D\mathbf{u}}{Dt} = \begin{cases} -\nabla p + \mu \nabla \{[\nabla \mathbf{u} + (\nabla \mathbf{u})^T] - \frac{2}{3}(\nabla \cdot \mathbf{u}) I\} + \mathbf{F}, \\ -\nabla p + \mu \nabla^2 \mathbf{u} + \mathbf{F}, \end{cases} \tag{3.6}$$

for compressible respectively incompressible flows and where p is the mean normal stress, $\mathbf{F}$ is the external body force and $\rho \frac{\partial \mathbf{u}}{\partial t} + (\rho \mathbf{u} \cdot \nabla)\mathbf{u} := \rho \frac{D\mathbf{u}}{Dt}$. They are non-linear partial differential equations of second order. Although the friction terms are small compared to the other terms, they are crucial in order to describe the adhesion of wall boundary conditions. For inviscid fluids μ is set to zero as well and the Euler equation is obtained such that in the bottom equation in Eq. 3.6 the second term vanishes.

From the incompressible Navier-Stokes equations the Reynolds number can be derived by making the components of the equation dimensionless. The result is

$$Re = \frac{\rho u L}{\mu}, \tag{3.7}$$

where L is a characteristic length. Turbulent flows occur if the Reynolds number exceeds a critical value which is most commonly set to $Re_{crit} = 2300$ in literature. However, one should mention that for special conditions laminar flow can still be produced for Reynolds numbers that exceed this critical value.

3.2 Turbulence

Although turbulence describes the chaotic motion of fluids it can be described mathematically. Depending on the underlying situation, different effects can be considered in different models. In fluid flow simulations the modeling of inlet flows plays a crucial role.

3.2.1 Reynolds-averaged Navier-Stokes Equations (RANS)

Turbulence involves high Reynolds numbers which make it nearly impossible to solve the Navier-Stokes equations with a reasonable computational expenditure. In order to approximate turbulent air flow as properly as possible, one can use a common method developed by Osborne Reynolds. The idea is to assign each quantity an average value and a fluctuation value (cf. Fig, 3.2a). The choice of the mean value is taken such that the fluctuation value cancels out on average. One can choose between either *Reynolds averaging* for small periods of time or *ensemble averaging* especially used for unsteady flows. Averaging induces additional terms in the Navier-Stokes equations, corresponding to turbulent air flow, which has to be described by a certain turbulence model introducing additional equations to close the set. Since only average values appear in the equations, the partial time derivatives will vanish if the solution is converged to steady state. The accuracy of the solution depends on the averaging length and therefore on the duration of the simulation. The RANS method is commonly used in industry since most engineering problems deal with time-averaged properties of air flow. One starts with the so-called Reynolds decomposition, subdividing the instantaneous velocity and pressure (u_i, p_i) into time-averaged values ($\bar{u}_i$, $\bar{p}_i$) and fluctuation values (u'_i, p'_i):

$$u_i = \bar{u}_i + u'_i \qquad \text{and} \qquad p_i = \bar{p}_i + p'_i \tag{3.8}$$

where

$$\bar{u}_i = \frac{1}{\Delta t} \int_t^{t+\Delta t} u_i \, dt \tag{3.9}$$

and analogously for $\bar{p}_i$. These measures are plugged into the Navier-Stokes equations for turbulent and incompressible flow and finally one obtains the Reynolds-averaged continuity and Reynolds-averaged

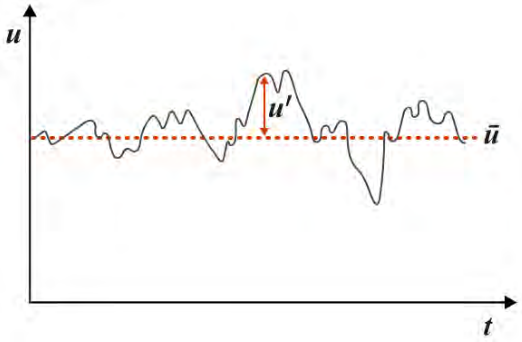

(a) Velocity fluctuations in a turbulent flow signal: u is the instantaneous velocity and is decomposed into an averaged value $\bar{u}$ and a fluctuation value u'.

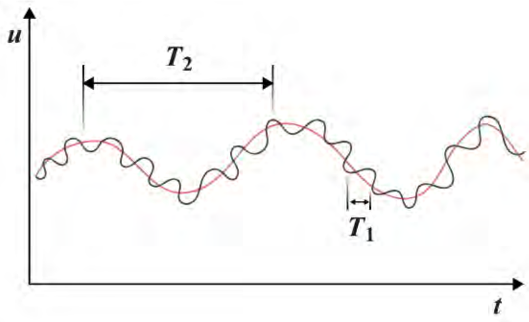

(b) Unsteady case of the RANS equation: the large scale oscillation $T2$ should be larger than the turbulent time scale $T1$.

Figure 3.2: The concept of Reynolds averaging. [6]

momentum equations:

$$\frac{\partial \rho}{\partial t} + \frac{\partial(\rho \bar{u}_j)}{\partial x_j} = 0 \tag{3.10}$$

$$\frac{\partial(\rho \bar{u}_i)}{\partial t} + \frac{\partial(\rho \bar{u}_i \bar{u}_j)}{\partial x_j} = -\frac{\partial}{\partial x_j}\left[\bar{p}\delta_{ij} + 2\mu \bar{S}_{ij} + \tau_{ij}^R\right] \tag{3.11}$$

with $\bar{S}_{ij} = \frac{1}{2}(\frac{\partial \bar{u}_i}{\partial x_j} + \frac{\partial u_j}{\partial x_i})$ the mean strain rate tensor and $\tau_{ij} = -\rho\overline{u_i' u_j'}$ the Reynolds stress tensor. With the knowledge of approximate turbulent flow properties these equations enable to give time-averaged solutions of the corresponding Navier-Stokes equations to the given problem. However, the first term of the momentum equation is still unsteady: a time-derivative of the mean value of the velocity appears. By ignoring this term one can model only steady flows whereas by considering this term one can simulate unsteady flows if the time scale for large scale motions (T2) is larger than the time averaging period (T1). Also in this case the computation of the instantaneous field is no longer needed as it is replaced by the Reynolds decomposition (red curve in Fig, 3.2b). But one has introduced another unknown term instead which is related to an additional stress to the turbulence. Its computation is quite challenging and one must solve it in terms of a mean flow. By assuming that the Reynolds stress and the mean rate of the strain tensor are related linearly to each other (so-called Boussinesq approximation), one can write down the Reynolds stress tensor as follows:

$$\tau_{ij}^R = \mu_t\left[\frac{\partial \bar{u}_i}{\partial x_j} + \frac{\partial \bar{u}_j}{\partial x_i} - \frac{2}{3}\frac{\partial \bar{u}_k}{\partial x_k}\delta_{ij}\right] - \frac{2}{3}\rho k \delta_{ij} \tag{3.12}$$

where μ_t is the eddy viscosity and $k = \frac{1}{2}\overline{u_i' u_j'}$ is the turbulent kinetic energy per unit mass. The only unknown in this equation is the eddy viscosity. It can be determined by one of the turbulence models.

3.2.2 Turbulence Models

Turbulence models can be categorized in their wave number range within the energy spectrum. Accordingly, their computational requirements can be higher or lower. In general, the transport equations of turbulence models can be written as [5]:

$$\underbrace{\frac{\partial(\rho\phi)}{\partial t}}_{\text{Unsteady}} + \underbrace{\frac{\partial(\rho\bar{u}_j\phi)}{\partial x_j}}_{\text{Convection}} = \underbrace{\frac{\partial}{\partial x_j}\left[(\mu + \frac{\mu_t}{\sigma})\frac{\partial\phi}{\partial x_j}\right]}_{\text{Diffusion}} + \underbrace{P_\phi}_{\text{Production}} + \underbrace{D_\phi}_{\text{Dissipation}} \tag{3.13}$$

where ϕ is a turbulence model variable which is *transported* in space and time. The left-hand side of the equation refers to the advection comprising a time-dependent acceleration term and a convection term while the components of the right-hand side are related to diffusion (summation of material and eddy viscosity), production of turbulent variables from the mean flow gradient and dissipation of turbulent variables as a consequence of viscous stresses. There is a whole range of RANS models that essentially differ in the number of transport equations [7].

k-ε Model

The k-ε turbulence model is one of the most common models used in CFD calculations [2, 36]. Containing basically two partial differential equations, it describes the flow characteristics by means of two transport variables: k is the turbulent kinetic energy and ε is the dissipation rate of the turbulent kinetic energy [34]. For further details of the transport equation, please refer to the relevant literature. The k-ε model is a quite simple model because it sets only the requirement of initial and boundary conditions. It can be applied for recirculating flows and for systems with shear layers that have low pressure gradients. On the other hand it shows bad performance for inlets and compressors, systems with large pressure gradients, non-confined and rotating flows, curved boundary layers and flows in non-circular ducts.

k-ω Models

The Standard (Wilcox) k-ω model accounts for low-Reynolds-number effects, compressibility and shear flow spreading. The transport parameters are the turbulence kinetic energy k and the specific dissipation rate ω which can be understood as the ratio of k to ε [49]. F. R. Menter improved this model which is a combination of the k-ω and k-ε formulations and is known as Shear-Stress Transport (SST) k-ω model. The standard k-ω model is used in the inner region of the boundary layer (near-wall region) whereas k-ε is used in free shear flow and free-stream independencies in the far-field are taken into account [3, 37]. It is commonly used in engineering problems, especially where large pressure gradients occur, or in problems with freestream. The transport equations are very similar to those of the k-ω model. Some modifications are done to the production of k, to the turbulent viscosity, to the Prandtl numbers and a cross-diffusion term of k and ε which is called D_ω is added.

3.2.3 Inlet Turbulence Modeling

Once the turbulence model is chosen, a specification of turbulence parameters is required to run CFD simulations. This concerns especially the inlet boundaries. For the abovementioned k-ε- and k-ω models these variables are the turbulent kinetic energy and the eddy dissipation rate. These measures can be characterized either by available measurement data or one can estimate them by means of other turbulence parameters that can be calculated. More precisely, these are the turbulence intensity I, the turbulence length scale and the eddy viscosity ratio. The turbulence intensity describes the ratio between the RMS of the turbulent velocity fluctuations u' and the mean velocity $\bar{u}$ - both measures are known from the Reynolds decomposition:

$$I = \frac{u'}{\bar{u}} \tag{3.14}$$

where $u' = \sqrt{\frac{u_x'^2+u_y'^2+u_z'^2}{3}} = \sqrt{\frac{2k}{3}}$ and $\bar{u} = \sqrt{(\bar{u}_x^2 + \bar{u}_y^2 + \bar{u}_z^2)}$. With raw measurement data it is not possible to evaluate the turbulence intensity through this formula. Instead there is an expression for fully developed internal flows which depends only on the Reynolds number:

$$I = 0.16 \cdot Re_h^{-1/8} \tag{3.15}$$

where $Re_h = \frac{\rho \bar{u} d_h}{\mu}$ and d_h is the hydraulic diameter. Rough estimates are made for different flow types:

- $5\% < I < 20\%$ for rotating machineries (turbines and compressors)
- $1\% < I < 5\%$ for internal flows (for example pipe flow)
- $I \approx 0.05\%$ for external flows (special aerodynamical problems like cars or aircrafts)

In order to quantize the size of the eddies in turbulent flows, the turbulence length scale l is used. It is easy to justify that it must be smaller than the actual dimension of the problem. Hence, l is typically set to a percent level of the geometry size:

- $l = 0.038 \cdot d_h$ for fully developed flows. For a circular pipe it is simply the diameter of the pipe.
- $l = 0.22\delta$ where $\delta \approx 0.382 \frac{x}{Re_x^{1/5}}$ is the turbulent boundary layer thickness, $Re_x = \frac{\rho \bar{u} x}{\mu}$ is the Reynolds number at the distance x from the start of the boundary layer. It is used in cases where the inlet flow is bounded by walls with turbulent boundary layers.

Another specification of the turbulences is achieved through the eddy viscosity ratio which compares the turbulent viscosity μ_t and the kinematic viscosity of the fluid μ:

$$\mu_r = \frac{\mu}{\mu_t} \tag{3.16}$$

It is recommended to use it for low-turbulence cases in external aerodynamics since a proper estimate of the turbulent length scale is nearly impossible, which is rather used in internal flow problems. However in the latter case, the eddy viscosity ratio can still be used as a double-check. Typical values are:

- $\mu_r = 1 - 10$ for internal flows
- $\mu_r = 0.2 - 1.3$ for external flows.
- $\mu_r = 1000 - 10000$ for highly turbulent flows

Depending on the turbulence model different inlet specifications can be done. The k-ε- and k-ω model will be considered more in detail below. If kinetic energy $k = \frac{3}{2}(\bar{u}I)^2$ and dissipation rates ε, ω are not known, the following characterizations can be done. One selects either turbulence intensity and the turbulent length scale as parameters (left) or turbulence intensity and viscosity ratio (right):

$$k - \varepsilon \text{ model}: \qquad \varepsilon = C_\mu \cdot \frac{k^{3/2}}{l} \qquad \text{or} \qquad \varepsilon = C_\mu \cdot \frac{k^2}{\mu \mu_r} \tag{3.17}$$

$$k - \omega \text{ model}: \qquad \omega = \frac{\sqrt{k}}{l \cdot C_\mu^{1/4}} \qquad \text{or} \qquad \omega = C_\mu \cdot \frac{k}{\mu \mu_r} \tag{3.18}$$

Hereby $C_\mu = 0.09$ is a model constant. Note that some CFD codes, as it is for Ansys Fluent, use a different definition of the length scale. Here it is $l = C_\mu^{3/4} \cdot \frac{k^{3/2}}{\varepsilon}$ thus one has to use $l = 0.07 \cdot d_h$ for the turbulence length scale of a pipe.

3.3 Pipe Flow

The flow profile of homogeneous air passing through a closed environment like a pipe does not remain constant but changes after a certain run-up distance. This depends on geometrical properties of the environment, respectively on the characteristic length. For example, for laminar flow ($Re < 2.300$) in a tube it is the inner diameter d_i [12]:

$$l_a \approx 0.05 \cdot Re \cdot d_i \tag{3.19}$$

This run-up distance is present when the fluid enters the pipe at a uniform velocity. A distinction is made for turbulent flow:

$$10 \cdot d_i < l_a < 60 \cdot d_i \tag{3.20}$$

In both cases a parabolic velocity profile forms (cf. Fig, 3.3a). The air comes to a standstill at the walls due to friction (so-called adhesion or no-slip condition $u = 0$ which can be seen as Dirichlet boundary condition) and increases towards the center. Hereby viscous effects due to shear stress between the fluid particles and the pipe wall occur. The layer which is in contact with the surface of the pipe slows down the adjacent layers gradually but due to mass conservation these reduced velocities are compensated by a velocity increase towards the center, forming a velocity profile with a velocity gradient. Therefore, the farther a flow particle is from the wall, the greater its velocity. The fluid velocity should therefore be defined as an average velocity $\bar{u} = \frac{2Q}{\pi R^2}$. The air flow inside the pipe is subdivided into two parts: the region in which shearing viscous forces occur is called boundary layer, whereas the region in which these effects are negligible is called inviscid core or irrotational core flow region [14]. The boundary layer thickness increases steadily from the point where the fluid enters the pipe until it covers the entire pipe. Therefore its growth is limited by the geometric properties of the pipe. The length of the (hydrodynamic) entrance region is known as entrance length l_a (cf. Eq. 3.19). The shear stress is defined through the shear stress at the wall τ_w, the radial distance from the center of the pipe to the point of interest r and the pipe diameter d_i: $\tau = \frac{2\tau_w r}{D}$. The shear stress causes a pressure drop $P_2 = P_1 - \Delta P$ and is highest at the pipe inlet where the boundary layer thickness is smallest and decreases along the flow direction. All these effects will affect the flow rate and forces it to be defined as an average measure as well: $Q_a = \frac{\pi D^4 \Delta P}{128 \mu L}$, where L is the pipe length. In a *turbulent flow*, the profile and thus the velocity increase tends to be flattened due to the interactions of the flow particles with each other, which is not the case in a laminar flow due to the parallel flow lines that ensure that the particles do not interact with each other. Once the velocity profile does not change anymore, one speaks of a **fully developed flow**, in contrast to the developing flow until l_a. Note that this is only true if surface roughness and pipe diameter remain constant. Note also that if the air is guided through a curved pipe system, it will have to travel a certain distance again to become fully developed since the curvature disrupts the velocity profile. In theory, the entrance length l_a is of infinite size but in practice the flow is assumed to be fully developed if the velocity at the pipe center is 99 % of the theoretical maximum freestream velocity u_s, such that an expression for the boundary layer thickness can be found: $\delta = y_{u=0.99u_s}$. For turbulent flows, the shear stress (cf. Eq. 3.1) gets a new component, the eddy viscosity μ_t:

$$\tau = (\mu + \mu_t)\frac{du}{dy}, \quad \text{where often} \quad \mu_t > \mu \tag{3.21}$$

Usually the boundary layer always tends to be laminar as it develops at the beginning of the pipe and can become turbulent depending upon the ratio of inertial to viscous forces acting on the fluid (Reynolds number), respectively if transition occurs within the boundary layer before it covers the whole pipe, otherwise the flow will remain laminar. The awareness of the entrance length plays a crucial role in the reasonable placement of flow meters since they work only properly for fully developed flows [35].

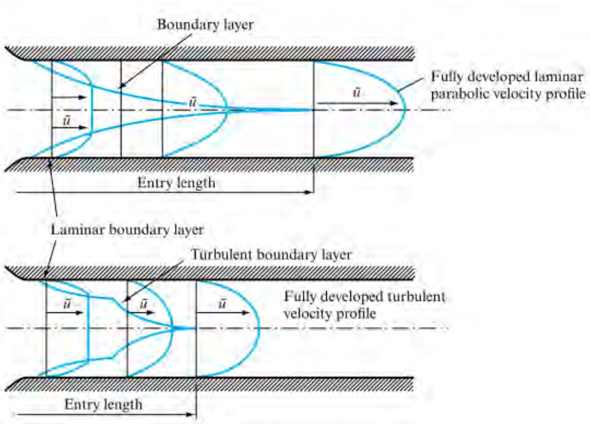

Figure 3.3: Fully developed air flow inside a cylindrical pipe. At the wall the air particle velocity is assumed to be zero whereas it decreases quadratically towards the center of the pipe to a fixed value. This effect is most pronounced for non-turbulent flows. In fully developed flows the flow characteristics no longer change with increased distance along the pipe direction. It occurs also for the temperature profile of the flow. [20]

3.4 Computational Fluid Dynamics (CFD)

Fluid flow problems can be calculated numerically by powerful computers using computational fluid dynamics (CFD). They are broadly used for several types of engineering problems in the industry. However, CFD has to be regarded as still in developmental stage and often does not provide solutions that fit exactly the reality. For example, turbulent flow is still not worked out at a sufficient level. The core of CFD simulations is to solve the Navier-Stokes equations in a set of specific boundary conditions. The equations account for freestream and particle interactions among each other and with surfaces. They can describe fluid flow for a wide range of conceivable scenarios and one has to design its simulation based on physical assumptions that suit the underlying problem. Turbulences can be calculated with RANS equations. The structure of a CFD code consists of a pre-processor, a solver and a post-processor. Built-in models can be loaded, modified and meshed with pre-processing tools. The solver offers a set of partial differential equations, fluid models and boundary conditions to choose between, which then will be expressed in a discretized form in the computational domain. The solver iteratively tries to find a solution within the pre-specified convergence level. The most important boundary conditions are the inlet, the outlet and the wall condition. CFD simulations require the discretization of the geometry into a grid. One commonly used discretization method is the finite volume method (FVM).

Finite Volume Method (FVM)

For the solving process the Fluent uses a Green-Gauss Finite Volume Method (FVM) with a cell-centered formulation to solve the equations numerically by discretizing the computational domain into three-dimensional finite volume elements (cuboids, tetrahedrons,...) that are defined through the mesh design. Volume elements are often referred as cells. More precisely, the conservation form of the PDE is discretized, instead of the classical form (finite element method, FEM) or the weak form (finite difference method, FDM) [10]. The physical behavior of the whole object is defined through the response of the cells to boundary conditions and external forces as well as through the propagation of these responses into adjacent elements that are determined through approach functions satisfying continuity conditions. The solution of the equation of motion can be determined by the parameters of the approximation functions, and the more parameters are included in the calculation of the system of equations, i.e. the more cells are available, the more accurate the approximate solution. These parameters have real physical meaning. For each cell the continuity and conservation equations will be integrated over the whole grid of cells that get flow contributions through their boundaries, such that information can be obtained about physical properties like flow velocity, pressure or temperature. An overview of the main mathematical tools is shown in the appendix A.

Ansys Inc.

Ansys is a software that works with FVM and is able to solve linear and nonlinear problems with steady and transient solvers in a wide physical domain for innumerable scenarios of fluid flows. For CFD simulation the inhouse software Ansys Fluent is available and in the scope of this work the latest open-source version Ansys 2023 R1 Student has been utilized. Ansys is equipped with a modern GUI and 3D CAD interfaces for editing geometries for own use. In the Ansys Workbench the individual steps of the simulation design, from loading the geometry to post-processing the simulated results, can be carried out successively (cf. Fig. 7.2a). User-friendly tools for visualization purposes are available. Ansys Fluent provides 10 types of boundary zone types for specifications of flow inlets and exits. It depends on the exact physical problem and which boundary conditions are most appropriate.

4

Experimental Setup

In the following chapter the details of the current CBM-RICH detector design around mechanical construction, mirroring system and readout electronics will be presented. A demonstrator is situated in the experimental hall at the University of Wuppertal. The cooling system is tested on the basis of this prototype and the cooling concept as well as the main goals will be discussed.

4.1 The CBM-RICH Detector

The CBM-RICH detector foresees a radiator gas vessel filled with ≈ 63 m^3 CO_2 radiator gas ($n = 1.00045$ at $T = 0$ °C, $p = 1$ atm, such that $\gamma_{\text{thr}} = 33.3$ and $\theta_{max} = 1.72°$, cf. [1]), wherein the focusing mirror system is placed. The choice of this type of gas is beneficial in many ways: small contribution to

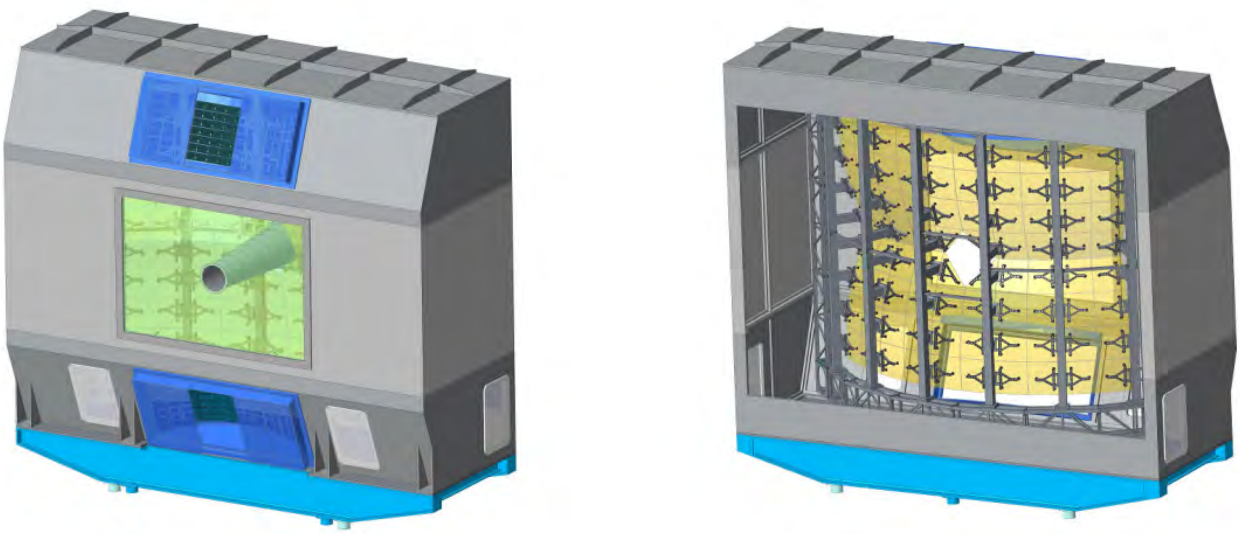

Figure 4.1: Drawing of the CBM RICH detector in beam view (left). The dimensions of the vessel are about 2.2 m in length, more than 5 m in height and about 6 m in width. The shielding boxes (blue) protect the RICH camera from the magnetic field. The beam pipe is situated in the center. A mounting structure supports the mirror wall on the back side (right). [48]

scintillation, absorption of photons below 180 nm [48] and good electron to pion separation until high momenta up to 10 GeV. The latter can be deduced from the threshold momentum of $P_{thr} = 4.65$ GeV/c and the assumption that good separation is provided up to $0.9\,\theta_{max}$. The mirror system is separated into two halves with one detection plane per half placed around the focus point of the system. Around 40 different sized trapezoidal mirror tiles made up of special glass with an Al+MgF_2 coating are mounted to the mirror support structure which ensures its mechanical stability. The spherical mirror surface (13 m^2) with a curvature radius of 3 m and a focal length of 1.5 m is made up of the mirror tiles which are oriented towards the upstream and downstream photon detectors. Two vertical rows of mirror tiles are always mounted to one thin aluminum pillar through small transition frames connecting the tiles to special holding structures (consoles) attached to a pillar. The pillars are mounted in an external frame which in turn itself is mounted to the whole vessel (cf. Fig. 4.1 right). The mirror holding structure withstands the forces of the mirror without any deformations so that a movement of the RICH does not destroy the mirror tiles. The vessel stands on the support platform which allows to align the detector properly along the beam axis in the CBM cave via adjustable hinged supports. Both cameras are mounted above and below the beam pipe 1.6 m downstream the target between the CBM magnet and TRD detector with a tilt angle of 22° downwards (upwards) respectively and are protected from stray magnetic fields coming from the nearby dipole magnet by heavy iron shielding boxes. Being an integral part of the RICH vessel, the shielding box and the camera module, which are attached to each other by a flange with gas-tight seal, are two distinct components of the whole detector allowing to remove the back cover of the box in order to have access to the readout electronics when the camera is in maintenance operation. A conical tunnel leads through the RICH vessel and the beam pipe is guided through this tunnel. Lowering of the material budget is realized by specially fabricated input (probably Kapton foil) and output (plastic sheets) windows.

4.2 The CBM-RICH Camera

The detector comprises two individual RICH cameras placed upstream and downstream (cf. Fig. 4.1 left). The 600 kg aluminum camera is supported by a special rack and can be rotated around the x-axis in order to do assembly work. The camera front includes 14 CNC-milled columns arranged in a circular shape [44], matching closely the focal plane of the RICH mirror. Each column consists of seven rectangular-shaped aluminum frames and serve as support structures for the readout modules. Each backplane is carrying six MAPMT photon sensors with their optical entrance windows closely matching the focal plane (in total 7 readout modules with each $3\times2 = 6$ MAPMTs on the front and $7\times(12+2) = 98$ DiRICH readout modules on the back). CNC-milled aluminum masks provide mechanical fixture for the readout modules and at the same time serve for distribution of the cooling air. The modules are housed in individual compartments and designed to allow cool air to flow from the top and bottom through distribution ducts and exit near the insertion position of each compartment of the mask. Gas leaks are prevented by sealing rubber O-rings, which are placed in a groove milled into the aluminum, against which the back of the PCBs are pressed. The camera halves are held each by a camera box consisting of two D-shaped plates and a right-angled flange. Both cameras are fastened to a mounting flange of the shielding boxes. The design convinces in light and gas tightness, as well as in structural stability and stiffness, according to all expectations based on initial FEM stability simulations.

4.3 The Camera Test Stand

A full-size prototype of the RICH photon detector camera was assembled at the University of Wuppertal based on a 3D CATIA CAD model (cf. Fig. 4.3a). It serves as a demonstrator to test for example the mechanical stability and the performance of the air cooling system.

Air Cooling System Concept

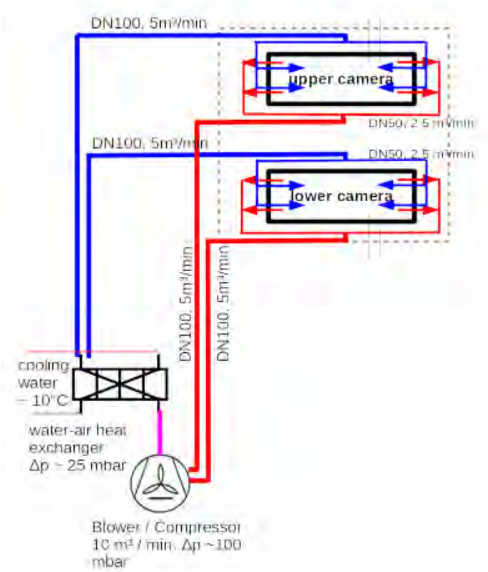

(a) Sketch of the air cooling system comprising the air-water heat exchanger and the blower supplying the upper and lower camera with cool air. The pressure drop due to the blower is at most 100 mbar. [44]

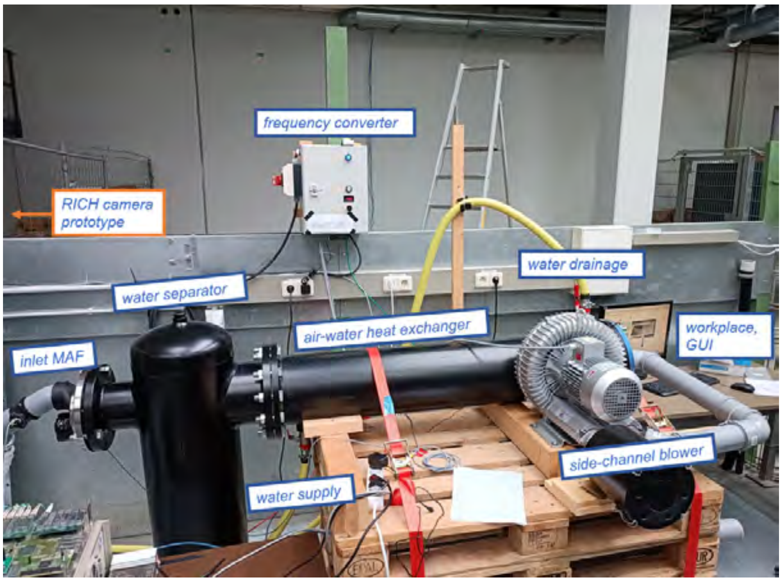

(b) Cool water is introduced through the yellow hose at the bottom left of the exchanger and cools down the air produced by the blower (silver). After recirculation inside the camera the warmed air is guided back to the exchanger and the warmed water is discharged through the other yellow hose on the top right side.

Figure 4.2: Concept of the CBM-RICH air cooling system.

The front-end readout electronics generates a heat dissipation of 3 kW per camera by operating around 2500 individual electronic modules. This poses a problem because of an increase in dark noise in the MAPMTs for increasing temperatures. Temperatures of more than 35 °C at the photon sensors must therefore be avoided. The development of a cooling concept for the demonstrator allows to get first experiences with an air cooling system for a particle detector. Moreover, one can do feasibility tests regarding air flow homogenization, design controlling and system monitoring. The complexity of the system makes a direct water cooling nearly impossible: the sensitive electronics are located inside shielding boxes, so that the risk of their destruction by leaking water would be too great [45]. A significantly less risky variant is to extract the dissipated heat by means of a ***closed-cycle air cooling system***. The basic idea is to blow cold air ($T \leq 18\,°\mathrm{C}$) inside the camera module through each backplane cooling mask and to push out the warm air ($T \approx 45\,°\mathrm{C}$) away from the backplanes and MAPMTs (cf. Fig. 4.2a). After being extracted out of the camera volume, the warm air is not released inside the experiment cave, which would be counterproductive in terms of keeping the environmental temperature as small as possible, but is recirculated by an air-water heat exchanger which is connected to the cave cooling water circuit. Another positive side effect is that any pollution or contamination like dust particles or dirt are prevented to enter the air stream. A water temperature of $\sim$ 16 °C provided in the CBM cave leads to an air temperature of 16–18 °C at the detector inlet. Both, an air temperature of $\sim$ 18 °C and the air recirculation prevents the emergence of large amounts of condensing water, which is beneficial in this context. At the test stand, the water is much cooler in comparison with 6–8 °C, furnishing cool air at 9–10°C. Along the 14 columns the air is predicted to be inhomogeneously distributed. The main objective of this work is to develop concepts to homogenize the airflow in each outlet (lateral air distribution), in each column and in each frame (vertical air distribution), since the heat dissipation of MAPMTs at these scales is assumed to be uniform with respect to the air flow.

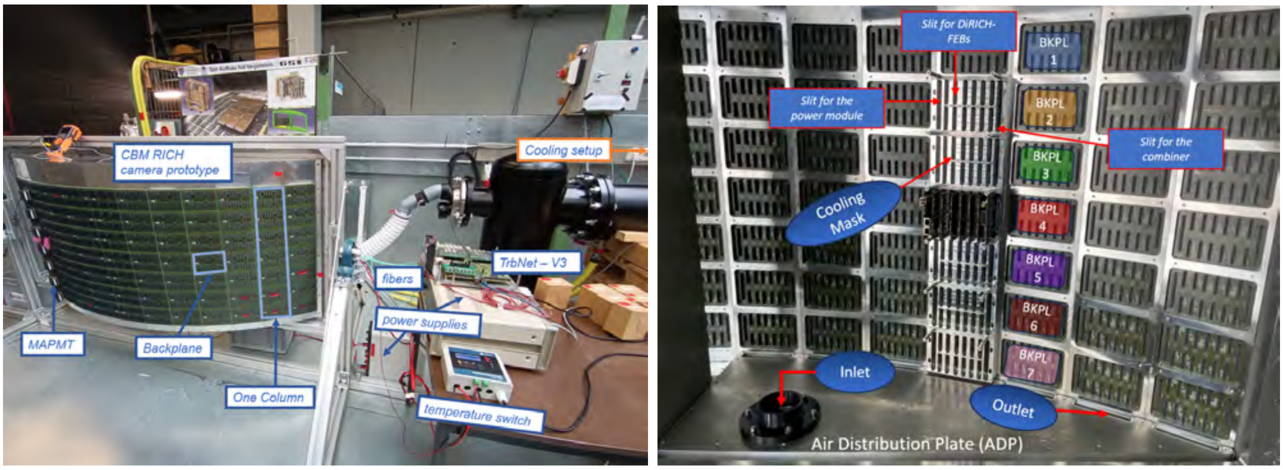

(a) Front side of the prototype and readout electronics. **(b)** Back side of the prototype and readout electronics.

Figure 4.3: The CBM-RICH Test Stand at the University of Wuppertal.

Cooling Prototype

The study of the air cooling system allows to predict the requirements for the blower. For example, it would be important to know the amount of air that has to be blown into the system dependent on the backplane PCB temperature. The cooling prototype (cf. Fig. 4.2b) consists of the air-water heat exchanger (Parker WFN090) with an additional centrifugal water separator (Parker SFH089N) which removes condensing water from the output air produced by a side-channel blower (SKV-NS-420-3-916). The blower provides a maximum of 420 m^3/h ($\sim$ 515 kg/h) at 50 Hz. Only the heat exchanger is part of the final CBM-RICH detector and will later be moved to the CBM cave. The air flow and differential pressure provided by the blower can be controlled by a three-phase frequency converter. It is located in a control cabinet together with a RaspberryPi computer for slow control. A hose is attached to the heat exchanger and enables temperature control by providing cooling water regulated through a solenoid valve. A first estimate reveals the requirement of 5 m^3/min (367.5 kg/h) for one camera and 600 m^3/h (735 kg/h) for the full RICH, respectively [44]. This corresponds to 26.25 kg/h per column and 3.75 kg/h per backplane. Important measures are also the pressure drop inside the camera and inside the heat exchanger. First tests have already been done. The latter can handle at least 200–300 mbar whereas at full operation a pressure drop of $\sim$ 25 mbar is observed. It seems to be advisable that the pressure drop in the camera should not to exceed 100 mbar but stay in the order of $\sim$ 20–40 mbar [45].

Backplane Cooling Mask

First plastic prototypes of the backplane cooling masks were manufactured to attach them to the camera and to perform some tests. A first fabrication in aluminum is also available (cf. Fig. 4.3b). The air will be pushed through a total of two times seven air channels, where one row each consists of five channels that are located centrally and two outer channels with a slightly larger distance to the middle channels. The air is guided through several slits of equal size to the backplane on one side and onto the readout electronics on the other side. Generally, the aim is uniform cooling of all components. As it is the case for the lateral air distribution of the air distribution plate (ADP), here the vertical air distribution through the slits is estimated to be inhomogeneous as well. Depending on the degree of inhomogeneity, reflections must be made whether the slit size is to be adjusted or not. This will be investigated in CFD simulations.

Air Distribution Plate

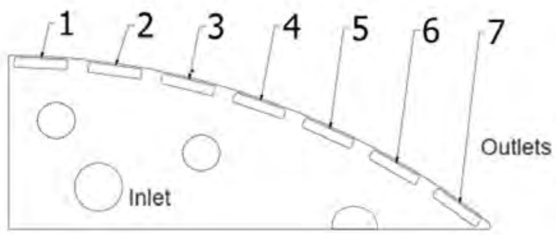

(a) Sketch of the ADP with all the 7 outlets drawn in (left). The inlet diameter is d_{inlet} =100 mm, the outlets are 112 mm in width and 21 mm in height. Modified and taken out of [41].

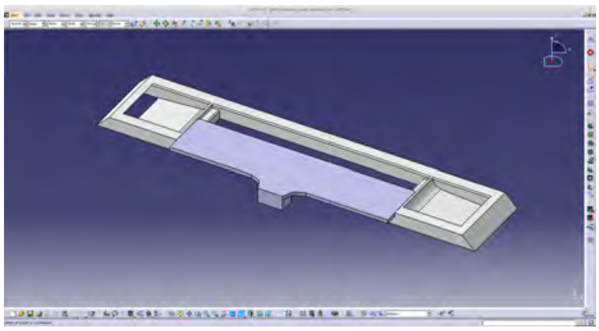

(b) Model of the plastic slider that can be placed on each outlet. It can be flexibly moved up and down, increasing respectively decreasing the outlet area size. Credits: Dennis Pfeifer.

Figure 4.4: The Air Distribution Plate (ADP).

A sketch of the ADP is shown in Fig. 4.4a. Four ADPs are installed in a camera, two at the top and two at the bottom. They have a circular opening for air inlet (d_{inlet} = 10 cm) and seven individual rectangular-shaped rounded outlets through which the air is pushed to the seven columns. It is important to mention that the sum of the outlet areas is larger then the inlet area. Further, it can be assumed that the system is gas-tight. Each outlet will be used for calibrating the setup and to perform air distribution measurements. Due to the different distances between outlets and inlet it is to be expected that the air flow out of the different outputs is strongly inhomogeneous. Besides, in the interior of the ADP there are cylindrical cut-outs affecting the flow through the panel. First CFD simulations already showed the inhomogeneity of the air distribution. However, these simulations are not elaborated enough and will be therefore improved within the framework of this thesis. Once there is a rough idea of the degree of inhomogeneity, it can be tried to reduce it. One measure that has been taken to do this is to thread small plastic sliders between the plate and the cooling mask, which reduce the areas of the rectangular outlets along their vertical side. They can be moved flexibly, making the system highly adaptable to several scenarios (cf. Fig. 4.4b).

DiRICH Readout Chain Setup

The RICH front-end electronics (FEE) of the CBM-RICH detector is very similar to the FEE used for the miniCBM (mCBM) RICH (mRICH) and HADES-RICH detector. The backbone of the readout is the backplane, a PCB of 156×105 mm^2 size. It distributes power, low and high voltage, digital serial links and analog connections to all the components that will be discussed below. On the side facing the radiator volume, the backplane is equipped with six MAPMTs in a 3×2-array with pin header for PMT signals as well as ground and high voltage connections, while on the opposite side 12 DiRICH front-end boards (FEBs) of 100×47 mm^2 size (cf. Fig. 4.6), a data concentrator (sometimes referred as combiner) and a power module per backplane are attached to SAMTEC connectors (cf. Fig. 4.5). One single backplane connects twelve 32 channel DiRICH-FEBs to six 64 channel MAPMTs and hence hosts 384 channels in total. For proper communication among these components, the channels on the backplane are routed and the several conductor tracks on the PCB layers have sufficient distance. The whole setup is connected to a Trigger Readout Board - V3 (TRB3) which provides trigger for readout through the combiner. CBM measures heavy-ion collisions with collision rates up to 10 MHz and data rates up to 1 TB/s. A powerful triggerless data acquisition system is being developed for that purpose.

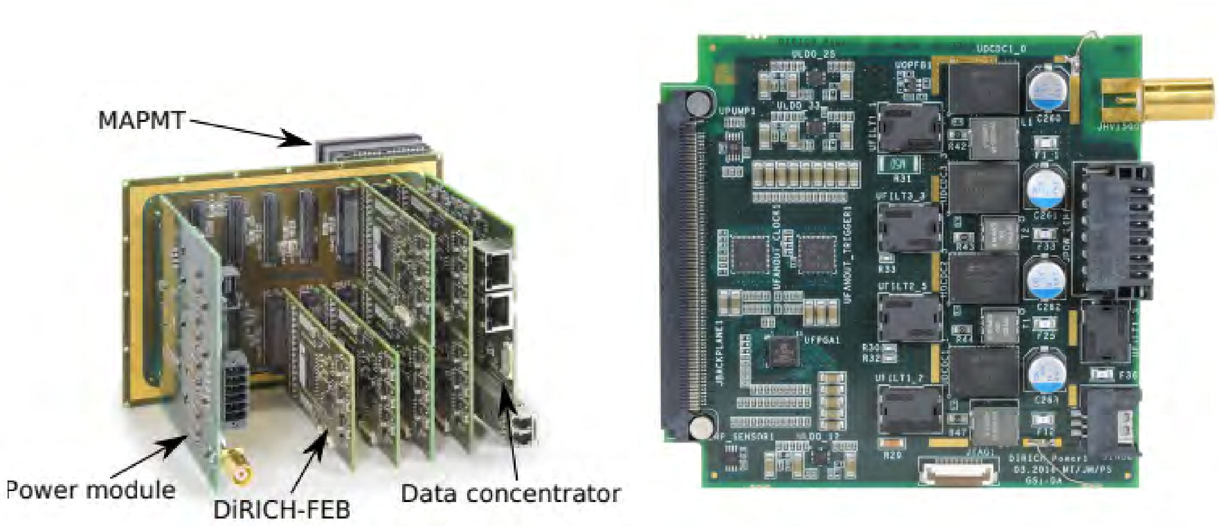

Figure 4.5: The DiRICH Readout Chain. The components are mounted on the front and back side of a backplane. In this picture (left), the power module, six DiRICH-FEBs and the data concentrator are attached to the front side and one MAPMT is plugged into the back side. Customarily, the backplane offers 12 slots for the DiRICH-FEBs. The components are supplied with high and low voltage by a power module (right). [24]

DiRICH-FEBs

The readout of the 32 MAPMT channels is done measuring the leading (LE) and trailing edge (TE) of each incoming signal. The leading edge is used as hit arrival time, while the difference between leading and trailing edge gives the so-called time over threshold (ToT) which intern is a proxy for the signal charge. For that purpose, the input signals need to be amplified, which is done by the inverter amplifier that every DiRICH channel has. The negative signal is shaped to a positive signal by an undershoot in the falling edge which leads to a rectification of the ToT signal measurement in this region. To distinguish a signal pulse from noise the input voltage is compared to a threshold. This discrimination takes place at the low voltage differential signaling (LVDS) inputs of a Lattice ECP3 forward programmable gate array (FPGA). The threshold voltage needed for the comparator discriminator is supplied by two MachXO3 FPGAs (sometimes referred to as side-FPGAs). Whenever one of the two lines overshoots compared to its partner line, an internal FPGA signal is generated and passed to a time-to-digital converter (TDC). In principle, the scaler counts the number of signals crossing the threshold and one has access to the current rate in the corresponding channel. The digital input signal is guided from the scaler to the TDC and basically measures the LEs and TEs at the discriminator output, wherein the TEs are delayed with a calibrated stretcher. Hereby, a timing precision of 7 ps can be reached [46]. The DiRICH-FEBs send the data via Serializer/Deserialize (SERDES) media interfaces to the combiner board [48]. Signals that exceed the threshold are measured and their LE and ToT information are stored.

Data concentrator/Combiner

The event data of all the DiRICH-FEBs in the backplane are brought together and merged in the data concentrator (cf. Fig. 4.6). It is connected to the central data acquisition and receives a readout trigger signal from the central trigger system (CTS). From there it is further distributed to the trigger fanout chip on the power module and to the DiRICH-FEBs with a 200 MHz clock used also by the TDC and the TrbNet. The data concentrator is equipped with an ECP3 FPGA. Furthermore, its hub functionality allows to transfer the data at high rates from the uplink to the downlink ports (DiRICH-FEBs) and back. Finally, the data concentrator allows also the distribution of the slow control to all DiRICH-FEBs.

Power Module

The RICH FEE needs to be provided with low and high voltages. A voltage of -1000 V is provided through the backplane and LEMO ports to the HV connectors of the MAPMTs while the other components are fed with low voltages between 1.1 V and 3.3 V which turns out to be quite challenging due to the need of high currents. Two scenarios were under discussion for the CBM-RICH setup: the first option could be to use four classical onboard DC/DC converters, where the power module would be connected to a 36 V supply voltage and the ICs regulate the input voltage to four lower output voltages. This solution is favorable in terms of the light cable weight, but at the same time leads to a bad noise bandwidth due to electromagnetic noise of the DiRICH-FEBs. Another way would be to connect twelve power cables with pre-regulated voltages to a Weidmüller connector which acts as bypass of the converter. It has excellent noise behavior but since the cables are not flexible this leads to high forces on the PCB and additionally a voltage drop on the supply lines is to be expected. The final decision was made in favor of the DC/DC converter. For the measurements at one column of the camera at the test stand setup a total of 84 DiRICH-FEBs where individually programmed. This requires connecting the boards with a JTAG cable and programming both the main FPGA and the two side-FPGAs manually with corresponding programming scripts. The programming can be considered successful if the DiRICH-FEB appears in the TrbNet when it is plugged in. Finally, the noise bandwidth spectrum can be investigated in order to ensure that the DiRICH-FEB is well-functioning.

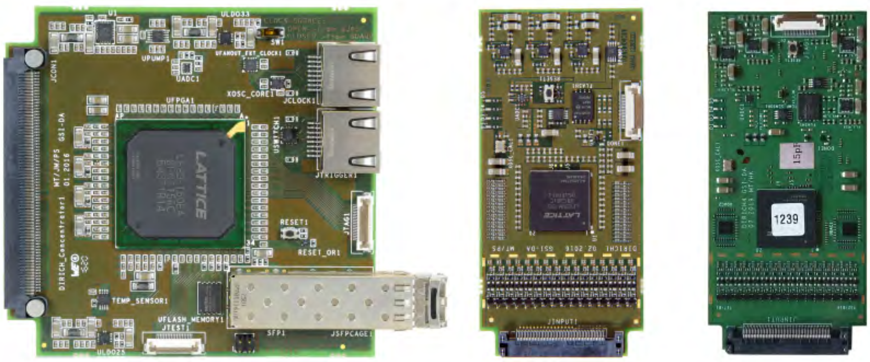

Figure 4.6: Data concentrator (left) and DiRICH-FEBs (right). [48]

5

Slow Control System of the CBM-RICH Test Stand

Slow control systems are used to setup and monitor a large number of hardware components such as temperature sensors, pressure gauges and leak detectors and many other physical quantities. They are suited especially for long-time monitoring and remote control of experiments. This chapter will briefly describe the controlling and monitoring software that were developed and used for the experiment.

5.1 The EPICS Software Environment

The Experimental Physics and Industrial Control System (EPICS) is an open-source software framework used for the implementation of distributed control systems (DCS) [11]. It can be applied for process controlling and monitoring purposes at scientific and industrial facilities with a large number of computer networks. EPICS provides a network including lots of tools and libraries for the communication of several devices and systems. The most important component of the EPICS framework is the installation of so-called Input-Output-Controllers (IOCs). These are processes that communicate with other components over the network and publish or exchange their data via the Channel Access (CA) network protocol. The devices and their properties are defined in a database as so-called records and establish the connection between the physical devices and the corresponding IOC instances. The data inside these records are stored as unique identifiers known as process variables (PVs). An Operator Interface (OPI) allows to view and control the PV data with graphical user interface (GUI) tools through display widgets, for example Control System Studio (CSS) Phoebus.

5.2 Control Studio System (CSS) Phoebus

Control System Studio (CSS) is an open-source software which provides a collection of tools and libraries to create graphical user interfaces (GUIs) of large-scale controlling and monitoring systems [18, 38]. Based on a modular architecture of the eclipse RCP framework, it can be flexibly modified and extended for specific applications and requirements of developers. Phoebus is the current variant of CSS. It is independent on eclipse RCP but uses a java/javafx based implementation with java features like SPI instead [17]. CSS supports the channel access and pvAccess protocols, enabling the communication between different devices and systems in the EPICS network [32]. Multi-threading applications are possible as well. The Data Browser tool allows to collect and plot real-time and archived values on a time axis, provided it is created from an OPI visual component which is linked to a PV. In general, a lot of data visualization tools like graphs, charts and tables are placed at the disposal. Alarms can be adjusted for troubleshooting and events can be monitored with fast response times. Data processing and task automation is possible with scripting thanks to compatibility with various programming languages such as Python.

5.3 Slow Controller Readout

Connection of the slow control interface card to a RaspberryPi allows to run EPICS, which is useful for later integration into RICH monitoring system. The RaspberryPi named *flowmeter* hosts all MAF sensors while temperature and pressure sensors are connected to a different RaspberryPi named *RICHcontrol*, which is also used to control the air system blower. Each system variable is assigned a ChannelAccess variable in the EPICS network (cf. Tab. 5.1). Parameters like the blower frequency can be adjusted via *caput* commands whereas monitoring variables like temperatures or pressures can be retrieved by *caget* commands. This allows live monitoring of all system parameters, as well as the associated design of a graphical user interface (GUI) for the test stand, including its cooling and camera components.

Table 5.1: ChannelAccess variables in the EPICS system. Accessible or configurable with caget or caput commands, respectively. Temperatures are output in °C, pressures in mbar and mass air flows in kg/h.

EPICS Variable	Parameter
AIR_SYSTEM:FU:Freq	returns actual blower frequency
AIR_SYSTEM:FU:SetFreq	sets fix frequency value of the blower
AIR_SYSTEM:FU:SetFreqInput	1: set frequency manually, 3: set frequency in EPICS
AIR_SYSTEM:TEMP:air_input	returns air temperature at heat exchanger input
AIR_SYSTEM:TEMP:air_output	returns air temperature at heat exchanger output
AIR_SYSTEM:TEMP:ambient	returns ambient temperature
AIR_SYSTEM:TEMP:water_input	returns temperature at the inflow valve
AIR_SYSTEM:TEMP:water_output	returns temperature at the outflow valve
AIR_SYSTEM:PRES:ambient	returns ambient pressure
AIR_SYSTEM:PRES:air_output	returns pressure at the air output
AIR_SYSTEM:BOSCH:inlet_2	returns mass air flow going through the inlet
AIR_SYSTEM:MAF:outlet_1...7	returns mass air flow going through the outlets

5.4 The Cooling Controller System GUI

The current look of the slow control GUI at the CBM-RICH test stand at the University of Wuppertal is shown in Fig. 5.1. Temperature and pressure sensors are placed at different positions inside the water-air heat exchanger. The air leaving the exchanger is monitored by the inlet MAF sensor by continuously accessing the EPICS variable AIR_SYSTEM:BOSCH:inlet_2. The sensor is located at the output of the heat exchanger and is directly connected to the PVC inlet hose that guides the air to inlet opening of the ADP. A rough qualitative idea of the degree of inhomogeneity is obtained on the right side by monitoring the outlet MAF sensors by means of the bars (tanks). They are obtained by the EPICS variables AIR_SYSTEM:MAF:outlet_1...7. The GUI is also used to monitor the cooling air temperature which will be important when the heat dissipation of a single camera column will be investigated. Once the camera prototype is fully equipped, for future prototype tests the GUI could be replaced with a heat map reading out the temperatures of all electronic components in real time at different settings of the blower. This would contribute to the idea of a hotspot detection in order to know where additional warm air can be extracted.

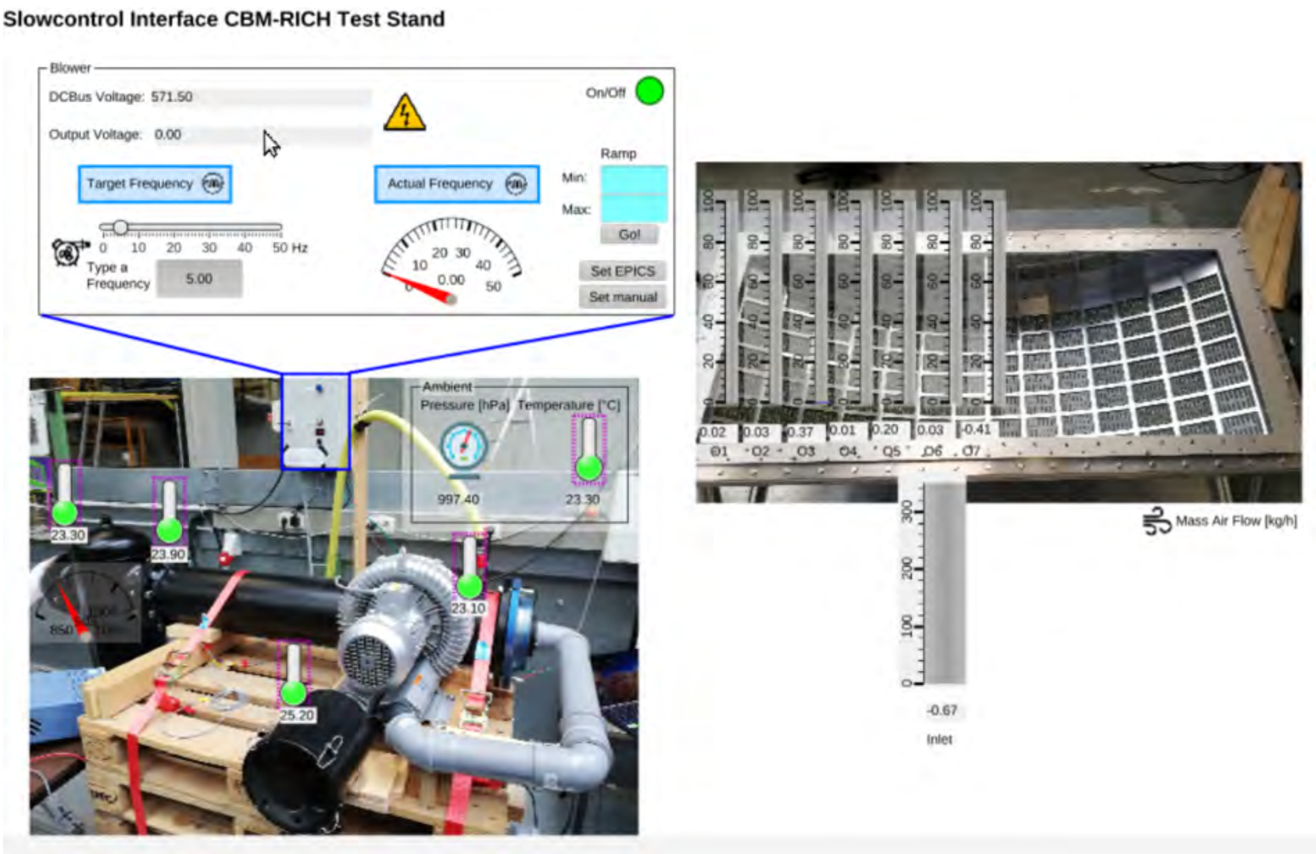

Figure 5.1: Snapshot of the graphical user interface of the slow control interface. An image of the cooling setup components is shown on the lower left. One-wire sensors are placed at different positions of the setup. Their CA-variables are published in the EPICS system and read out by the CSS-GUI for a complete temperature and pressure monitoring of the system. The frequency can be adjusted and monitored in the frequency converter box above. The MAFs of inlet and outlet sensors are visualized with vertical tank bars on the right.

6

Tests and Calibration of the Mass Air Flow Sensors

This chapter will describe procedure and results of calibrative measurements. The two different MAF sensors calibrated throughout this chapter follow both the constant temperature anemometry (CTA) principle, which will be briefly discussed first. This results in a highly non-linear response function of the analog output signal and hence there is a strong need to have a calibration curve in order to translate voltage into mass air flow. Appropriate calibration measurements must be made on the cooling system structure. The BOSCH sensors are used to measure the total cooling inflow into the CBM-RICH ADP through the inlet. This inlet is connected via a hose to the side-channel blower. The calibration of the FLW122 sensors, used to measure air flow at any location inside the camera with the purpose to develop the distribution system, depends on the individual installation situation and therefore needs to be calibrated separately.

6.1 Working Principle of Mass Air Flow (MAF) sensors

Hot-wire mass air flow sensors use an operation principle that is called Constant Temperature Anemometry (CTA). In general, an anemometer is a meteorological device used to measure flow fields or wind speeds. In this case, thermoelectric anemometry is exploited (cf. Fig. 6.1a). A constant voltage is applied to a fine wire, e.g. made up of tungsten whose electrical resistance is – as of most metals – dependent upon temperature, so that the wire is heated to some temperature above the ambient. Thereby, the excess temperature of the heated sensor element is kept constant. This is only achievable if one additionally measures the ambient temperature. When air flows past the sensor element, the sensor area cools down and the current is increased due to the decrease of the electrical resistance (Ohm's law). The current increase itself compensates the loss of heat and the wire temperature rises again to its constant level with respect to the ambient temperature. Hence, the change in current is proportional to the mass air flow flying past the wire. Conventional volumetric CTA-based MAF sensors are not very sensitive to humidity and contamination. The BOSCH HFM7-R5 is a pre-calibrated MAF sensor where the calibration curve is provided by the manufacturer (cf. Fig. 6.1b). It is sensitive up to 480 kg/h, ca. 6.5 m^3/min and is commonly used in automotive applications. The analog readout interface is already included. The test stand owns a total of four specimens and it is used to measure the amount of air that is flowing through the inlet of the ADP. The MAFs used to measure the outlet air distribution amongst the seven outlets of the air distribution plate are so-called FLW122 thermical flow sensors (cf. Fig. 6.2a). A total of seven FLW122 sensors are used. They operate at temperatures of -20...150°C with a measurement range of 0–100 m/s at a 3 percent precision level and with fast response times in the order of 2 s. The three-pin

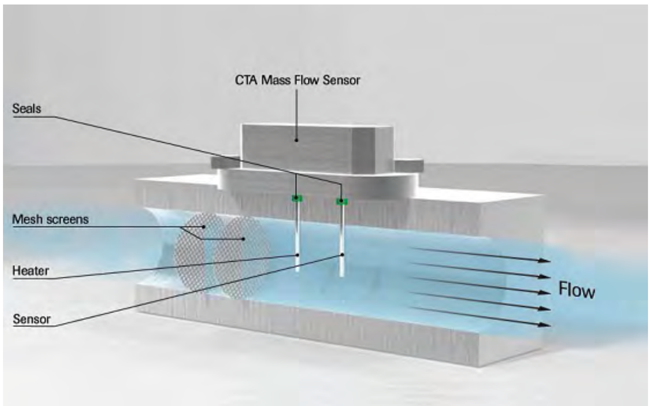

(a) CTA working principle: the temperature difference ΔT between a low-ohm heater and a high-ohm temperature sensor pin, two stainless steel probes, is aimed to be kept constant. The MAF is extracted from the power variation that is required to maintain the temperature difference constant, respectively to compensate the heat loss that is directly proportional to the flow velocity. The voltage required at the bridge input is therefore a measure of the flow velocity. [47]

(b) BOSCH HFM7-R5 MAF sensor. A calibration curve is provided by the manufacturer and it is commonly used for automotive applications. The sensor pin is in the center of the cylindrical housing. The sensor works only properly in one direction (out of the paper plane). Before the air flow reaches the sensor pin, it passes through a fine grid, which is faintly visible here. Special pipes were acquired for the measurements that fit exactly the size of the sensors.

Figure 6.1: Constant Temperature Anemometry (CTA) working principle.

sensor consist of two platinum resistive elements on a chip which are switched in a Wheatstone bridge with additional resistors R1, R2 and R3 such that both Pt elements have always a fixed temperature difference due to the applied voltage (cf. Fig. 6.2b & 6.3b). The third pin is set to ground (GND). Both, the FLW122 as well as the BOSCH sensors are evaluated with a flow module.

(a) FLW-122 thermical flow sensor. [27]

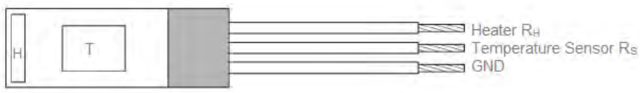

(b) Heater R_H and sensor R_S are switched in a full bridge. [28]

Figure 6.2: FLW-122 sensor manufactured by B+B Thermo-Technik GmbH.

6.2 Readout of the MAF sensors

For simultaneous readout of all BOSCH and FLW122 sensors a dedicated slow control interface card has been developed (cf. Fig. 6.3a), providing all necessary interface circuitry and ADCs for fast sampling of both sensor types. For the BOSCH sensors, all active measurement circuits are already included in the sensor itself, such that the output signal can be directly digitized using an ADC. The FLW122 sensors are uncalibrated and need external circuitry for readout as they come without measurement electronics, just a direct connection to the reference and heating element. They come without any housing and can be used very flexibly. Therefore, an external measurement bridge is required. It actively regulates the heater current such that a constant temperature difference between reference and heated surface is kept. The bridge is included on the slow control interface card. Potentiometers (blue) allow to adjust the temperature difference and thus also the measurement range. If the temperature difference is regulated too high, then the sensitivity of the sensor increases and subsequently high mass air flows can no longer be measured reliably.

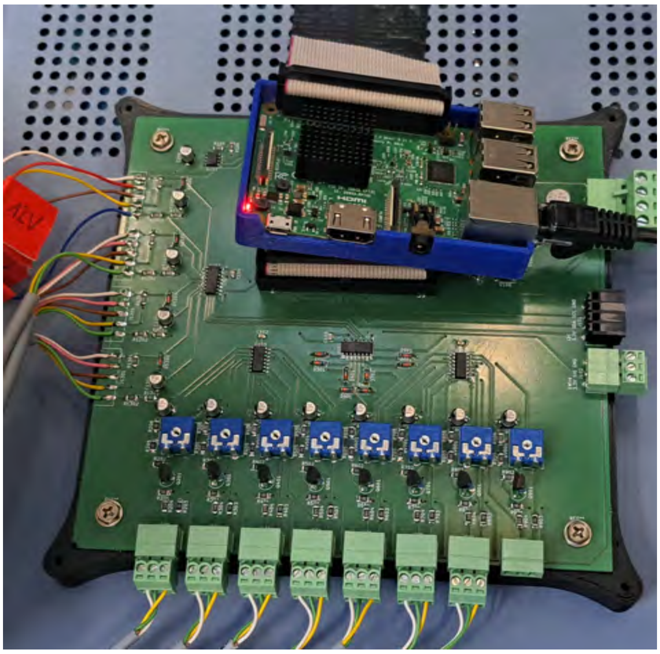

(a) The slow control interface card used to connect up to four BOSCH MAF sensors (connected on left side) and up to eight FLW122 MAF sensors (connected on the bottom side), including the necessary measuring bridge amplifier and control circuits. Dedicated potentiometers (blue) allow to adjust the current of the sensors leading to a temperature offset between heater and sensor. The module as well as the RaspberryPi computer are operated with a four-channel power supply unit.

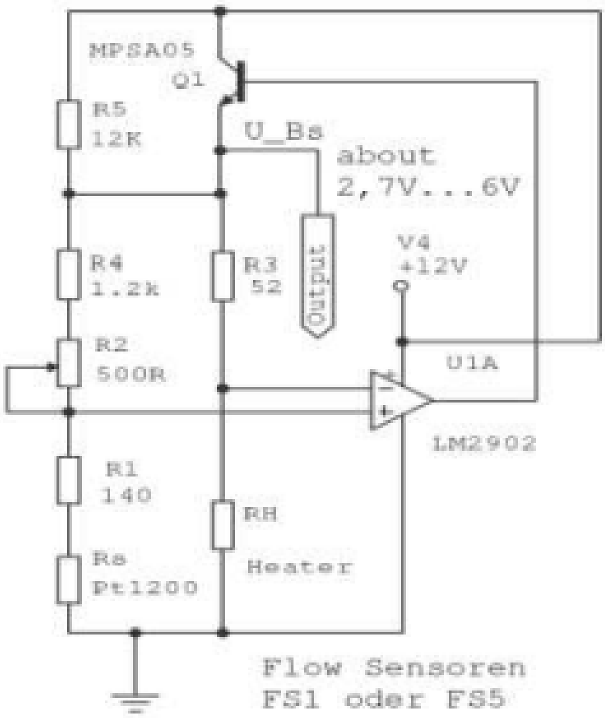

(b) Example of a connection sketch: the heater R_H and the sensor R_S can be connected in a bridge. An operational amplifier together with additional resistors R_1, R_2 and R_3 regulate the current such that the temperature difference $\Delta T = T_H - T_S$ between both surfaces is kept constant. The heat loss of the heater is dependent on the change in mass air flow, and thus also the power to maintain ΔT constant. Hence the voltage required at the bridge input is a measure for the mass air flow. [27]

Figure 6.3: The slow control interface.

6.3 Inlet Mass Air Flow Sensors

In order to assure accuracy over a large dynamic range (which is required in different types of measurements) and reproducibility of the BOSCH sensors a series of cross-check measurements were done. First, the calibration of the BOSCH sensors was verified. To do this, one can imagine a setup that tests whether the air flow coming through a first sensor is evenly divided among three other sensors on an output (cf. Fig. 6.5a). The setup of these measurements merely includes the four BOSCH sensors, a couple of commercially available cylindrical tubes from the hardware store and a custom-made 3D-printed three-way splitter (cf. Fig. 6.4) with one opening for the input BOSCH sensor and three openings for the output BOSCH sensors. The inside of the splitter is made up of a Mercedes star shape, such that

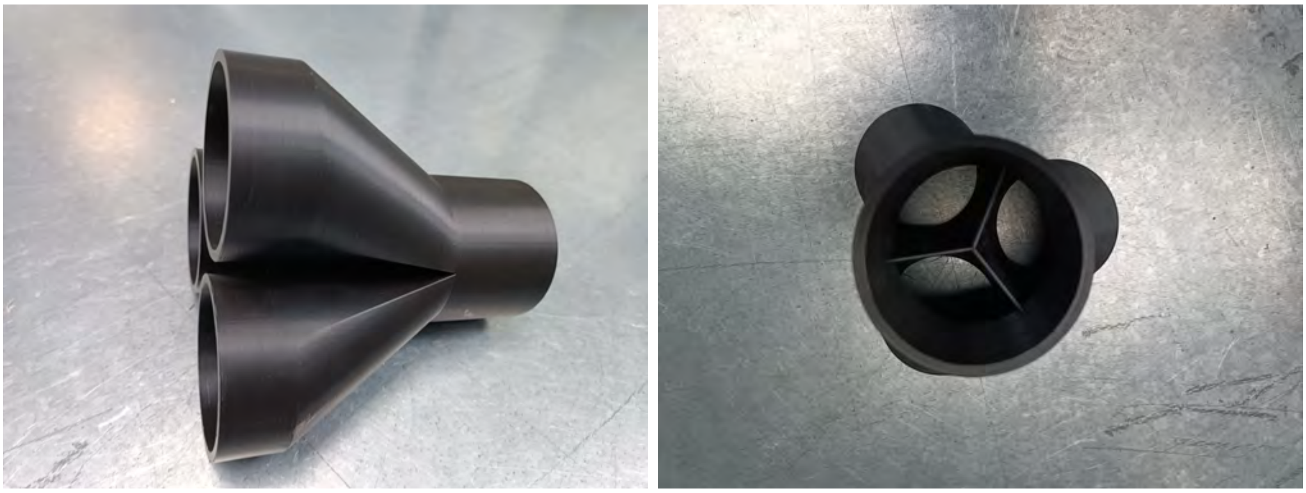

Figure 6.4: 3D-printed customarized splitter with one input opening and three output openings. One BOSCH sensor is plugged onto the single opening on the right side and measures the input air flow. Three other BOSCH sensors are plugged onto the three openings on the right side and prove if the air is split up in equal three parts. MAF sensors work most reliable for fully developed flows. Hence additional prolongation tubes are attached to the input and output openings and connect the sensors to the splitter. The length of these tubes is decisive for whether the flow gets fully developed and laminarized or not which would effect the accuracy of the calibration.

the air is is split up into three openings. It has been designed so that one only has to plug the sensors onto the openings. The calibration curve of the BOSCH sensors can be considered as trustworthy, if each output BOSCH sensor would measure 1/3 of the known input air flow for a range of air flows with different strengths. The curve (cf. Fig. 6.6a) is provided by the manufacturer and the calibration function was extracted from the data sheet with an online tool:

$$MAF(V) = -28.00507 + 31.96391 \cdot V - 5.37310 \cdot V^2 + 0.66098 \cdot V^3 + 1.19383 \cdot V^4, \tag{6.1}$$

where in some tests in advance the offset has been determined and is subtracted during a measurement in the readout script. For obvious reasons an additional constraint must be that the sum of the individual output flows must equal the input air flow so that the flow is generally neither overestimated nor underestimated in a systematic way. This is of particular importance, since the BOSCH sensors are used to calibrate the seven smaller FLW122 sensors, which will be used to measure the output airflow through the seven output openings of the ADP, where a single BOSCH sensor will be used to measure the full input flow. Hence the FLW122 sensors operate at only 15% of the flow of the BOSCH sensors, and their calibration will only be sufficiently correct if good linearity of the BOSCH sensors over a wide range is proven.

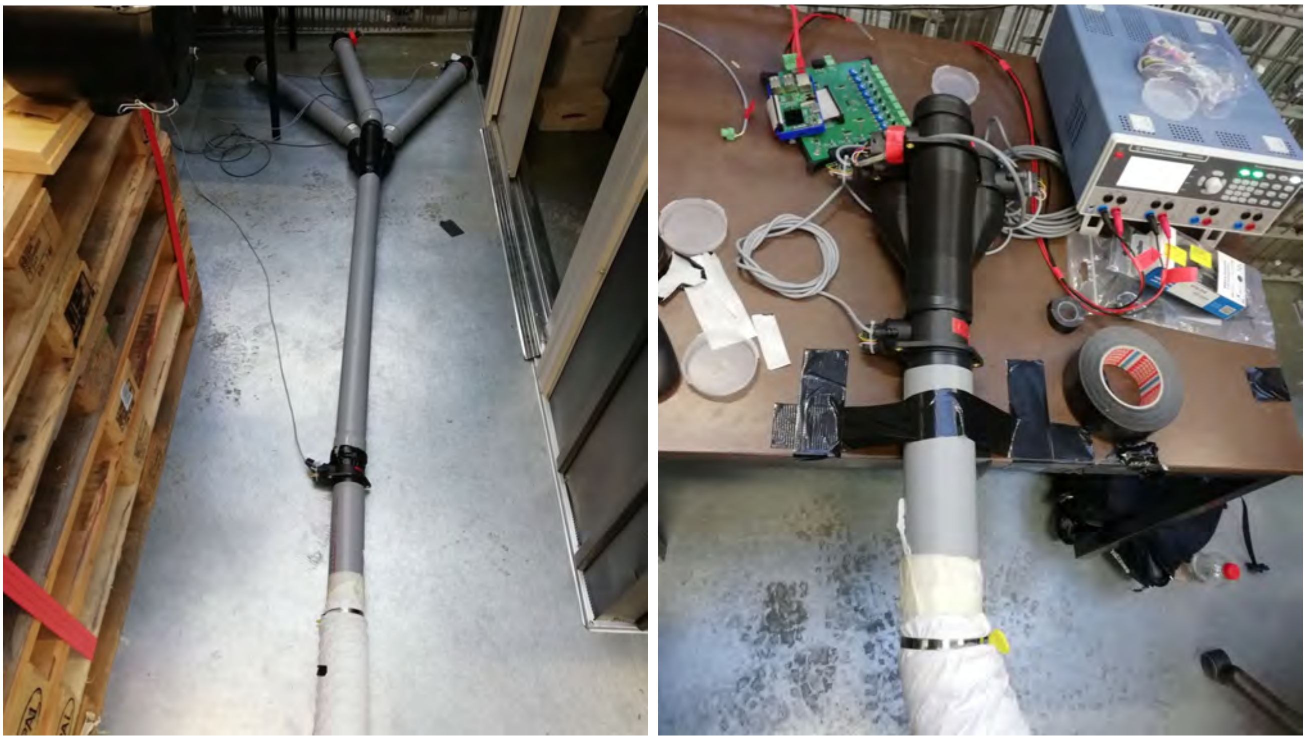

(a) Setup with prolongation tubes. **(b)** Setup without prolongation tubes.

Figure 6.5: Setup of the cross-check measurement: incoming air (from the bottom) measured with a first BOSCH sensor (non visible in the image) is equally distributed into three output channels through the three-way splitter (black), homogenized with conventional tubes that are attached (gray) and finally measured with three output sensors.

Initial measurements revealed differences between the input flow and the sum of the seven output flow measurements, hinting a possible miscalibration. At that time, there was still no use of additional pipes so that all BOSCH sensors were connected directly to the splitter. There are various possible reasons for this. What should be mentioned first is that the sensors utilize a small measuring cell positioned in the center of the circular cross section. Secondly, the air flow coming out from the hose is most likely not perfectly homogeneous and besides the effects of fully developed flows discussed earlier one should take into consideration some inconsistencies in the air stream. Further, since turbulence increases with fluid velocity, at higher input air flows some turbulent effects will occur. This becomes especially relevant in the region inside the splitter. As a last aspect the occurrence of slipstream effects can play a role. The sensor pin in its natural composition itself, as well as the elements in the interior of the splitter can simply block the path of the air when it is on its way to the output sensors and that is crucial if the components are altogether situated to close to each other. These effects could successfully be suppressed for the final test measurements by adding tubes between splitter and sensors (cf. Fig. 6.5b), providing valuable experience for all further measurements to come. By increasing distance between splitter and input-, as well as output-sensors the air is more homogenized and laminarized at the splitter yielding more consistent results. The final results tell that the measured air flow is now equally distributed over the three output channels (cf. Fig. 6.6 & 6.7 right) and their sum matches well the amount of air blown into the first sensor despite the non-linear measurement principle (cf. Fig. 6.7 left). This demonstrates the good accuracy, linearity and reproducibility when measuring the MAF, as the input and the three output BOSCH sensors are operated in different regimes of the characteristic curve.

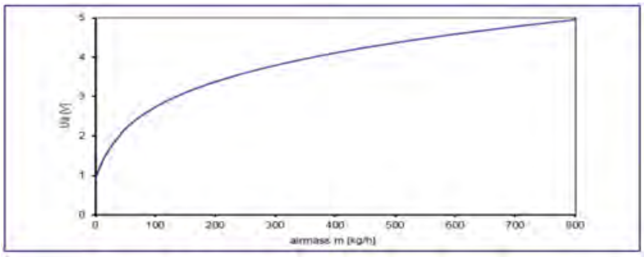

(a) Calibration curve provided by the manufacturer BOSCH, taken out of the data sheet. The MAF is plotted against the output voltage. For small MAF the highly non-linear character of the curve is clearly visible. In terms of a good calibration more data points should therefore be taken for small flows. The data was fitted with a fourth-degree polynomial function to translate output voltages to MAFs. [13]

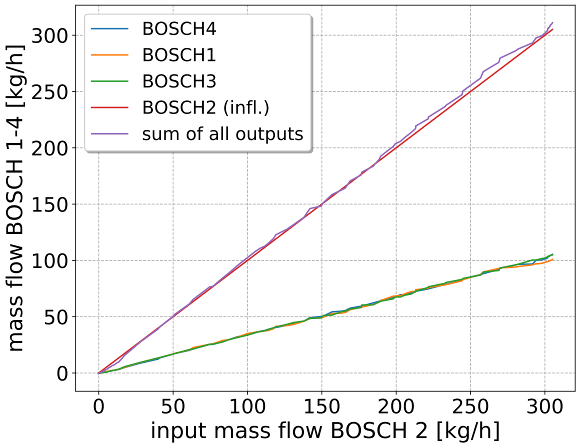

(b) Comparison of input mass air flow (BOSCH2) and output flow (BOSCH1, 3-4) after the three-way splitter. The sum of all three output sensors (red) matches very well the input flow for a large dynamic flow range with only little deviations towards highest flows, despite the fact that input and output sensors are operated at quite different flow ranges. The sensors on the output all three measure pretty much the same flow values.

Figure 6.6: BOSCH calibration curve and cross-check results.

One of the most important findings is the reliability of the sensors depending on the air ducting. Air flows that are not fully developed can have a significant impact on the measurement accuracy of the sensors.

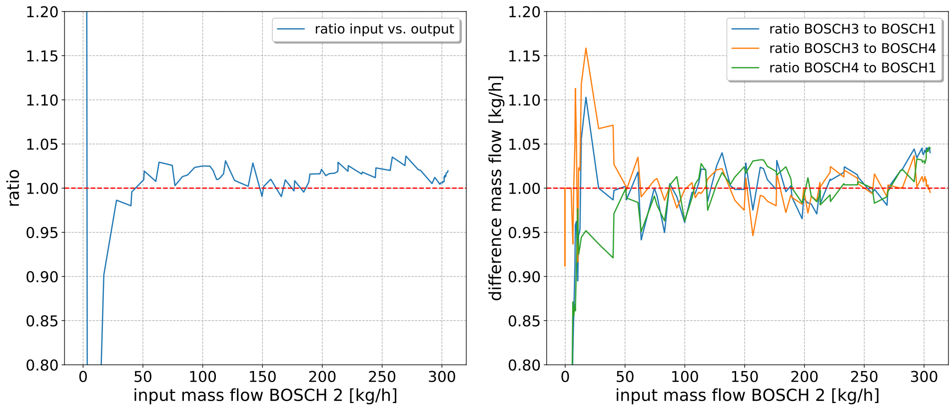

Figure 6.7: Ratio between inlet air and the sum of outlet flows. Except of some inconsistencies at very small flows the measured air inlet flow compares well within maximally 5% deviation to the measured sum of air flows measured at the outlets. This confirms the reliability of the pre-calibration, as well as the air sealing of the system.

6.4 Outlet Mass Air Flow Sensors

Figure 6.8: Adiabatic guide adapters put on each outlet to calibrate the FLW122 MAF sensors and to measure the amount of air flowing through each outlet. The inner diameter of the prolongation tube is $d_{pt} \simeq 38.7$ mm. The FLW122 sensor pins are held and screwed into a special circular-shaped housing that can be plugged onto the prolongation tube.

The FLW122 MAF sensors do not come pre-calibrated. Therefore, each of them needs to be calibrated separately in place, meaning connected to the individual ADP outlet of the later intended measurements. Hereby sequentially one outlet was left open with all others closed such that all air ran through the input sensor and the calibration sensor to calibrate at the outlet. The reason for this calibration setup is that with such a setup one can exclude any effects – like turbulence – induced by the ADP to impact the later measurement, since these effects would also happen during calibration and hence are corrected for. Therefore a calibration which is carried out in the ADP itself would probably be more accurate. A calibration procedure that is similar to the BOSCH calibration would be suitable for a fairly homogeneous input air flow distribution at the input of the measurement tube. In reality this is not necessarily the case, hence this *in-situ* calibration of each individual tube/sensor at its later measurement position should provide a more precise measurement. Due to the fact that the sensors do not come with a special housing but just as small area sensor panel, a mechanical construction fitting to the outlets of the ADP is required. Also all the sensors must be placed in a reproducible and equal manner above the outlet area to make meaningful statements about how much air flow is coming through. For this purpose, special adapters were developed (cf. Fig. 6.8) to measure the air flowing out of the outlets easily and reproducibly. Their bottom parts are constructed such that they fit into the rectangular-shaped outlets. It has to be mentioned that 3D printing bears some problems as objects are not produced accurate to millimeters and some adapters are plugged in a bit looser, such that small air leaks are not excluded. The rounded shape of the adapter is such that the air streamlines will remain as uniform as possible. On top of the adapter there is a grid with rectangular pieces with the task of minimizing turbulence and homogenizing the flow. Simple prolongation tubes are placed onto the adapters in order to reach a fully developed flow. The size of the tube was wisely chosen such that its length exceeds the entrance length. Since the amount of air flowing through each outlet is significantly smaller than through the inlet (roughly one seventh as large), this reduces the Reynolds number and finally the entrance length.

The calibration procedure can be described as follows: each sensor is assigned an individual outlet and its position will not be changed (sensor 1 to outlet 1, sensor 2 to outlet 2,...). Each individual sensor is calibrated in an separate measurement. The outlets that are not involved in the current measurement are closed on the top side of their prolongation tubes with adhesive tape. For example if sensor 1 is calibrated, only outlet 1 will be opened and outlets 2–7 will be closed. If sensor 2 is calibrated, then outlet 1 and 3–7 are closed, while outlet 2 is opened and so on. In this constellation, all the air flowing through the inlet is forced through the outlet on which the sensor sits. As the inlet MAF is monitored by a pre-calibrated BOSCH sensor, one can deduce a calibration curve for each FLW122 sensor by setting a linear ramp of blower frequencies and to scan the sensor voltages from small to high air flows. Minimum and maximum blower frequency can be set after some simple considerations. A maximum MAF of roughly 350 kg/h is provided by the blower if all the outlets are opened. However, the blower does not need to be exploited in its full range. For the case of fully homogenized air flow, each outlet would get $\frac{1}{7} \cdot 350\text{kg/h} = 50\text{kg/h}$ of air. But since the air flow is still inhomogeneous and for safety reasons (if for example some special tests have to be performed in the future) the maximum value should be much greater. A minimum value of 0 kg/h and a maximum of 150 kg/h has been chosen for these scan. Hereby, lower input air flows feature a larger variance which is unavoidable and needs to be taken into account when interpreting the later results. A measure to prove whether the set of seven calibration curves is consistent and reliable is the introduction of a cross-check. The measuring principle remains almost the same as for the calibration method, despite the fact that now a fixed sensor (in this case sensor 1) measures the air at each outlet with the other outlets being closed. The inlet MAF is plotted against the seven outlet MAFs. The calibration can be considered successful and trustworthy if the seven curves do not differ from each other and lie on the angle bisector. A series of calibration measurements have been taken.

The first cross-check results revealed a large spread of the air distribution among the outlets. This could be improved as air leaking through small gaps between the adapter and the ADP were observed. The adapters have been fixed more tight to the plate by means of isoprene-isobutylene caoutchouc (butyl rubber). A second measure was to replace the linear blower frequency ramp by approaching individual frequencies and measure over a certain range of time, in this case 1 minute, and finally averaging both output values with a binning method. This allows the small fluctuations of the inlet MAF to be better taken into account. The result of the cross-check is shown in Fig. 6.10. The calibration has to be described by the best fit model. Usually for the calibration of MAF sensors a 2nd-degree polynomial function is used. This setting did not produce inlet to outlet ratios and outlet air distribution (in later measurements) to a satisfactory degree. The system has special pressure and turbulence conditions with bigger impact at larger air flows. These effects can be removed by taking higher polynomial degrees.

The best setting that was found can be seen in Fig. 6.9.

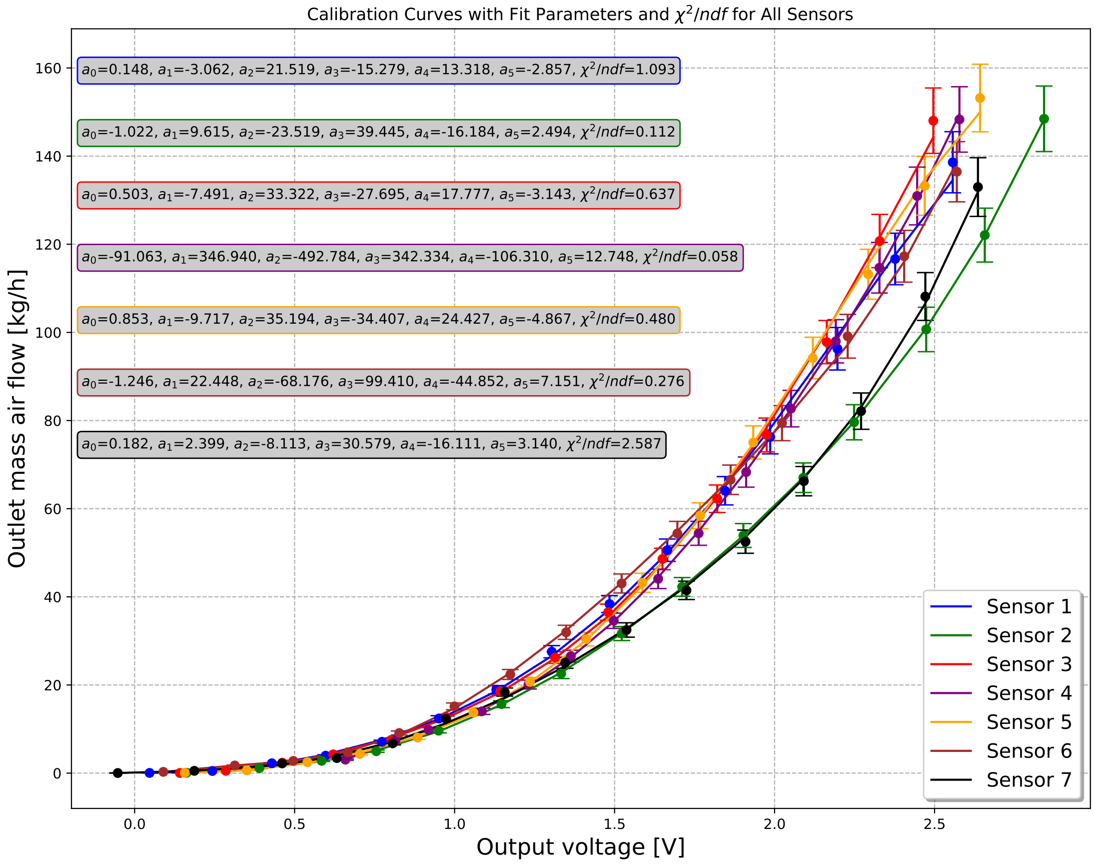

Figure 6.9: Calibration of the seven FLW122 MAF sensors which are used to measure the mass air flow at all positions inside the camera system. The data is fitted with a fifth-degree polynomial function. The fit parameters a_0,...a_5 and the χ^2/ndf values are shown in the colored boxes.

Each sensor data is fitted with a 5th-degree polynomial function with a constant offset:

$$MAF(V) = a_0 + a_1 \cdot V + a_2 \cdot V^2 + a_3 \cdot V^3 + a_4 \cdot V^4 + a_5 \cdot V^5. \tag{6.2}$$

The graph shows the MAF at different output voltages for 10 points per sensor approached. The uncertainty takes into account statistical (χ^2-method was used) and systematic (an accuracy of 2 % was assumed) effects in the following way:

$$\sigma_{tot} = 1/N \cdot \sqrt{\sigma_{stat}^2 + \sigma_{sys}^2}. \tag{6.3}$$

The χ^2/ndf values are all close to 1 and thus the fits are valid. For some sensors (2,3,4,5,6) they are slightly overestimated, while for sensor 7 it is slightly underestimated and the error of sensor 1 seems to be well-matched.

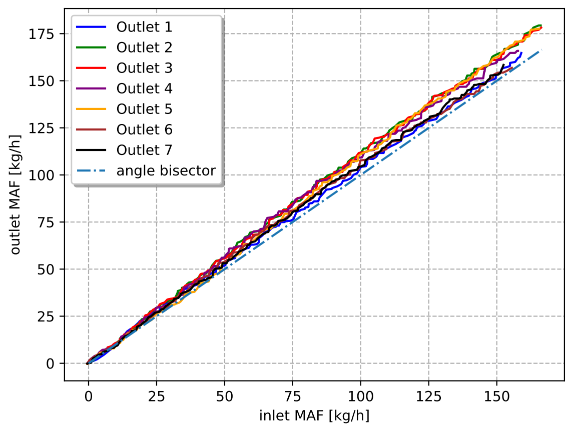

(a) One specific sensor (in this case it is number one) is placed on each associated outlet, while each of the other six outlets are closed, and measures the air flow in the given range. In the ideal case, one would expect no difference between the seven curves recorded (all graphs should lie on the angle bisector). The real measurements show only small differences between the outlets and the air flow is systematically overestimated (see right plot).

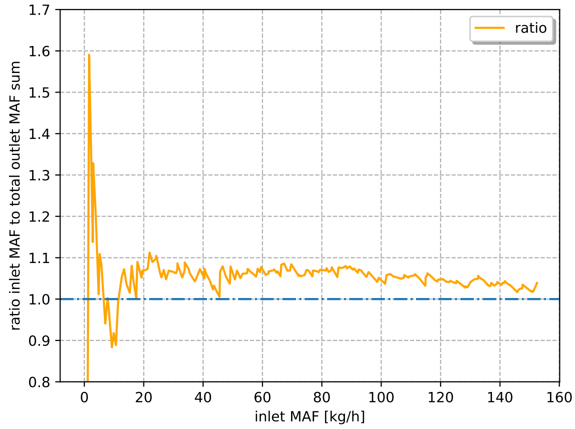

(b) Inlet to outlet ratio of the cross-check. The MAF is plotted against the sum of all outlet MAFs. Except of an unknown instability for small air flows, as they were already seen in the inlet MAF sensor calibration, the calibration seems to be stable and reliable for air flows above 20 kg/h. This is sufficient as in full operation for the whole camera, MAF clearly exceeding 100 kg/h will be used.

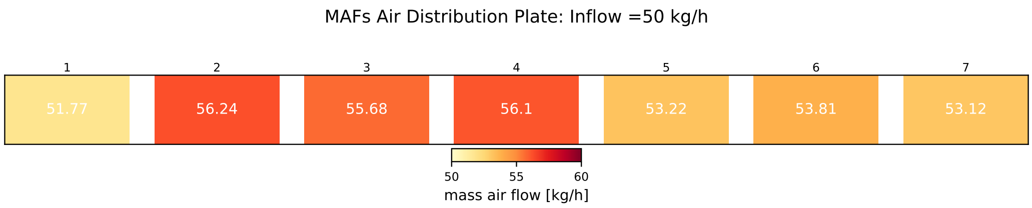

(c) Color plot of the cross-check at one fixed MAF of 50 kg/h. It shows the reliability of the cross check measurement at fixed inlet MAF of 50 kg/h, where the system has not fully reached its accuracy, as shown in (b). The range of the color scale is limited to ± 10 kg/h.

Figure 6.10: Cross check measurement of the FLW122 MAF sensor calibration.

With the inlet and outlet MAF sensors being calibrated, they can be used for all kinds of measurements that are equal or at least similar to the calibration setup conditions. The calibration allows to determine the MAF distribution among the outlets for a range of blower frequencies and therethrough to get an idea of the inhomogeneity of the system, which will be elaborated in the following chapter. The calibration parameters are summed up in Tab. 6.1. One of the most important findings is that the outlet MAF sum is slightly larger (5–10%) than the amount of air that is distributed through the inlet.

Table 6.1: Calibration parameters of the inlet MAF sensors (of type BOSCH) and outlet MAF sensors (of type FLW122).

	Inlet MAFs (BOSCH 1-4)	Outlet 1	Outlet 2	Outlet 3	Outlet 4	Outlet 5	Outlet 6	Outlet 7
a_0	-28.00507	0.148	-1.022	0.503	-91.063	0.853	-1.246	0.182
a_1	31.96391	-3.062	9.615	7.491	346.940	9.717	22.448	2.399
a_2	-5.37310	21.519	23.519	33.322	492.784	35.194	-68.176	-8.133
a_3	0.66098	-15.279	39.445	-27.695	342.334	34.407	99.410	30.579
a_4	1.19383	13.318	-16.184	17.777	-106.310	24.427	-44.852	-16.111
a_5	-	-2.857	2.494	3.143	12.748	4.867	7.151	3.140

7
Results

In the following chapter, the results of all studies regarding lateral outlet air distribution, backpressure and column heat dissipation will be discussed and interpreted in the sense of possible application scenarios for the CBM experiment. Air flow measurements will be compared to corresponding CFD simulations. In particular, the inhomogeneous air mass distribution along a column is compared to the resulting heat distribution. Furthermore, it will be investigated whether a different slit size of the backplane cooling mask has a possible positive effect on air flow homogenization inside the column.

7.1 Setup of the Experiment

The air flow distribution measurements were performed in the right half of the camera prototype and the setup is similar to the calibration setup. At this point, the half was not yet equipped with all backplanes. The adiabatic adapters with prolongation tubes were attached onto each outlet. The sensors are connected to the slow control interface. They can be directly read out through the ADCs and a readout script on the RaspberryPi computer writes the output voltages into a csv-file. Each sensor is assigned to its corresponding column and outlet (cf. Fig. 7.1).

Figure 7.1: Measurement setup. Both halves of the camera is divided into seven columns. Each column is provided with air through its corresponding outlet.

The air produced by the side-channel blower is guided from the air-water heat exchanger via a polyvinyl chloride (PVC) hose and an additional prolongation tube into the inlet of the ADP. The heat production by a single camera column and its cooling was investigated at a later stage in the left camera half which was fully equipped with backplanes and readout electronics. For that the air is guided through the inlets of both ADPs (bottom and top). An additional adapter splits up the air coming from the PVC hose into two parts which is then guided by two smaller prolongation tubes to the inlets. Unlike in the later real experiment, all cooling measurements are carried out in an open-loop.

7.2 Setup of the Simulation

The workbench structure is processed from top to bottom (cf. Fig. 7.2a). After loading and editing the geometry as well as creating a mesh, the simulation can be set up. As a first step, it can be chosen between a transient and a steady solver. Since time-dependent components of the air flow are negligible in the experimental setup, the steady solver was chosen. Then the fluids and solids of the system have to be characterized. Air is chosen for the fluid domain, while aluminum is chosen as a material for the ADP and the backplane cooling masks (cf. Fig. 7.2b). Afterwards, characteristics of the flow, such as the turbulence model that has to be used, can be defined. Ansys Fluent has a wide range of boundary conditions that allow flow to enter and exit the solution domain. One can choose as inlet boundary condition between the following options: velocity inlet, pressure inlet, mass flow inlet, pressure outlet, pressure far-field, outflow boundary, inlet vent, intake fan, outlet vent and exhaust fan [21]. In this case it is most appropriate to choose mass flow inlets, which is commonly used for compressible flows to prescribe mass flow rates at inlets. It permits the total pressure to vary at a fixed mass flow rate in response to the interior solution which is in contrast to a pressure inlet. An exemplary calculation for the inlet turbulence modeling based on the formulae presented in chapter 3 is shown in the appendix A. All other setting possibilities like fluid temperature or gas mixture have been left at the default values. Parametric studies allow to simulate the setup for a series of different inlet MAFs. Depending on the turbulence model, at least two turbulence parameters, in this case the turbulent kinetic energy (TKE) and the eddy viscosity ratio (μ/μ_t) need to be defined. As exit boundary conditions, pressure outlets will be used (red arrows in Fig. 7.2b), as they define the static pressure at flow outlets when backflow can occur, and empirically show better convergence behavior. In the settings of the wall boundary conditions, the surface roughness can be specified, which is left at default value 0.5. A rough wall surface can produce turbulence and additional pressure but was not considered here. Symmetry boundary conditions are used if the geometry and its expected flow pattern have mirror symmetry. This will be important when simulating a camera prototype setup with a column that interconnects the upper with the lower ADP. The symmetry plane can be determined by the center of gravity of the system. Its interaction faces are defined as the symmetry boundaries. After setting convergence criteria and initializing the simulation, the solver type as well as the number of iterations and the iteration step size can be set. The simulation can be run by pressing *Run Calculation*.

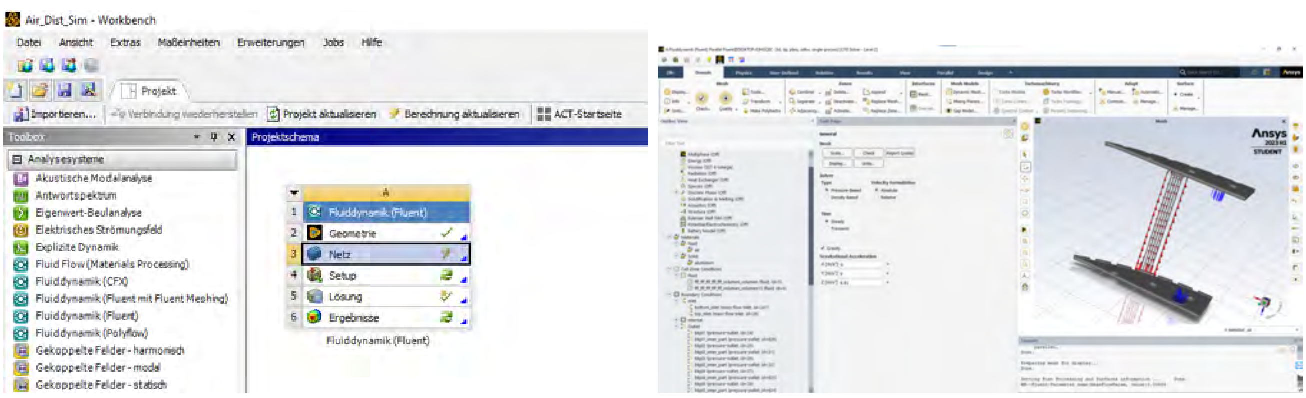

(a) Ansys Workbench structure. **(b)** Setup interface of the simulation.

Figure 7.2: Screenshots of the Ansys Fluent Workbench and setup interface.

7.3 Air Flow in the Air Distribution Plate

Previous simulations have already been run by a group of researches at the University of Warsaw. On the basis of their results, they developed a homogenization concept of the ADP. Small pieces that should be attached to the interior of the ADP ought to direct streamlines more evenly distributed among the outlets. The pieces are extracted from the CAD geometry and have been printed. After being fixed with glue into the ADP, a measurement has been performed for a ramp of different MAFs. In the analysis of the outlet MAF distribution no optimization of the air flow could be observed. The pieces only lead to a change in the order of the outlets. Also, predominantly laminar flow is claimed. For these reasons, a homogenization concept following a manipulation of the streamlines in the volume inside the ADP has been discarded. The very first CFD simulations within the framework of the thesis have been performed with the fluid flow package of COMSOL Multiphysics, which is a different simulation software. Within the scope of the license provided, it differs from Ansys Fluent mainly in that only incompressible flows as well as turbulence models can be considered. The first results did not match the experimental observations. This is why the switch was made to Ansys Fluent. Some plots of both preliminary studies can be found in the appendix (cf. Fig. B.1 & B.2).

7.3.1 Measurement

To measure the homogeneity in the air distribution towards all outlets of the ADP the calibrated sensors are now all connected at the same time to the plastic adapters used already before. The sensor pins will be plugged on as centrally as possible (cf. Fig. 7.1). Hereby their relative orientation plays no crucial role: in some tests the air coming through each outlet was observed in different angles of the sensor pin which did not reveal any difference. The blower is operated at full range from 50 kg/h to 300 kg/h in steps of 50 kg/h. To account for the small fluctuations of the inlet MAF, time-averaged measurements were performed for each of the seven blower settings. A total time of 1 minute was chosen. The results are shown in Fig. 7.3. The plots show for each inlet the corresponding outlet MAFs as a function of time, together with their mean values and a light-shaded uncertainty band describing systematic and statistic uncertainty of the mean. In the header of each plot, the inlet flow, the sum of the outlet flows and the percentage deviation of the actual value from the the setpoint is displayed. The deviation seem to be in agreement with the overestimation of the outlet air sum that was already seen in the cross-check measurements, however, slightly increases for higher air flow. Irrespective of this overestimation, one immediately notes the inhomogeneity in the air output between the different outlets. Moreover, the order of which outlet receives most and which outlet the least amount of air can be seen. This ordering seems rather independent of the total air flow fed into the system. Outlet 7, having the largest distance from the inlet, has always the least air flowing through. Conversely, most of the air flows through outlet 1, albeit having the second shortest path to the inlet. From geometric arguments one would naturally expect most of the air flow passing through outlet 2 (cf. Fig. 4.4). Moreover, one of the cylindrical cutouts is located exactly between inlet and outlet 1 & 2, but obstructing more area of outlet 1, acting as an obstacle. Nonetheless, it is likely that this artefact creates turbulence and directs more air to outlet 1, which should be reflected in the simulations.

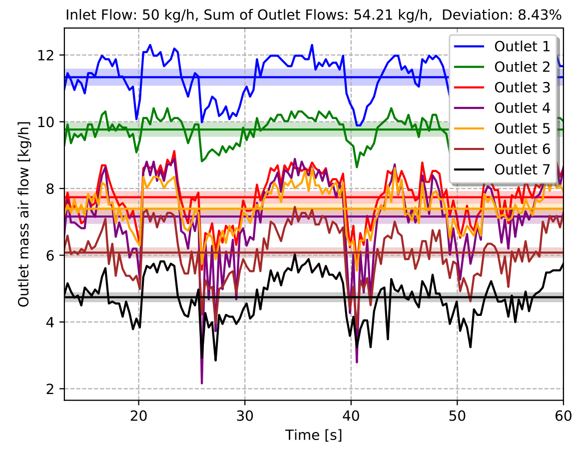

(a) Inlet Flow: 50 kg/h

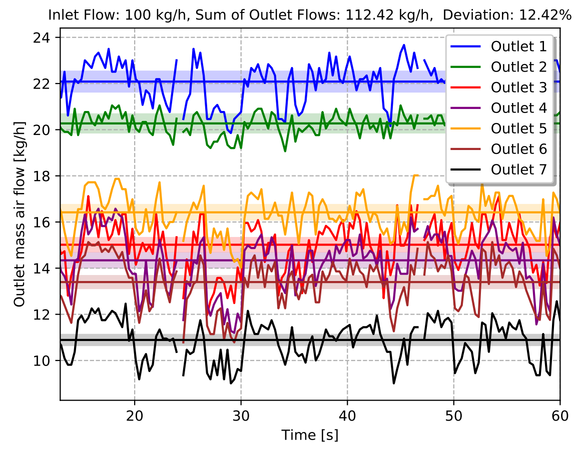

(b) Inlet Flow: 100 kg/h

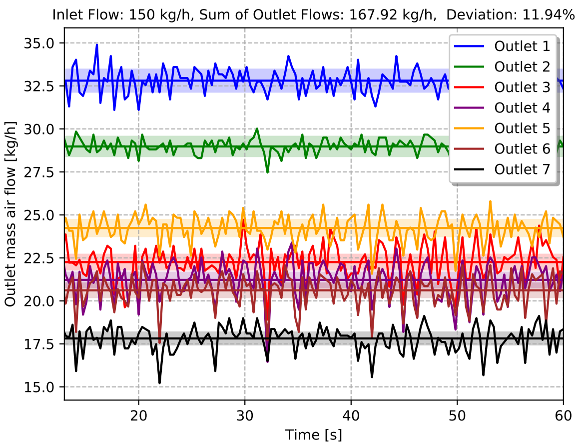

(c) Inlet Flow: 150 kg/h

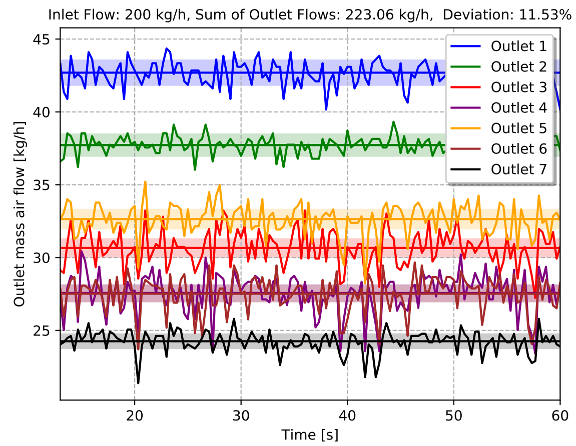

(d) Inlet Flow: 200 kg/h

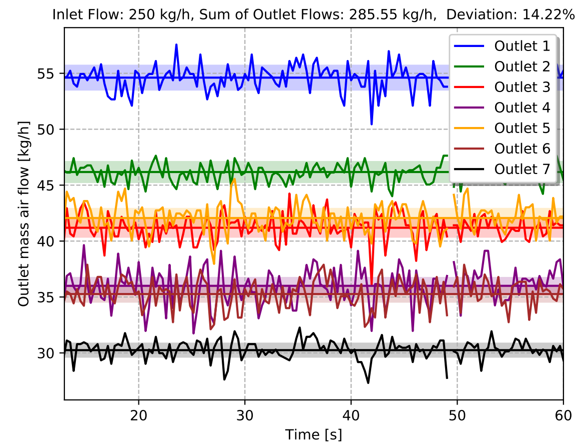

(e) Inlet Flow: 250 kg/h

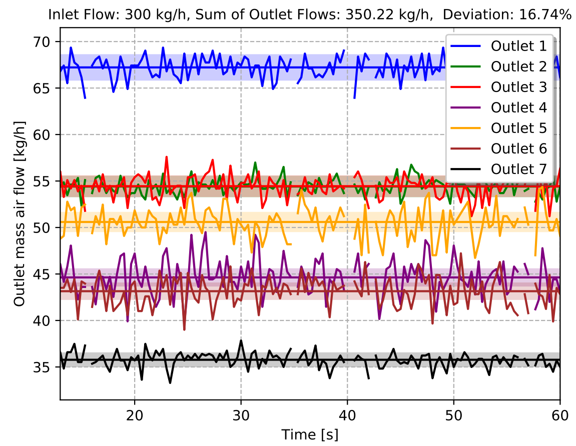

(f) Inlet Flow: 300 kg/h

Figure 7.3: Flow for each of the seven ADP outlets (cf. Fig. 4.4), measured for six different inlet MAFs. Average value shown by straight line and standard error of the mean shown by the shaded area.

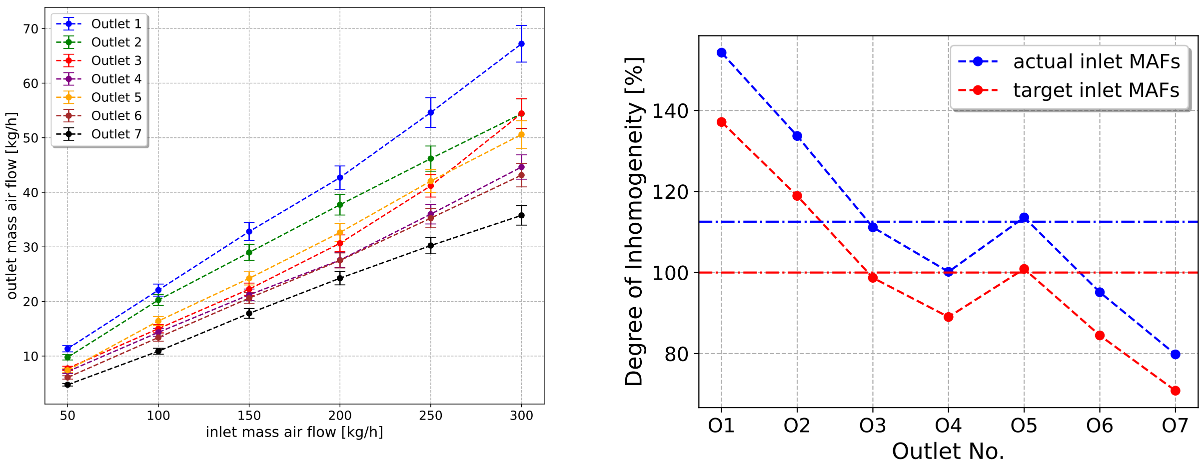

(a) Outlet MAF distribution for six different inlet MAFs. The global trend shows a dominant air flow towards the outlets that are closer to the inlet hole (O1-O3). The most distant outlet O7 shows the least MAF. However, some effect(s) seem(s) to impact the hierarchy with respect to inlet distance, i.e. the MAF of O5 is larger than for O4. The error takes into account statistical (from the χ^2-approach) and systematic (sensor accuracy) effects.

(b) Inhomogeneity d for each outlet. It describes the percentage deviation of the individual outlets from the case of fully homogenized air flow and is additionally averaged for all inlet MAF. The middle outlets deviate least from the case with fully homogenized air flow. This parameter can be trailblazing for an air homogenization concept as one knows by how much the air flow could be augmented or reduced in the corresponding outlet.

Figure 7.4: Outlet MAF distribution inhomogeneity.

The time-averaged outlet MAFs can be plotted against inlet MAFs for different outlets. This is shown in Fig. 7.4a. As discussed above, an outlet hierarchy can be observed, with the only exception being for 300 kg/h. Apart from that, the overall trend can be described as roughly linear. A linear fit is nevertheless not carried out at this point, since it is dealt with turbulence which is a highly non-linear process. From these values, each outlet can be assigned a certain level of inhomogeneity. In this case, the inhomogeneity d will be treated as the relative deviation of the actual outlet MAF to the target outlet MAF which is always a seventh of the current inlet MAF. The results are presented in Fig. 7.4b. The plot shows the degree of inhomogeneity d_j, averaged for all of the six blower frequencies i, and the mean degree of inhomogeneity d averaged over all outlets j:

$$d_j = \frac{1}{6} \sum_{\text{i=50 kg/h}}^{\text{i=300 kg/h}} d_i, \quad \text{where} \quad d_i = \frac{\text{actual flow at outlet j}}{\text{expected flow at outlet j}} \quad \text{and} \quad d = \frac{1}{7} \sum_j d_j \tag{7.1}$$

The outlets that are closer to the inlet are supplied proportionally with an excess of air compared to more distant outlets (see also Fig. 7.5). The goal for an homogenization concept would be to reduce this excess. A manipulation of the ADP with 3D-printed plastic parts taken from a simulation that predicts air flow homogenization by this modification, was discarded due to conflicting measurements. As mentioned in chapter 4, the ADP will be equipped with movable plastic sliders that can reduce the outlet area. A significant improvement would have to be observed by, for example, pushing the first three outlets with the plastic sliders to different degrees of closure, such that the system can stabilize. This measurement was not performed here, as it strongly depends on the backpressure produced by the electronic equipment and the heat distribution along each column, so that it would have to be readjusted again anyway.

Some final thoughts can be made regarding the reliability of the results: (1) does the air temperature, which is slightly rising during the time-averaged measurements affects the functionality of the FLW122 sensors? (2) How can be ensured that the outlet MAF values are consistent values, if the small sensor pin is located at the center of the prolongation tube, not taking into consideration possibly occurring uneven flow from the tube? The first question can be answered with the CTA-based working principle of such MAF sensors. The air temperature influences the density of the fluid (air), which in turn has an impact on streaming properties. For higher temperatures, the density decreases leading to an increase in volume and a reduction in flow velocity if the MAF is kept constant. However, the sensors are not volumetric but measure air mass. A change in (ambient) temperature, i.e. the temperature recorded by the sensor R_S leads to a change in temperature of the heater R_H as well because the temperature difference $\Delta T = T_H - T_S$ is always tried to be kept constant, notwithstanding that for example less dense (more expanded) air would cool the sensor less strongly. Hence in a first approximation, the sensors therefore work independently of the air temperature. The changes in temperature are comparably low (only $\approx$ 2–3 °C), influencing the air density only to a minimal extent, such that in second order temperature effects would be negligible anyway. Regarding the second question, simple measurements were performed by hand and with the help of a volumetric manometer that can measure wind speeds. Without adapters, the air flow leaving the ADP openings was observed to be strongly inhomogeneous. Only very few air is pushed out through the right side of the outlet, the rest being pushed out in the center and the left side. When the adapters, whose main purpose actually is to homogenize the air stream, where plugged on again, no significant difference could be found between the inner and the outer part of the circular opening. This seems to agree with the preliminary considerations of fully developed flows. However caution is advised, since these openings are smaller than the sensitive area of the manometer itself. Whether the air flow is really bypassing the sensor pin homogeneously, can be subject of the simulations. An additional argument for the consistency is that the sensors were reproducibly calibrated in the same position.

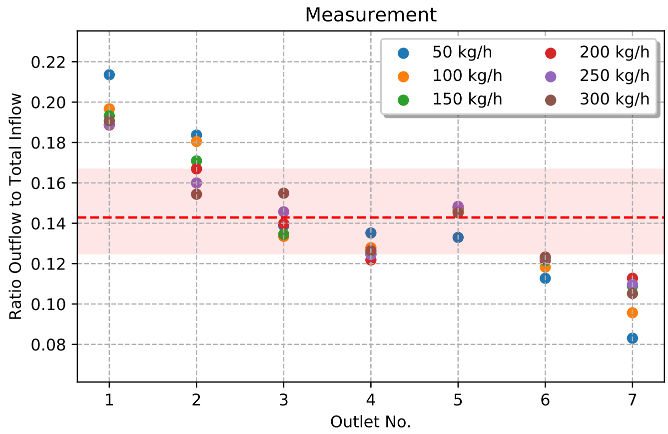

Figure 7.5: Observed inlet to total outlet sum ratio compared to the fully homogenized scenario.

7.3.2 Simulation

The first simulations were performed for a single inlet MAF in a geometry where only the ADP is included. One result of the simulation can be seen in Fig. 7.7a in form of the simulated outlet MAF distribution and in Fig. 7.7d, where a transparent wireframe model of the ADP is shown. It shows the mass flow contour observed at the inlet and through the seven outlets. A first observation is that the air flow seems to be fully developed at the inlet. Wide parts of the circle reach maximum MAF (and thus fluid velocity) whereas they decrease significantly in a small ring at the outer edge such that the no slip boundary condition is fulfilled. By taking a closer look at the outlets a strongly inhomogeneous

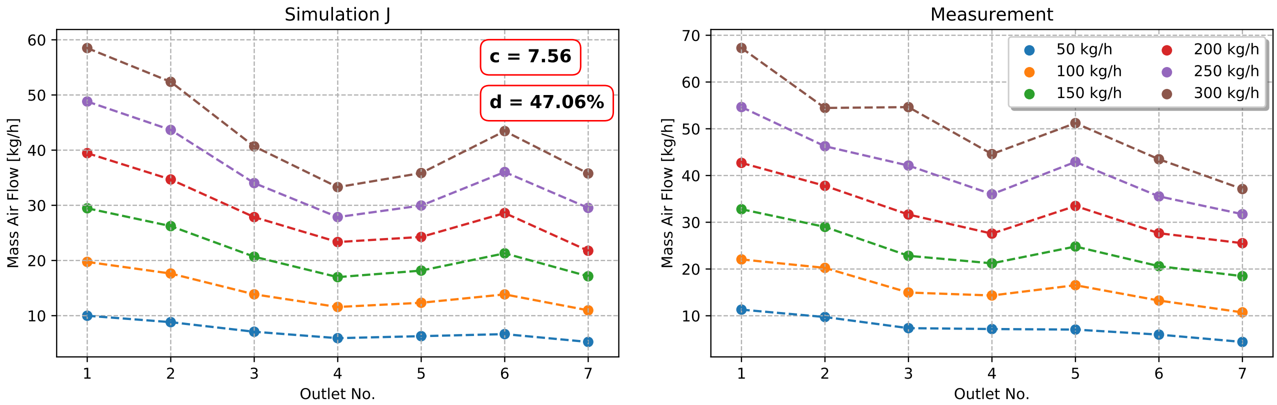

(a) Outlet MAF distribution for the best simulation setting J at different inlet MAFs. Additionally, the c-parameter, validating consistency and accuracy of the simulation.

(b) Actual measured outlet MAF distribution at different inlet MAFs. As already discussed above, the global trend agrees with the simulation.

Figure 7.6: Comparison between outlet air distribution measurements and best simulation setting J.

behavior can be observed. Since the fluid direction is opposite compared to the flow through the inlet, colors towards red have to be interpreted as small and colors tending to blue mean high air flow. Except of outlet 1 & 2, all ADP outlets tend to have higher air flows towards the left side. This perception is in agreement with the abovementioned observations seen in measurements. As the simulation setup proved stable and the solution converged (at least to 1e-4), in the next step the geometry could be extended by the adapters. Their curvature is large, so it was necessary to sacrifice something in the resolution of that curvature, due to a restriction of the number of cells in the student version of Ansys. An example of first results with this geometry is shown in Fig. 7.7a-c. Hereby (a) shows the distribution of velocity vectors simulated in each cell in magnitude and direction. First indications of a reason for the observed higher mass flow through outlet 1 are discernible. Regions with small (in vicinity to outlets 3-5) and high fluid velocity are apparent. To answer question (2) of the previous section one can take at look at a birds-eye view on the prolongation tubes shown in (b) and (c). With the exception of minimal deviations, the fluid velocity and the MAF through the openings of the tubes are largely homogeneous. For these reasons it is justifiable to measure the air flow with the FLW122 MAF sensors exactly at these positions in the center of the opening to obtain reliable statements and to compare them with simulation results.

Whether the simulation setup can be trusted in terms of physics, i.e. whether the underlying turbulence model best describes the real conditions, remains to be studied. Also, in terms of consistency, it is to be verified whether the mesh size and number of maximum iterations is set adequately. For this purpose, a total of 12 different simulation setups were studied (cf. Tab. 7.1). The density solver defines the fluid as a continuous medium and assigns a density to each point in space. Generally, it is rather used for transient (time-dependent) flows. Further, it is used where the density changes very much in a short period of time (for example shock waves or detonations), leading to high Mach numbers. The pressure solver, which is set as default here, is used for steady-state applications where the density is assumed to be constant and is beneficial for incompressible flows in terms of convergence. Pressure based solvers use mainly the SIMPLE(C) (semi-implicit method for pressure-linked equations - corrected) algorithm. This is an iterative method to solve the coupling of pressure and velocity. The PISO (pressure implicit with splitting of operators) algorithm is an extension of SIMPLE(C) for more complex air flows and

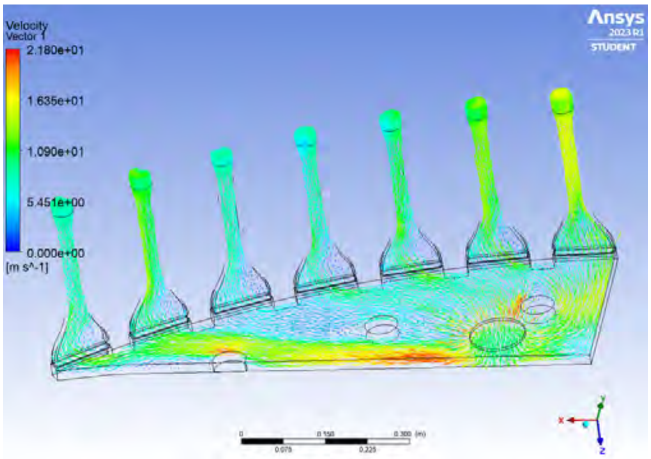

(a) Velocity vector evolution in the ADP and the adiabatic guides. The outlet numbers read 1 to 7 from right to left.

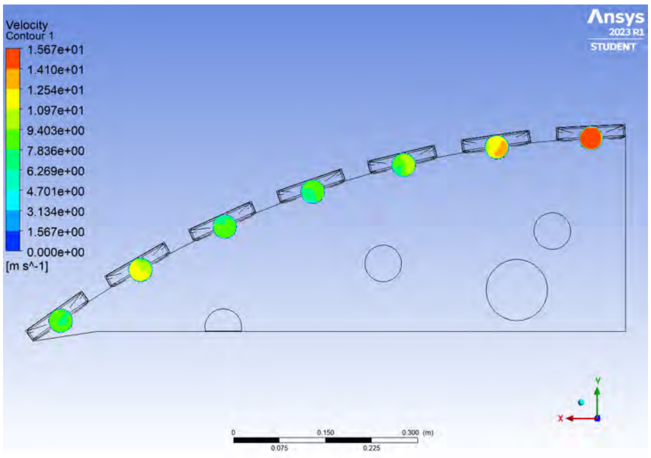

(b) Birds eye view on the openings of the adiabatic guides. The color scale shows again the air velocity. The outlet MAF distribution is largely homogeneous.

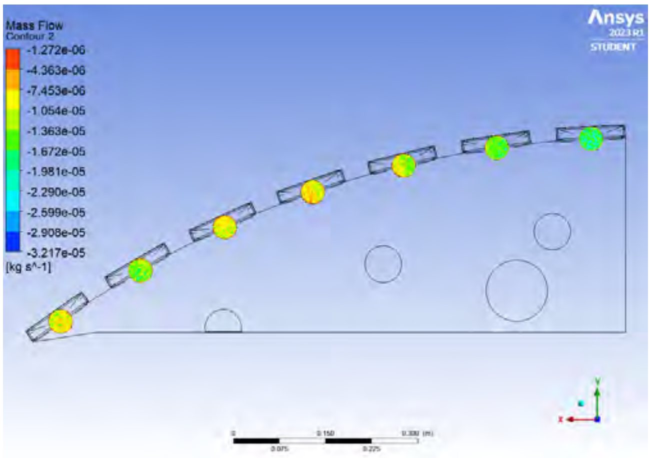

(c) Birds eye view on the mass air flow through the outlets of the guides.

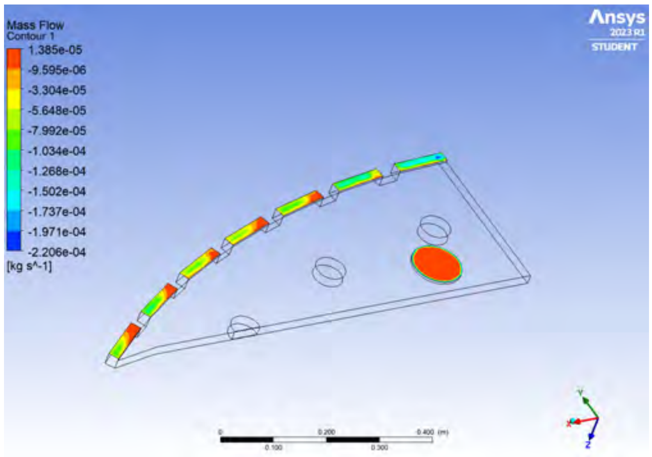

(d) Fully developed inlet air flow and inhomogeneous outlet outflow.

Figure 7.7: Simulated CFD parameters of the calibration setup.

larger pressure gradients. To assess the validity of the individual simulation a parameter accounting for both, the accuracy and the consistency is introduced:

$$c = \frac{1}{6} \cdot \sum_{\dot{m}_i=1}^{6} \cdot \left[\sqrt{\sum_{o=1}^{7} \frac{1}{7} (\dot{m}^o_{meas} - \dot{m}^o_{sim})^2} \right]_{\dot{m}_i} \tag{7.2}$$

It takes the difference between the measured $\dot{m}_{meas}$ and the simulated $\dot{m}_{sim}$ MAF for each outlet which is then summed up and averaged by the number of outlets and finally averaged for each inlet MAF. This means that for accurate simulation setups c will be small, i.e. in well agreement with the measurements. Further, if the simulation is consistent, it will remain constant if the mesh size is reduced or the number of solver iterations is increased.

The calculated c-parameters are all within the range of 7–8. Simulation J exhibits to be the best simulation setup with the k-ω as turbulence model. A laminar or a k-ε model lead to small deterioration. Hence the k-ω model will be used for all future simulations. This is comprehensible as the k-ω model is an extension of the k-ε model. Compared to its predecessor it is more suitable for near-wall flows, regions

Table 7.1: Simulation settings and calculated c-parameters. Different turbulence models, solvers and mesh sizes are used. As a default setting, the k-ω model was used.

Simulation	Model	c
A	k-ω	7.686
B	laminar	7.768
C	k-ε	7.700
D	density solver	no solution
E	PISO solver	no solution
F	SIMPLEC solver	7.884
G	Large Turbulent Viscosity Ratio	7.704
H	Mesh size: 0.008 m	7.657
I	Mesh size: 0.007 m	7.632
J	Mesh size: 0.009 m	7.560
K	Automatic mesh for ADP and Adapter	7.603
L	Max. iterations = 5000	7.679

with large pressure gradients and takes better account of the anisotropy of turbulence, i.e. regions with strong directional dependence of the flow. All three aspects occur in the underlying situation. Moreover, c does not change significantly with finer mesh size or larger number of iterations. Based on these considerations, this simulation is considered as reliable. Later analyses show that increasing backpressure in the system yields in even better matching between simulation and measurement (cf. subsection 7.5.1). Simulation J is compared with the measurements for different inlet MAFs in Fig. 7.6 and 7.8. The global trend of the simulation is in line with the measurement. It tends to suite better for small air flows than for larger ones. The biggest difference is that a kink upwards in MAF occurs at outlet 5 instead of outlet 6. Visibly, the inhomogeneity between the different outlets is reflected well at lower input MAFs whereas at higher input MAFs the inhomogeneity larger in simulation than in the measured data.

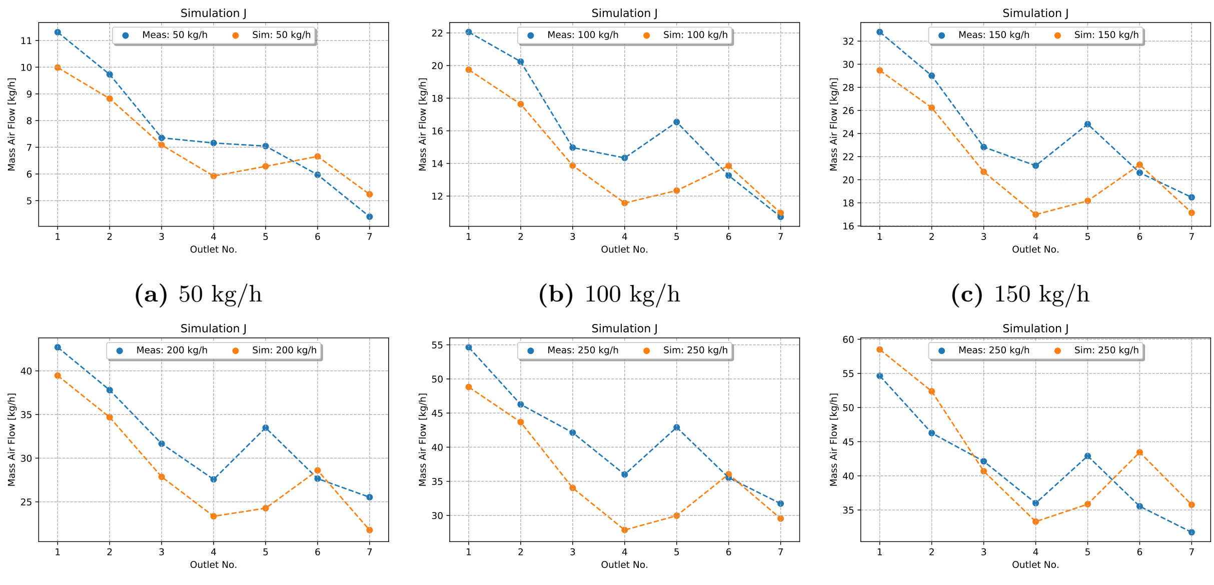

(a) 50 kg/h

(b) 100 kg/h

(c) 150 kg/h

(d) 200 kg/h

(e) 250 kg/h

(f) 300 kg/h

Figure 7.8: Comparison between outlet air distribution measurements and best simulation setting J for each inlet MAF. Simulations and measurements agree quite well.

7.4 Air Flow within a single Camera Column

After assessing the inhomogeneities between the different outputs the next step is to measure the inhomogeneity in a vertical column. This is mainly done with simulations as the measurement concept could not have been carried out. It will also be discussed whether different design options for the slit sizes of the backplane cooling masks can have some benefits.

7.4.1 Measurement

A concept has been drafted in order to measure the vertical air flow distribution coming out at the level of each backplane. Special holders were printed which made it possible to attach the FLW122 as well as the BOSCH sensors. Time-averaged measurements have been recorded with this setup. Unfortunately, the results that were obtained are physically not meaningful. The air flows are too low for the BOSCH sensors to work reliably. The FLW122 sensors are basically detached from the camera system such that the flow is not fully developed and their calibration do not provide accurate results. Consequently, the air flow along the columns was only simulated and it can be inspected whether it matches in some way the heat distribution for a fully equipped and commissioned column, as measured later.

7.4.2 Simulation

A 3D CAD model exists including two ADPs that are identical in construction for the bottom and top part of the camera half (cf. Fig. 7.9). The plates are interconnected with seven backplane cooling masks, each of them guiding the air from the outlet towards the center. As a consequence, two inlet flow boundary conditions are required. The target MAF that is led into the system is always equally split up into the top and the bottom inlet. For example, if a total inlet MAF of 100 kg/h is chosen, then 50 kg/h is led through the top and 50 kg/h is led through the bottom inlet. The masks come in two versions: one with equal slit sizes and one with slit sizes that were designed after fluid mechanical considerations, having larger slits towards the center and smaller ones at the outer parts of the mask. In this study, column 4 is taken as a showcase. After removing the columns that are not of interest and sealing their outlet on the ADP, a volume extract corresponding to the fluid domain was created, and each slit size was assigned a surface component which is important in order to define the boundary conditions.

Since the slits are very small and the gradients are sometimes very large, a finer meshing is required, especially for the regions around and including the slits (cf. Fig. 7.9a). A parameter that validates the mesh quality is the skewness. It evaluates to what extent the edge and angle of the created mesh deviates from the ideal state, i.e. equilateral triangle / square. A recommendation is that maximum value of the skewness should never exceed the value of 0.95 while the mean value should not be greater than 0.35 [22]. Except for two faces at the rear edge of the ADP, this condition is always fulfilled (cf. Fig. 7.10b).

The mask consists of a total of $7 \cdot 14 = 98$ slits. Each slit is defined as pressure outlet boundary condition. These slits are grouped into groups of 14. Each group of slits corresponds to the cooling of a

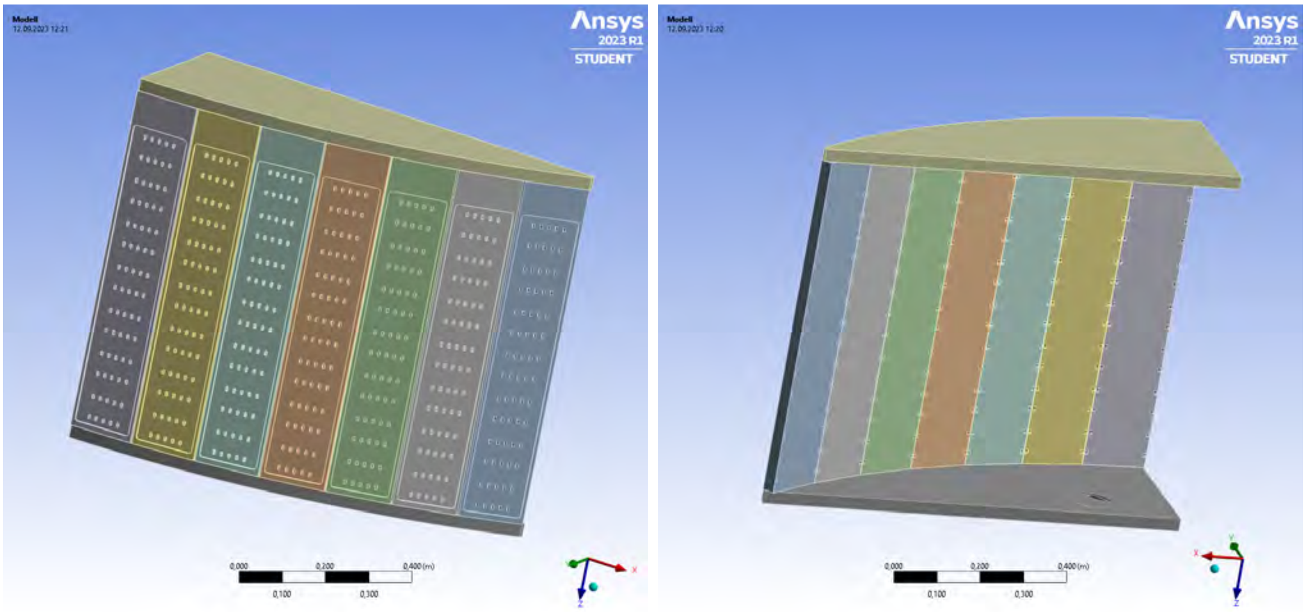

(a) Beam downstream view.

(b) Beam upstream view.

Figure 7.9: Full-size model of one of the CBM-RICH camera prototype halves implemented in Ansys Fluent.

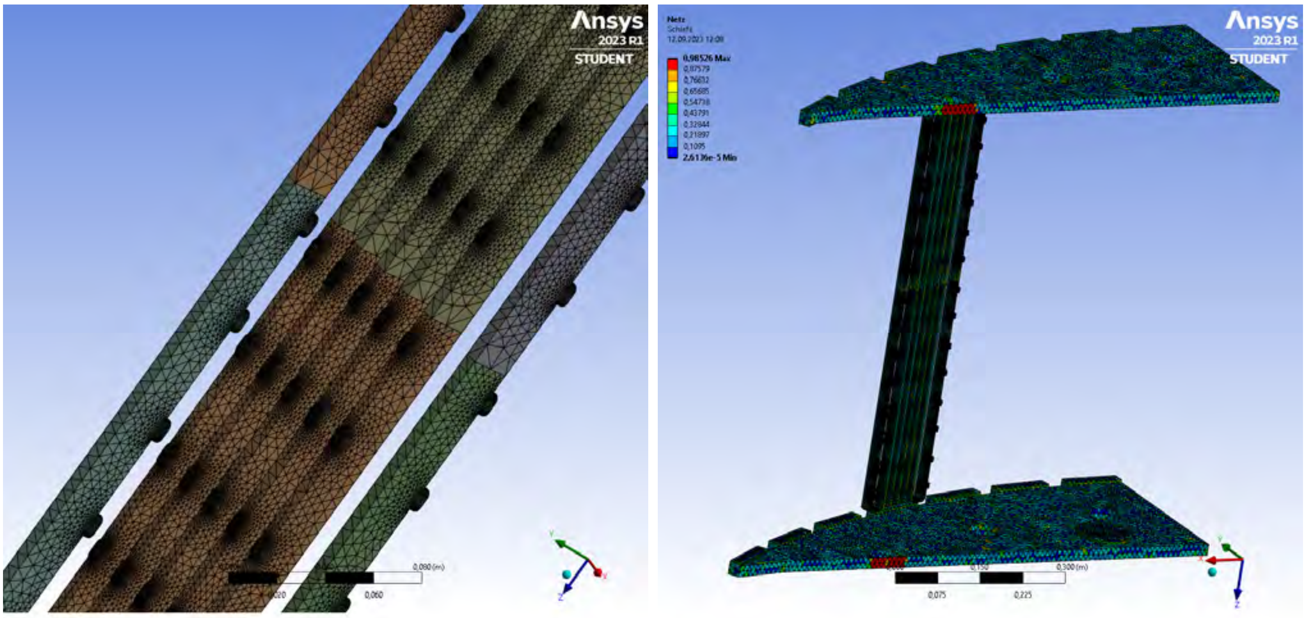

(a) Meshed volume extract of the BKPL cooling mask. The mesh becomes finer in regions where the cell gradient increases which is the case for the small slits of the cooling mask where the streamlines change their direction.

(b) Meshed volume extract of the full-size prototype with the fourth column. The skewness parameter is shown on the color scale. The value should not exceed 0.95 for tetrahedral cells which is the case here.

Figure 7.10: Meshing of the column geometry.

single backplane. Before examining the vertical air distribution along the column it is worth taking a look at the simulated turbulence parameters inside the system: the turbulent kinetic energy (TKE) and the turbulence intensity (TI). Both make up a not inconsiderable contribution to the air flow (cf. Fig. 7.11). Much turbulence (up to 70 % intensity) can be observed in the immediate vicinity of the inlet. Especially the inflow to the first two outlets is massively affected by this. Small air vortices can therefore be regarded as the reason of the abovementioned outlet hierarchy that deviates from expectation. The outflow through the outlets is affected by small turbulence effects as well. This transfers at least to a small extent to the outer backplanes. In general, turbulence modeling is delicate and requires fine meshes. They can have a large impact onto the slight deviations from the measurements. Due to the restricted number of cells given by the available Ansys license, a finer mesh that led the solution possibly converge down to 1e-6 was not possible.

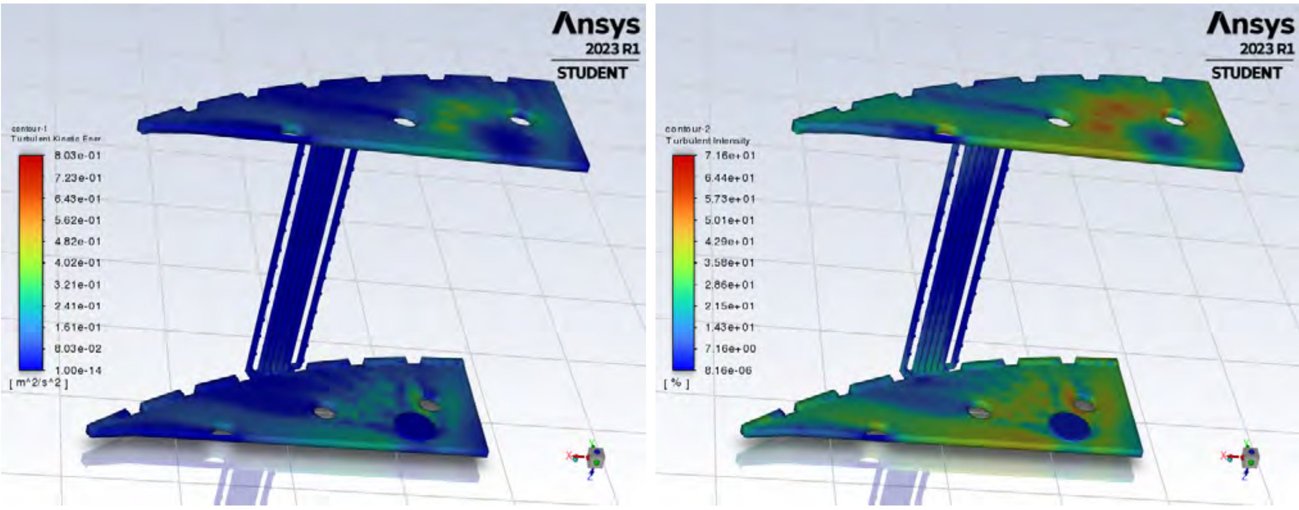

(a) TKE **(b)** TI

Figure 7.11: Turbulence parameters in the column simulation.

Slit Size Modeling

In this study two versions of backplane cooling masks will be compared. As a first scenario the slit sizes of the mask are all of equal size and shape. The total area of the slits on the backplane side is $\sim 40\,\mathrm{cm}^2$. The vertical air flow distribution is predicted to be inhomogeneous in such a way that the outer backplanes (1,2,6,7) will be supplied with more air compared to the middle backplanes (3–5). Hence, an obvious modification is to decrease the slit sizes of the outer backplanes and to increase them for the inner ones. The slit sizes have been adjusted such that they have 120 % respectively 80 % of the previous cross-sections. This does not agree with the calculations of the degrees of inhomogeneity at a high precision level, however it is a good starting point to prove whether it has the desired effect. It is important to mention that the total outlet area changes as well in this constellation, as there are four outer and three inner backplanes, thus the mask version with adapted slit sizes has an effective decrease 20% of total outlet area sum (~ 32 cm^2).

Results

First qualitative results of both scenarios are shown in Fig. 7.12. It shows the mass flow contour in kg/s at every slit at an inlet MAF of 50 kg/h (0.0138 kg/s). The color scale must again be interpreted in reverse: bluish colors correspond to high MAF in outwards direction through the slit while reddish colors mean low MAFs. Unexpectedly most of the air flow concentrates at the middle backplanes 3–5. However, the symmetry character of the setup can be observed. A deeper insight is gained by looking

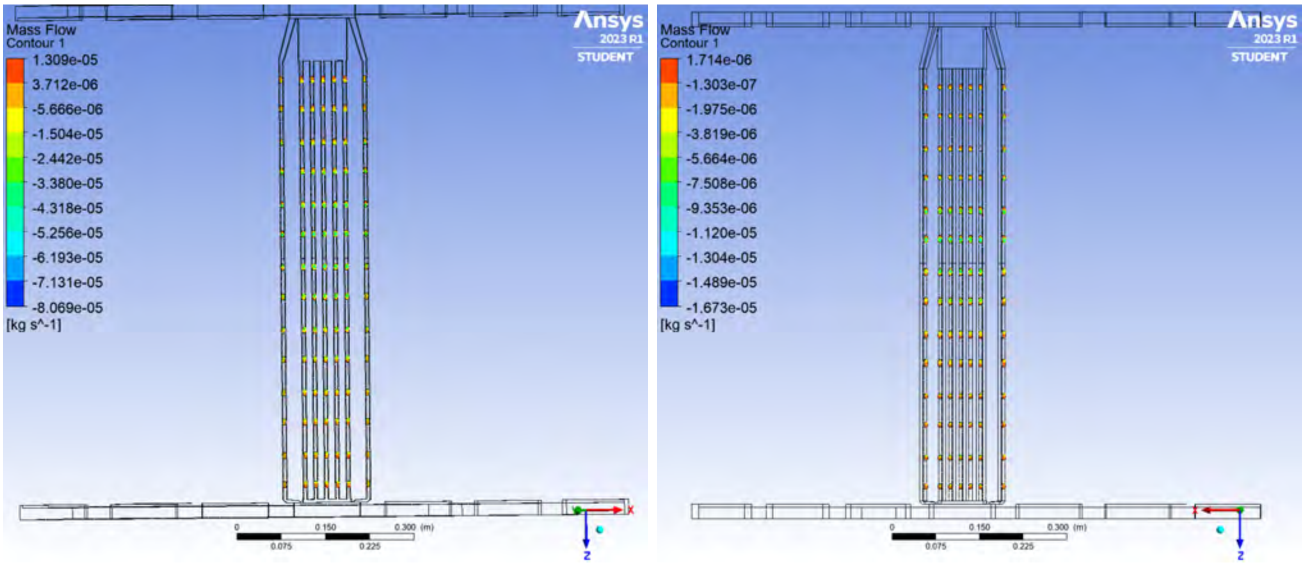

(a) Equal slit sizes.

(b) Adjusted slit sizes.

Figure 7.12: Simulated MAF contours of upper and lower part of the fourth column in the RICH camera prototype. The inlet MAF is 300 kg/h.

at the explicit vertical air distributions of the columns (cf. Fig. 7.13 & 7.14). For very small air flows (10 kg/h), the global trend of the air distribution with equal slit sizes is as expected: the air flow is highest at the outer backplanes and decreases towards the center. For increasing inlet MAFs, however, this behavior is reversed. Additionally, the air symmetry with regards to the backplanes vanishes, as BKPL3 becomes a more and more pronounced peak in air flow. This can be understood by taking a closer look at the cooling design. For design reasons, between the upper ADP and the cooling masks there is a small intermediate piece that guides the air which is not the case for the lower ADP. This changes the symmetry plane of the camera and shifts it slightly upwards in terms of the air flow.

Something that cannot be understood within the scope of the simulation work is the reversing effect of the vertical air flow distribution. However, the change in the total outlet area sum hints towards a change in backpressure. This can have an impact on the air flow inside the ADP and inside the cooling mask. Whether this could even have an effect on the homogenization of the system is discussed in the following chapter.

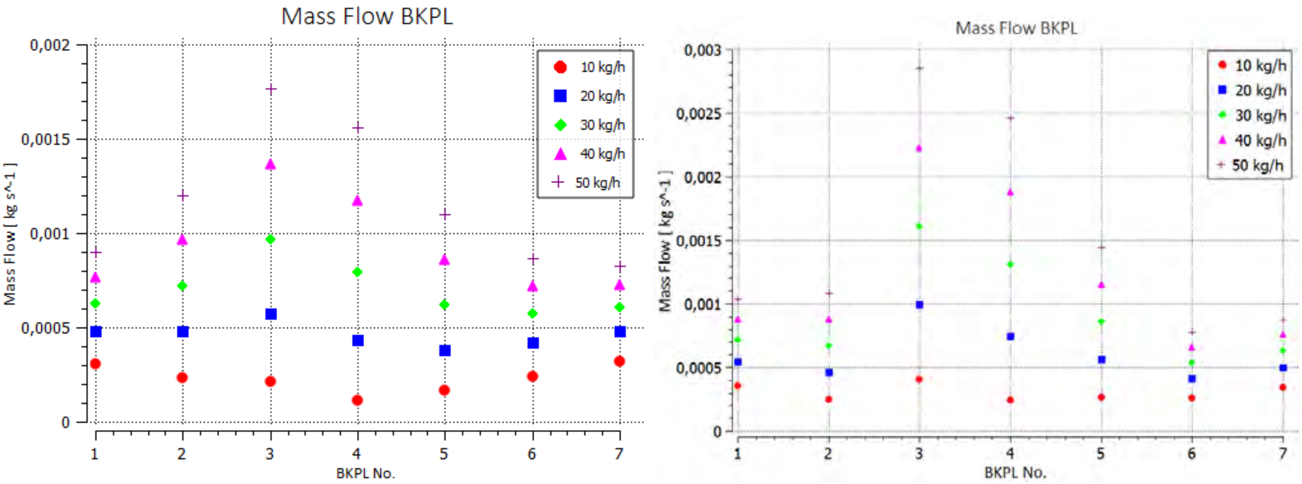

(a) Equal slit sizes. (b) Adjusted slit sizes.

Figure 7.13: Vertical column air distribution for inlet MAFs between 10 and 50 kg/h.

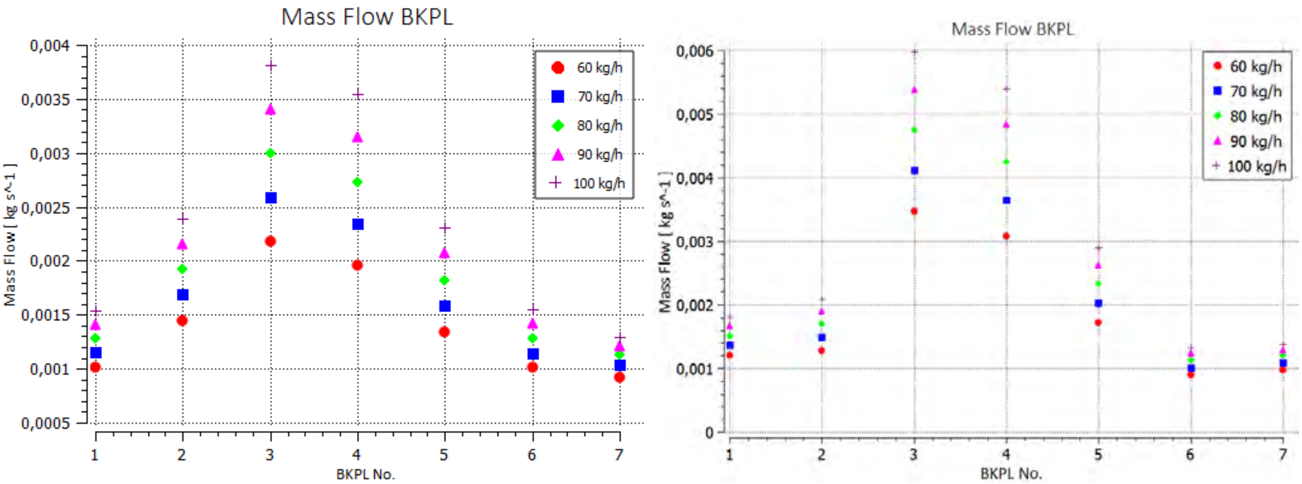

(a) Equal slit sizes. (b) Adjusted slit sizes.

Figure 7.14: Vertical column air distribution for inlet MAFs between 60 and 100 kg/h.

7.5 Backpressure

One additional requirement on the whole cooling setup and especially the ADP is that the backpressure induced by the system should not be too large. This is important since the side-channel blower can only produce sufficient air flow if the backpressure induced by the system is not too large. To measure the impact of the ADP a dedicated set of measurements and simulation has been carried out. The pressure inside the camera system should not exceed a critical value. On the other hand, more pressure inside the ADP leads to a homogenization of the air flow. Combining and balancing the two aspects is aimed in this chapter.

7.5.1 Air Distribution Plate

The first backpressure measurements were taken when the camera column was not equipped yet. In order to find some explanations for the small deviations between measured and simulated lateral air flow distribution the mismatch in backpressure inside the ADP has to be characterized.

Measured Backpressure

The pressure drop inside the camera system must not be too large. That this is guaranteed has been proven in several tests. The pressure is monitored at several locations within the heat exchanger. One of the pressure sensors is positioned at the output, where the air is guided through the inlet MAF and to the hose. The pressure drop can therefore estimated by taking time-averaged pressure data when the hose is attached to the camera and without. The difference between the measurement gives information about the backpressure that is created by the camera, assuming the total MAF remains constant (this was checked and is fulfilled). In a first step, the backpressure that is created merely by the ADP is investigated. At this time, the camera was neither equipped with backplane cooling masks nor with readout electronic modules. The result of this setup is shown in Fig. 7.15. There the pressure is plotted against time for both constellations, with and without the hose attached to the ADP and with the blower at full operation (inlet MAF = 300 kg/h). After a certain ramp-up time, the target inlet MAF and the pressure are stabilized. Time averaging can be applied as soon as the point in time has occurred. The pressure drop is estimated to be 2.492 mbar, which is in the safe range. More pressure inside the system, however, can have a positive effect in terms of air homogenization. For example, if the effective area of each outlet is reduced, the air flow will more and more evenly distribute among the individual outlets.

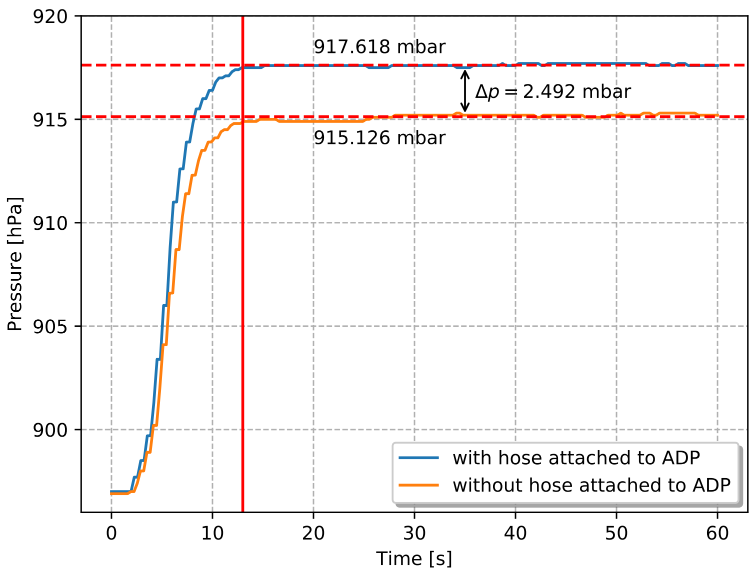

Figure 7.15: Pressure difference measured at the output of heat exchanger with hose and without hose attached to the ADP at 300 kg/h inlet MAF. In this case no cooling masks are installed.

Simulated Backpressure and Comparison to the Measurement

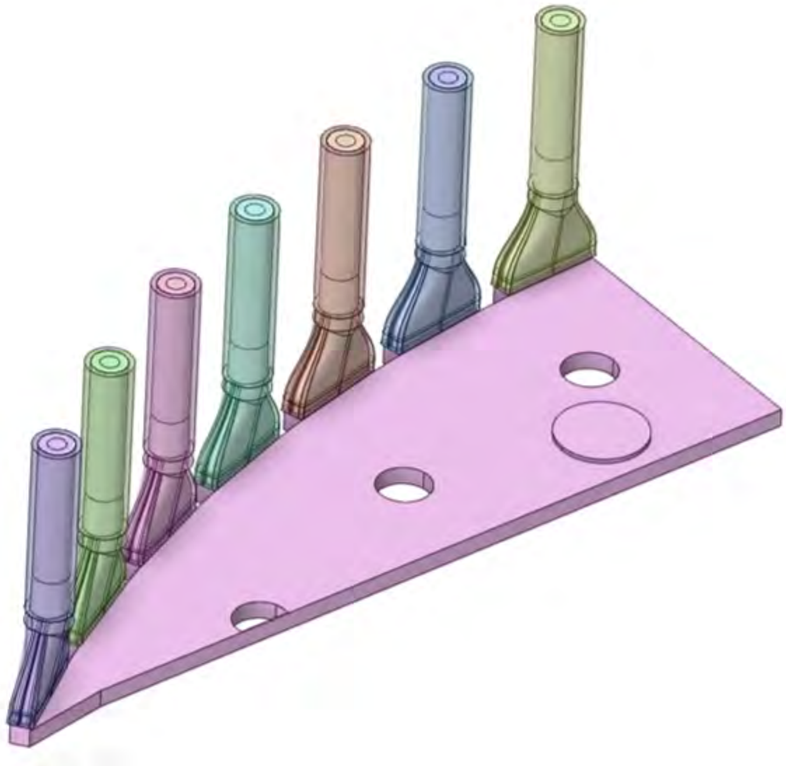

Figure 7.16: Volume extract of the ADP with adiabatic guide adapters placed on each outlet.

It can be assumed that the backpressure in the simulation is significantly smaller than in the measurement. One method of achieving this is to artificially reduce the size of the openings in the prolongation tubes. In the simulation, the pressure is calculated for each cell automatically through the Navier-Stokes equations. In the post-processing it is possible to get information about the maximum pressure and the mean volume backpressure inside the system. The latter is more suitable to compare with the measured backpressure. A function calculator can return the volume integral of the static pressure, total pressure, dynamic pressure and absolute pressure for a specified geometry volume. The backpressure corresponds to the pressure that is created when the fluid is at stillstand (static pressure). Hence this option was chosen for all further simulated backpressure values. The simulated backpressure depends strongly on the diameter of the outlet adapters connected to the ADP. Therefore, several measurements were made with varying outlet hole sizes. The opening hole size of the printed adapters is just above 38 mm. The size can be reduced in the geometry by creating a smaller circle at the top of the prolongation tube which is later defined as outlet boundary condition (cf. Fig. 7.16). The remaining area is set automatically to a wall boundary condition. A total of four simulations are performed with outlet sizes of 20, 25, 30 and 35 mm. These measurements together with the measured backpressure are depicted in Fig. 7.17a. The simulated mean volume pressure inside the ADP almost vanishes for the case with normal adapters, which is not realistic because this value underestimates the measured value (green). A further observation is that the measured backpressure is comparable with the simulated maximum pressure and the simulated mean volume backpressure at $\sim$ 25 mm opening size. In fact, the c-parameter, which is a measure for the agreement between measurement and simulation, improved for reduced opening hole sizes and reaches a minimum at roughly 25 mm (cf. Fig. 7.17b). One possible explanation on why the smaller hole sizes in simulation reproduce the measured results better is, that the surface roughness within the rough 3D-printed outlet tubes is not well reproduced in simulations. Hence, reducing the hole size might artificially result in more realistic simulations. The most important finding is that the backpressure in the simulation is not reproduced correctly. Unfortunately, the backpressure can be manipulated only in an artificial way by reducing the outlet opening sizes. In principle, it is possible to define a gauge pressure at the inlet and each outlet, meaning a relative pressure compared to the ambient pressure that is set in every simulation. However, it is for example not clear at which outlet how much backpressure would have to be generated.

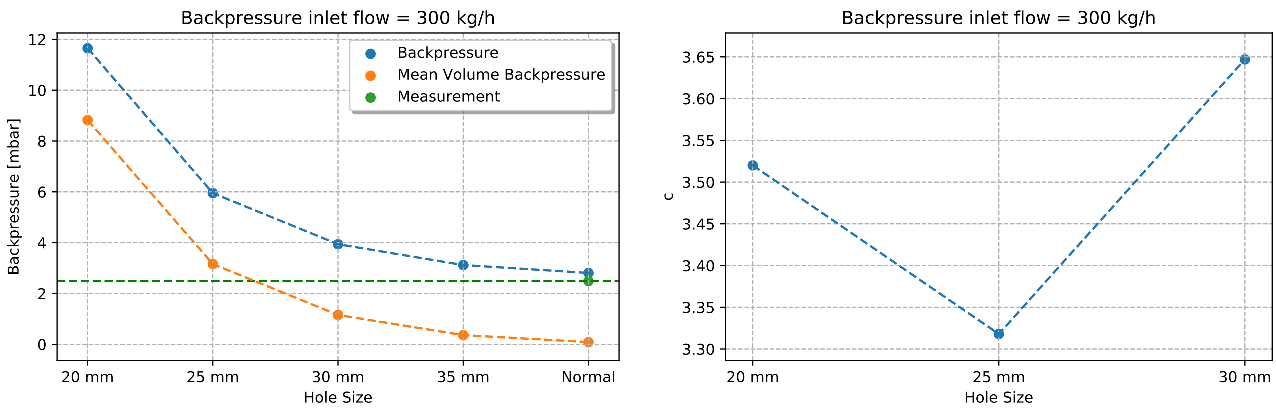

(a) Simulated (blue and orange) backpressure for different outlet hole sizes and measured backpressure (green dotted line).

(b) Calculated c-parameter for different outlet hole sizes. A hole size of 25 mm reproduces the pressure conditions in the system best.

Figure 7.17: Comparison of simulated and measured backpressure inside the camera prototype. The backpressure inside prototype system is investigated at different hole sizes of the adapter tubes and a fixed inlet flow of 300 kg/h.

Air Flow Homogenization due to Backpressure

The homogenization evolution with decreasing outlet sizes can be observed in Fig. 7.18a-d. In the limit of infinitesimal small outlet sizes, the air flow will achieve an exact homogeneous outlet air distribution. An outlet size of ~ 25 mm would provide a degree of inhomogeneity which is sufficient for the purposes of the cooling system. On this basis, a reduction factor for the effective area of the ADP outlets can be estimated by taking the ratio of the best simulated outlet area size and the inner diameter of the prolongation tube. Consequently, a reduction of $25/38.5 = 65\%$ of each ADP outlet could provide sufficient homogeneous air distribution inside the ADP. The rectangular area of each outlet is $112\,\text{mm} \times 21\,\text{mm} = 2352\,\text{mm}^2$. The effective area can be changed by the plastic sliders which reduce the depth dimension. Therefore, each slider can be set such that the outlet height is $0.65{\times}21$ mm $= 13.65$ mm. This can be reviewed, however, depending on the heat distribution across each column and possible hot spot generation, it must be adapted flexibly depending on the actual case. One might even envision slightly asymmetric sliders to cope with the left-right inhomogeneity of the air flow at each outlet.

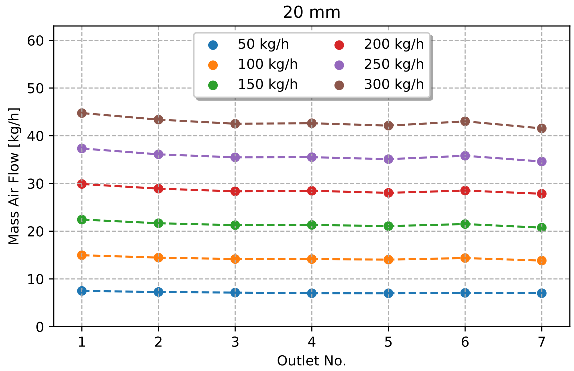

(a) Opening hole size: 20 mm

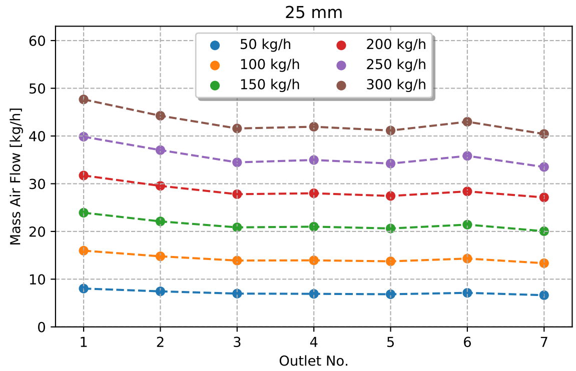

(b) Opening hole size: 25 mm

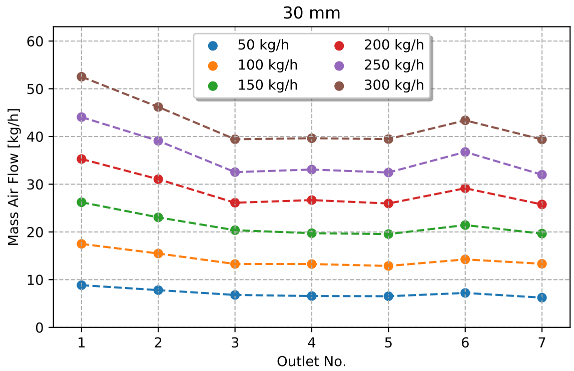

(c) Opening hole size: 30 mm

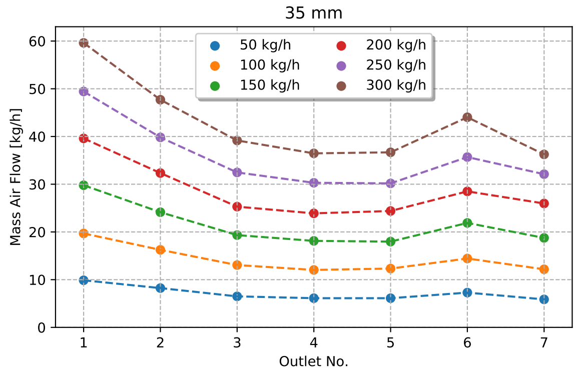

(d) Opening hole size: 35 mm

Figure 7.18: Outlet air distribution simulations for different opening hole sizes of the prolongation tube. A smaller opening size leads to more backpressure into the system with simultaneous homogenization of the air flow.

7.5.2 Single Camera Column

The incorrect prediction of backpressure in a simulation has an even more relevant effect when both ADPs and backplane cooling masks are included. This was seen in the air flow distribution along a single column as larger air flows were observed to occur in the middle backplanes compared to the outer ones, which normally has to be vice versa. Therefore, the backpressure measurement was repeated for the extended setup including the cooling mask and the readout electronic modules. The measured backpressures at different inlet MAFs are shown in Fig. 7.19a. This time the measurements were taken in a lower flow range from 10–70 kg/h since all the air is going through one outlet while the others are closed. The values of the other measurements range between roughly 0 and 5.5 mbar. The simulated backpressure values were once again extracted from Ansys post-processing tools. It turns out that especially for lower air flows the backpressure of the whole volume that is created on average in the simulation is underestimated by a factor of 100. This becomes very clear in the semi-logarithmic backpressure plot in Fig. 7.19b. Generally, it would be important to know how much backpressure is generated per column in order to transport the correct cooling capacity. For seven outlets the MAF rate must then be increased sevenfold as a first approximation, whereby the backpressure remains unchanged overall. A precise analysis of the heat dissipation generated in the camera will show that one should operate at 60 kg/h MAF rate per column (cf. Fig. 7.19 & Fig. 7.25). This will be discussed in the following chapter.

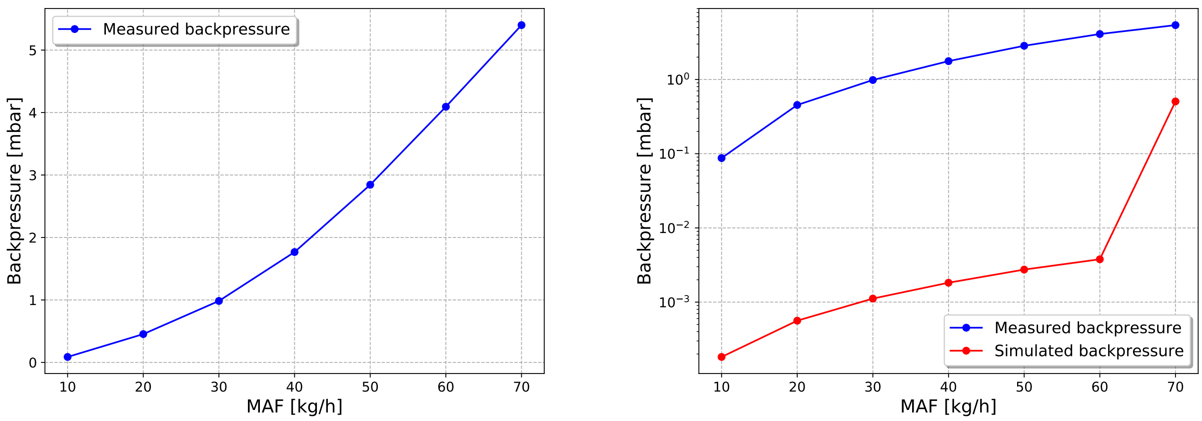

(a) Backpressure measurement with fully equipped column for different inlet MAFs

(b) Comparison of measured and simulated backpressure in a semi-logarithmic plot.

Figure 7.19: Backpressure measurement with both ADPs and a fully equipped column.

7.6 Heat Dissipation in a fully commissioned Camera Column

In order to evaluate the full cooling concept, the heat produced in a column (and the heat given off to the camera system) can be examined. This requires the commissioning of a full column. 84 DiRICH-FEBs were manually programmed. During the measurements, three of them failed such that they were removed and 81 DiRICH-FEBs were left. Each backplane was equipped with 12 DiRICH-FEBs, a power and a combiner module (cf. Fig. 7.20b). Each position in the backplane is assigned an own identification number (address). The scheme is as follows: backplane 1 hosts the DiRICH-FEBs 0xa101, 0xa102,...,0xa109, 0x10a, 0x10b, 0x10c. Backplane 2 hosts 0xa201, 0xa202,...,0xa209, 0x20a, 0x20b, 0x20c and so on up to backplane 7. The power modules are supplied with 36 V such that they provide the corresponding voltages to the individual components by means of their onboard DCDC converter (red and black cables) whereas the combiners are connected to the HUB ports of the TRB3 via fiber cables (light blue). Since only a single column could be operated for the measurement, one needs to mimic the effects of them by different means. Herefore two styrofoam panels were added left and right of column four to insulate them and leave no option to radiate heat to the sides where normally the other heated electronic modules would be situated (cf. Fig. 7.20b). All outlets except of the fourth are closed. For reasons of stability, further styrofoam plates are used to prevent the upper adapters from falling out of the ADP. The main purpose of the cooling is to counteract overheating of the MAPMT modules. Therefore, an MAPMT was mounted on each backplane (cf. Fig. 7.20a). The temperature of the MAPMTs was measured with an infrared camera. Since the glass is slightly reflective, each thermal image was taken a second time with plastic cap (cf. Fig. 7.20c–d). Every 30 seconds the temperature measured by all DiRICH-FEBs, the blower frequency, the air temperature, the inlet MAF and the elapsed time are stored in a csv-file for further analysis. The heat distribution is investigated for a total of three scenarios. Switching the cooling water on respectively off results in two different cooling air temperatures of ~ 10 °C and ~ 22 °C. These measurements allow to understand the cooling behavior at different air temperatures. As the temperature of the cooling water in the CBM cave – and thus the output air temperature – is warmer than at the test stand, it makes sense to approach this temperature from top and bottom to derive characteristics of the cooling behavior. Four blower frequencies of 20 Hz ($\sim$ 112 kg/h), 15 Hz ($\sim$ 84 kg/h), 10 Hz ($\sim$ 56 kg/h) and 5 Hz ($\sim$ 27 kg/h) are chosen. Since the camera is an object with high heat capacity, the heat is radiated also to surrounding devices. The process of reaching thermal equilibrium takes some time. For these reasons, data is recorded until this state is reached before the next frequency is set. This takes about an hour on average with cooling water and a little more without, such that a full measurement takes 4–5 hours. An additional digital thermometer was attached to the fourth backplane. Thermal equilibrium was assumed to have been reached when the temperature change of the fourth backplane did not exceed 0.1 °C within 10 minutes.

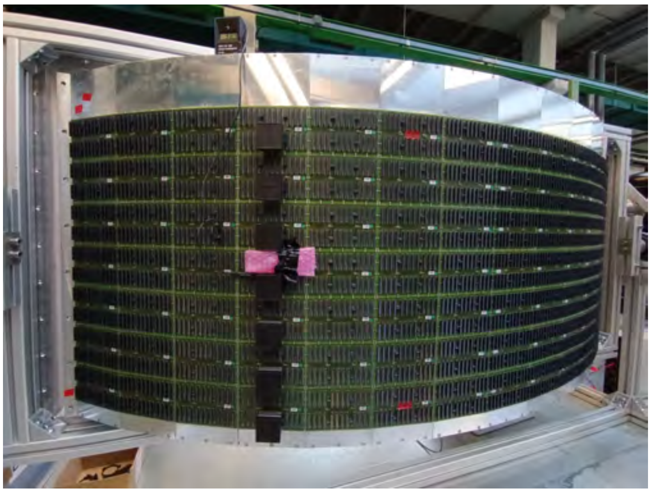

(a) Front view of the prototype: the fourth column is equipped with one MAPMT per each backplane. An additional digital temperature sensor is attached to BKPL4. It is used to monitor the temperature in order to determine the thermal equilibrium of the system.

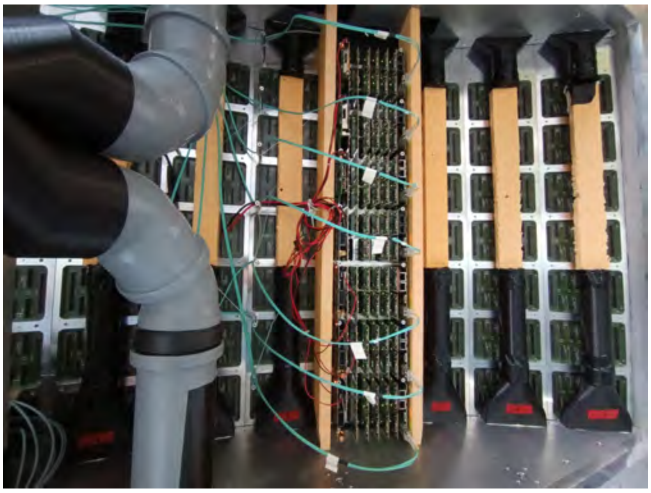

(b) Back view of the prototype: the fourth column is equipped with 12x7 = 84 DiRICH modules, 7 power modules and 7 combiners. The air of the inlet hose is split up with a custom adapter and is distributed through the top and bottom inlet.

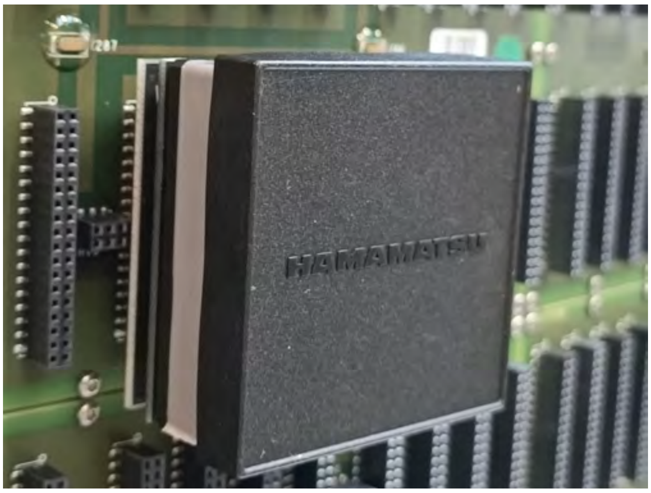

(c) Close-up of one MAPMT with plastic cap.

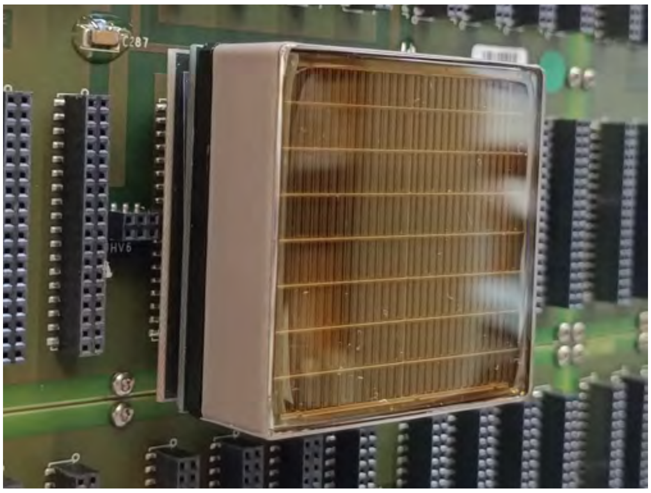

(d) Close-up of one MAPMT without plastic cap.

Figure 7.20: Experimental setup used for the temperature measurements.

7.6.1 Blower Off, Cooling Water Off

Before the air cooling system is investigated the heat dissipation can be examined. For safety reasons, an additional temperature switch is installed with the sensor being placed just below the upper ADP. The power supply is cut off if the air temperature exceeds the value of 45 °C. This measure prevents the system and especially the MAPMTs from overheating. The range of DiRICH temperatures and the induced average backplane temperature are shown in Fig. 7.21. It took roughly 25 minutes for the control temperature to reach the limit. With the passage of time, the spread in DiRICH temperatures becomes larger. At the moment of the system shutdown the hottest DiRICH temperature was around 60 °C and the coldest one at 40 °C, whereas most of the average backplane temperatures surpass 50 °C, with backplane 7 as an exception. A heat map showing the DiRICH temperatures and right position in

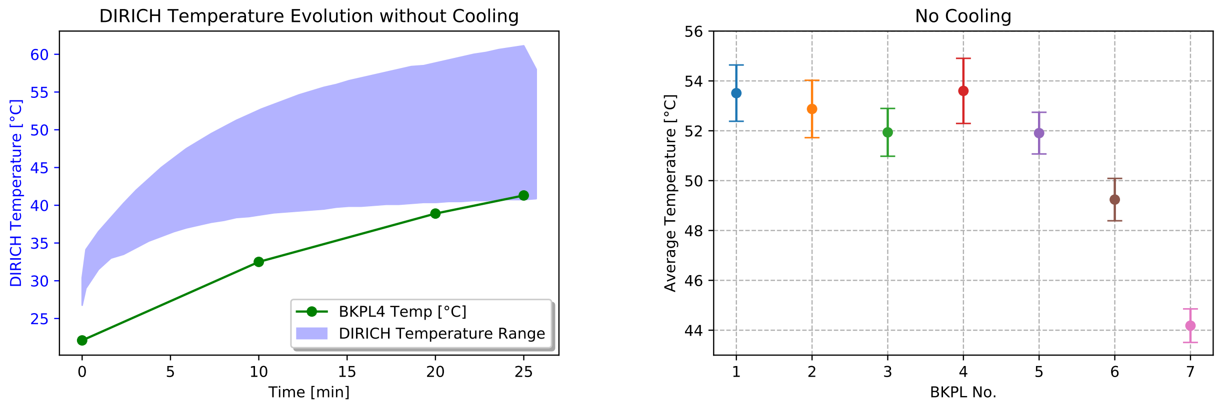

(a) DiRICH temperature evolution without active cooling measured over a total time of 30 minutes. The bluish band shows the temperature range of all DiRICHes, and the green dots are the temperature values read every 10 minutes at the digital thermometer attached to the BKPL4. The temperature spread is large: the coolest modules have a temperature of around 40 °C while some modules reach a temperature of 60 °C.

(b) Average backplane temperature. It is derived by taking the average of all DiRICH temperatures for the last measurement set when the thermal equilibrium is reached that are assigned to a backplane. The upper backplanes are warmer compared to the backplanes that are located at the bottom of the camera. This is consistent with warm air ascending from the bottom to the top in a convection process.

Figure 7.21: DiRICH temperature evolution without active cooling.

the column can be seen in Fig. 7.22 on the left. A temperature gradient from bottom to top is visible. This is to be expected with the warm air being produced rising to the top of the column, creating a chimney-effect. The leftmost and rightmost edges of the column are significantly warmer than the center regions, which is due to the fact that the combiner and power module which are both situated furthest outside produce more heat compared to the DiRICH-FEBs. The image on the right shows the DiRICH induced average backplane temperature which is calculated to be the mean over all DiRICH-FEB temperatures, but in a heat map. Here, the convection effect becomes more clear. However one can also recognize that the effect seems to saturate already at BKPL5 with the top five backplanes having nearly the same temperature. Nonetheless, the hottest backplane in the heat map is BKPL4 in the center and not the uppermost one. It is also conceivable that the power module in the center heats up slightly more than the other ones. Further, in BKPL4 the data of two DiRICH-FEBs is missing, more precisely from the lower row which is expected to be cooler than the upper row, which might artificially increase the calculated average backplane temperature slightly.

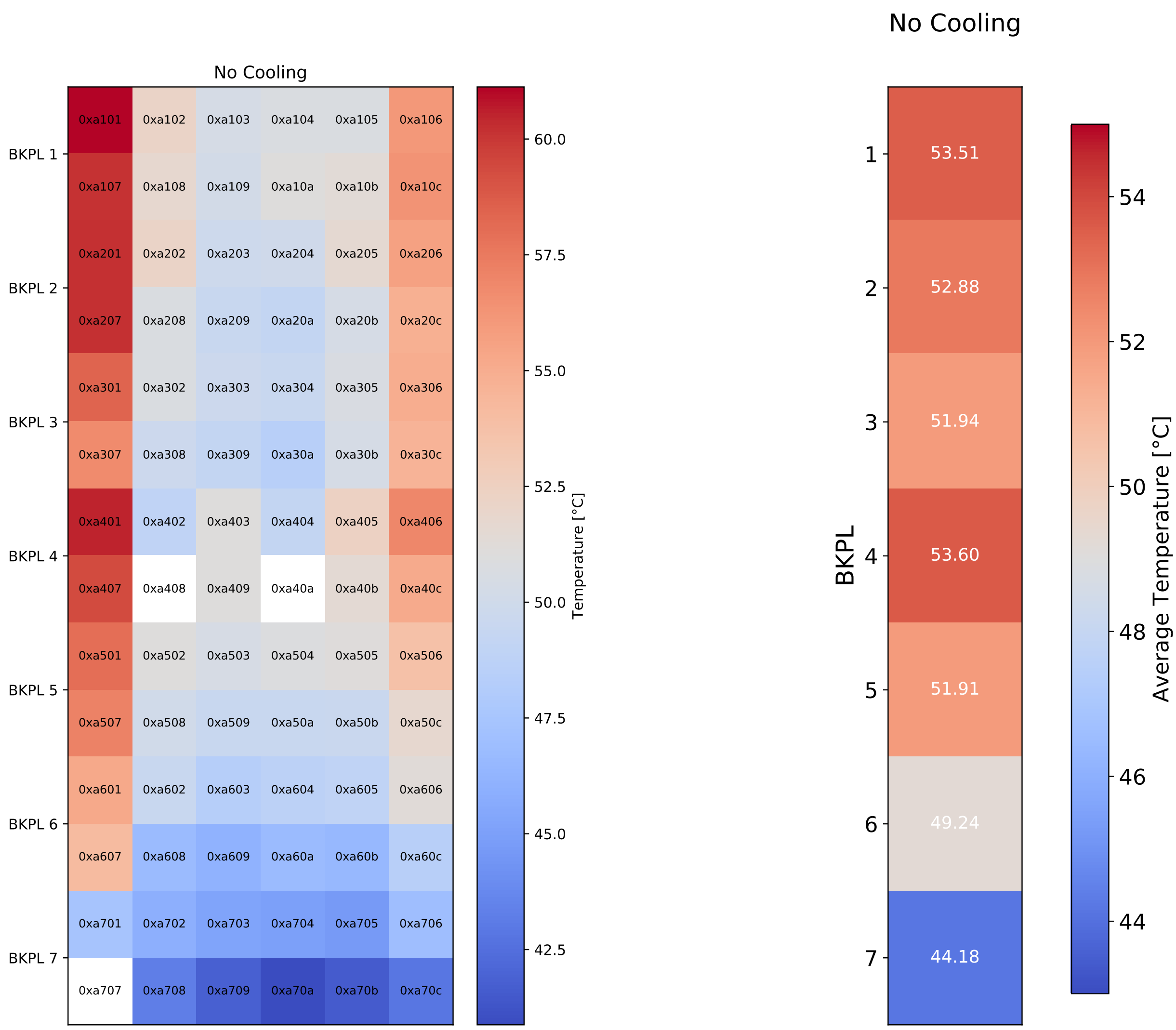

Figure 7.22: Heat maps of the front and back side of the prototype without active cooling.

7.6.2 Blower On, Cooling Water On

For the next measurement series the blower and the cooling water that is supplied to the blower are switched on. This measurement will serve somewhat as best case scenario since the water temperature and correlated air temperature are colder compared to the final setup in the CBM-RICH. Before the system can be fully put into operation, it is necessary to wait until the cooling water has completely cooled down the heat exchanger. By looking at the test stand GUI, one can observe the temperatures inside the heat exchanger, especially the air temperature at its output, and wait until it is saturated. The temperature evolution for different blower frequencies is visualized in Fig. 7.23 by means of thermal images of the whole PMT-side of the camera. From the images with fixed color scale the statement can be made that a significant decrease in cooling power is happening for >10 Hz. A not inconsiderable part of the heat is transferred to at least two neighbouring columns. It was always tried to keep the measuring point reproducibly on the same spot in the middle of the PMT-side of the camera prototype. The temperature increased from ≈ 23.5 °C to ≈ 28.6 °C for cooling power between 112 kg/h and 27 kg/h. The heat generated at the backplane is not evenly distributed whereas it is the case for the MAPMTs

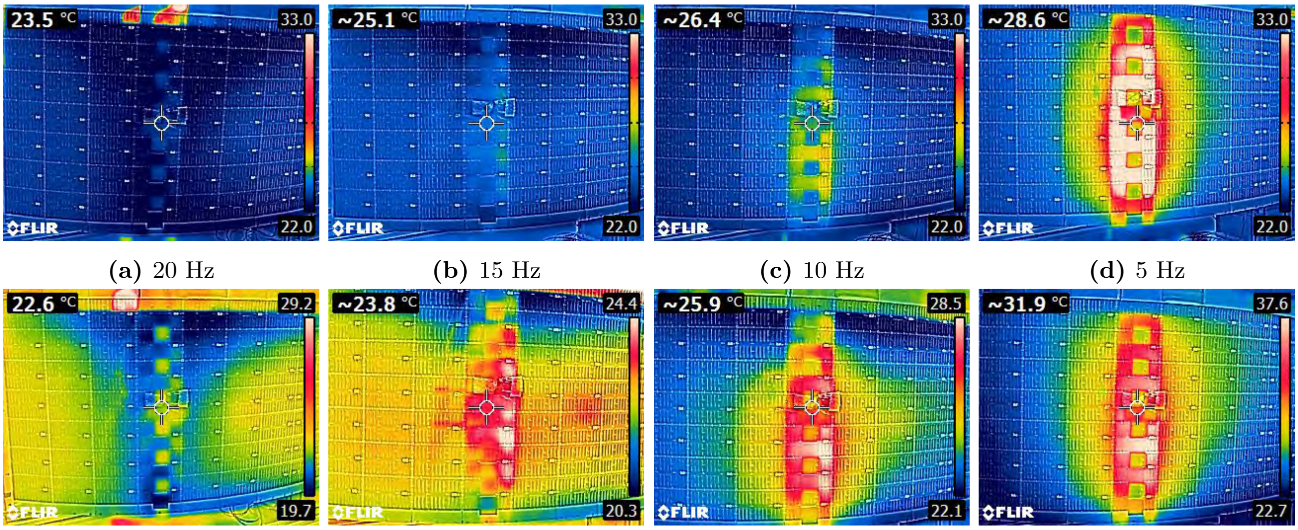

(a) 20 Hz **(b)** 15 Hz **(c)** 10 Hz **(d)** 5 Hz

(e) 20 Hz **(f)** 15 Hz **(g)** 10 Hz **(h)** 5 Hz

Figure 7.23: Thermal images of the back of the RICH camera prototype taken with an infrared camera for 4 different fan frequencies. (a)-(d) illustrates the temperature at a fixed scale, (e)-(h) for a variable scale.

(cf. Fig. 7.24a). This facilitates to describe the temperature behavior of the MAPMTs and justifies to just use the thermal image as a realistic quantification. A large part of the heat is dissipated by the power modules. At lowest blower frequency, it can reach temperatures of up to 80–90 °C. They are followed by the combiners and eventually by the DiRICH-FEBs. A thermal image of the camera electronics side is shown in Fig. 7.24b. It is noteworthy that the air directed to the upper inlet was often slightly colder (1–2 °C) than to the lower inlet. This artefact is clearly visible in the thermal image. This effect occurred every time when the input hose (that connects the camera to the heat exchanger and provides the blower air) was kinked, meaning that it was not in line with the splitter and is a possible explanation for more air flowing through the upper pipe and inlet compared to the bottom one. The evolution of the DiRICH temperatures with time is illustrated in Fig. 7.25a. The slightly fluctuating inlet MAFs are

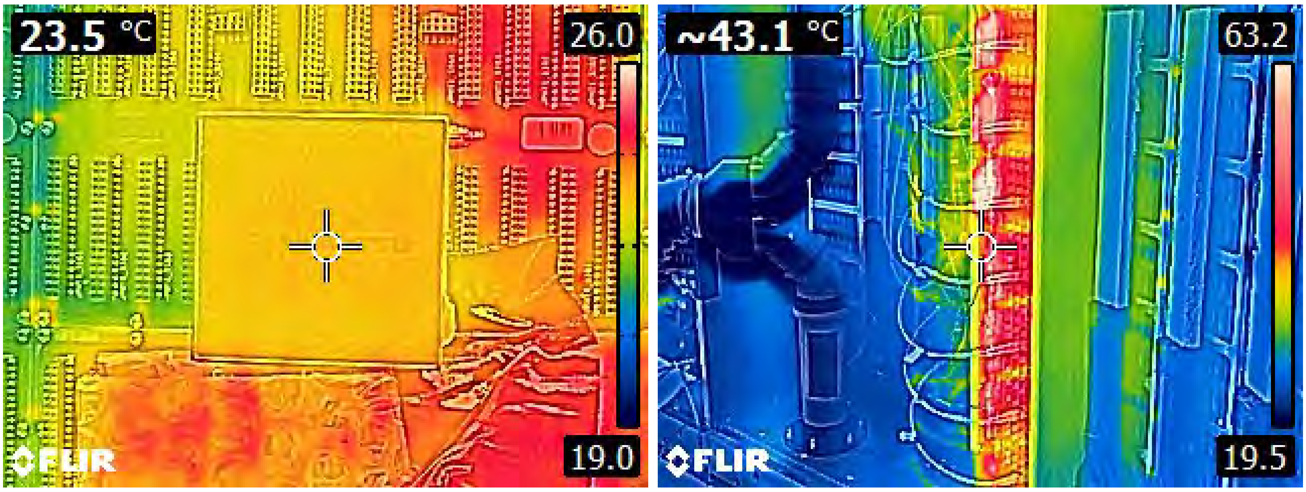

(a) MAPMT placed on BKPL3. In this image the plastic cap covers the photocathode. The temperature distribution is very homogeneous.

(b) Side view of the prototype front: the hottest components are the power modules, followed by the combiners and finally the DiRICH modules.

Figure 7.24: Thermal images of the experimental setup at a blower frequency of 20 Hz.

visualized in yellow and their mean value in dark blue. The corresponding blower frequency is shown in red. The temperature monitor on backplane 4 is represented by green dots. The figure clearly shows that with decreasing MAF (i.e. decreasing the blower frequency) the average as well as the spread of the temperatures of the DiRICH-FEBs increases. This is in line with an increase in the temperature measured by the digital thermometer on BKPL4. All 81 DiRICH temperatures are represented within the blue-shaded temperature band.

A first observation is that the spread in DiRICH temperatures is quite large (about 10 °C at $f = 20\,\text{Hz}$ and MAF = 112 kg/h) and keeps increasing the less cooling air is provided (about 20 °C at $f = 15\,\text{Hz}$ and MAF = 84 kg/h). Secondly, the DiRICH temperatures experience a disproportionate increase for the transition between 10 Hz and 5 Hz. The temperature of BKPL4 is always in the order of the coolest DiRICH, except for the last frequency setting. It can therefore be argued that the heat transfer from the electronics to the backplanes is not excessive. How much heat is generated by the electronics of each backplane can be quantified if one takes the average of all 12 DiRICH temperatures that belong to a backplane (cf. Fig. 7.25b). The absolute spread of the temperature averages for each backplane tends to be greater for low frequencies.

On a heat map with fixed color scale, the disproportionate increase of temperature between the last to frequency settings is more visible (cf. Fig. 7.26). It shows the average DiRICH-FEB temperature at the different backplane positions for the different blower frequencies and respective MAFs. The middle backplane 4 is the hottest for all frequency settings. Conversely, the outer backplanes are always the coldest ones. Generally speaking, the lower backplanes (5,6,7) are slightly warmer, which contradicts convection effects of upwelling warm air. One possible reason could be that the version of the power modules differ between upper and lower backplanes and probably heat up in different amounts. However, if the blower is operating then convection should not play a major role. Much more likely is the small asymmetry of the structure. For design reasons, there is a small black intermediate piece between the upper ADP and the cooling mask. It shifts the center of gravity of the backplanes slightly upwards.

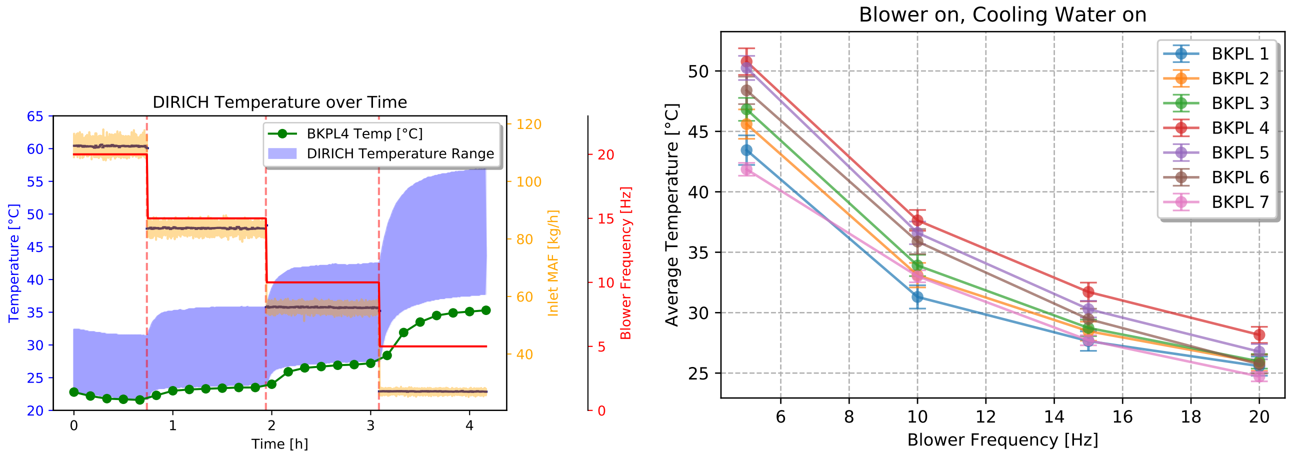

(a) DiRICH temperature evolution with active cooling water measured at different blower frequencies over a total time of four hours. The blue band shows the temperature range of all 81 functional DiRICHes. The blower frequencies are shown in red and the corresponding inlet MAFs in yellow. The backplane temperature monitor is visualized in green and lies always below the band.

(b) Average backplane temperature. It is built by taking the average of all DiRICH temperatures for the last measurement set when the thermal equilibrium is reached. The middle backplanes tend to be the warmest ones while the outer backplanes seem to be cooled more efficiently. The non-linear behavior of heat dissipation is visible in the plot.

Figure 7.25: DiRICH temperature evolution with cooling water.

Heat maps showing the temperatures of all DiRICH-FEBs for all frequency settings are shown in Fig. B.6 and B.7. They are highest at the far left and the far right edges of the column, for reasons that were discussed above. However, a strengthening effect can be the asymmetric air outflow through the outlet. Since no prolongation tubes are used in terms of creating a fully developed flow, more air is likely to be distributed through the left part of the column compared to the right part. A last observation is that the lower rows of each backplane tend to be cooled better as compared to the upper rows. This will lead to temperature gradients that can reinforce local convection effects. Since this behavior cannot be observed in the scenario without active cooling, this effect must be clearly assigned to the cooling concept. DiRICH heat maps with fixed color scales that illustrate the temperature evolution over time can be found in the appendix (cf. Fig. B.10 & B.11)

Since one of the main goals of the cooling scheme is also to protect the MAPMT from excessive heat which would result in an increased noise rate the temperature of the MAPMTs is also monitored throughout the measurement. Taking thermal images of each MAPMT at every blower setting one can assess the heat which is transferred from the backplane to the MAPMT. The images are traceable in the appendix and each measured value was written down in a table. The MAPMT temperature distribution depending on blower frequency and backplane number is shown in Fig. 7.28. Generally, the images that were recorded with cover do not differ significantly from the images without the cover. The global trend is consistent with the backplane average temperatures: MAPMTs that are located more towards the center are warmer than the MAPMTs that are attached to the outer backplane. However, the temperature spread is small and some outliers can be observed. They can be attributed to the measuring method where minor inaccuracies and systematic errors cannot be excluded. In general, the MAPMT temperature is reasonable for all frequency settings as they remain under 30 °C.

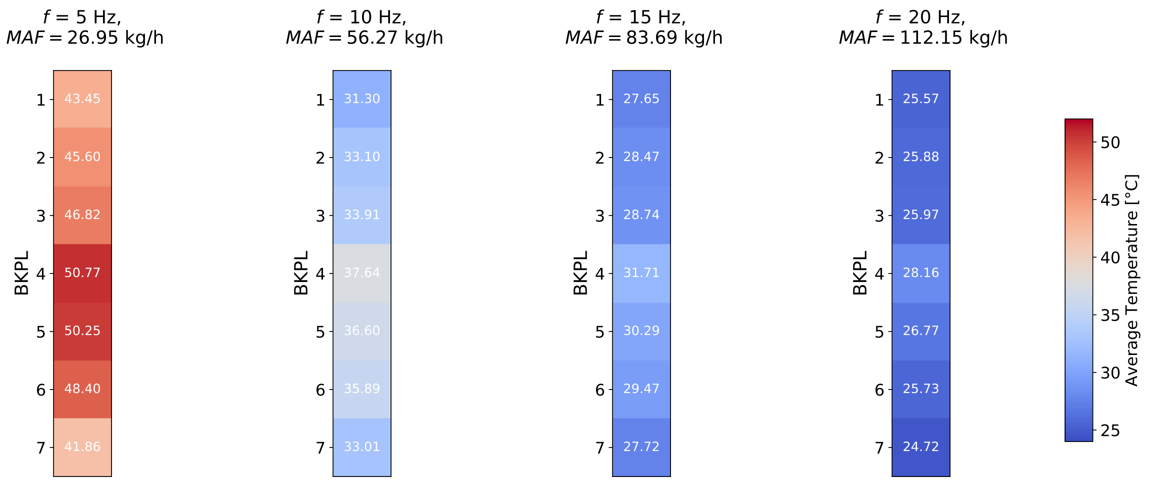

Figure 7.26: Backplane average temperature heat map at different blower frequencies, fixed color scale.

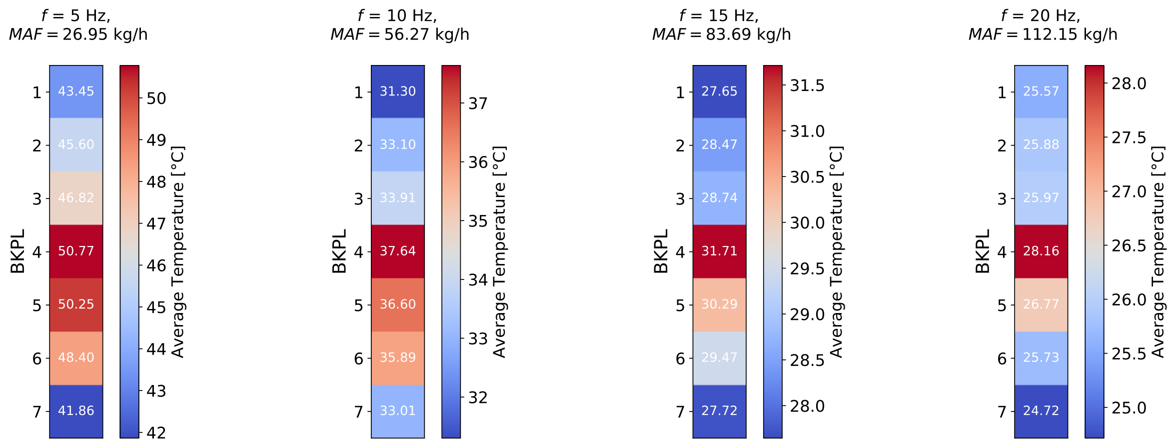

Figure 7.27: Average DiRICH-FEB temperature for each backplane presented as a heat map at different blower frequencies, variable color scale.

7.6.3 Blower On, Cooling Water Off

In order to get a feeling on what impact a lower air temperature has on the overall cooling performance the cooling water used for the blower is being switched off. If the cooling water is not in use, the cooling air temperature increases significantly. Additionally, heat that is generated by the side-channel blower can be transferred to the heat exchanger and this can take some time. Hence, it has to be ensured, that the air temperature stabilizes before a measurement is started. Over the course of the whole measurement, the cooling air temperature was nearly constant and increased by only 2 °C, which is acceptable. The stabilization was completed after the second set of measurements (transition between 15 Hz and 10 Hz, cf. Fig. B.5b). Without cooling water the measuring spot of the thermal image for the lowest blower frequency shows a temperature of 31.5 °C on the PMT-side, which is roughly 3 °C warmer than for the same scenario but with cooling water (cf. Fig. B.17). The difference in MAPMT temperatures is even smaller (cf. Fig. B.15) but the overall behavior is similar: the lower backplanes exhibit slightly higher temperatures than the higher ones. This could be due to the fact that a symmetric inflow into the ADP

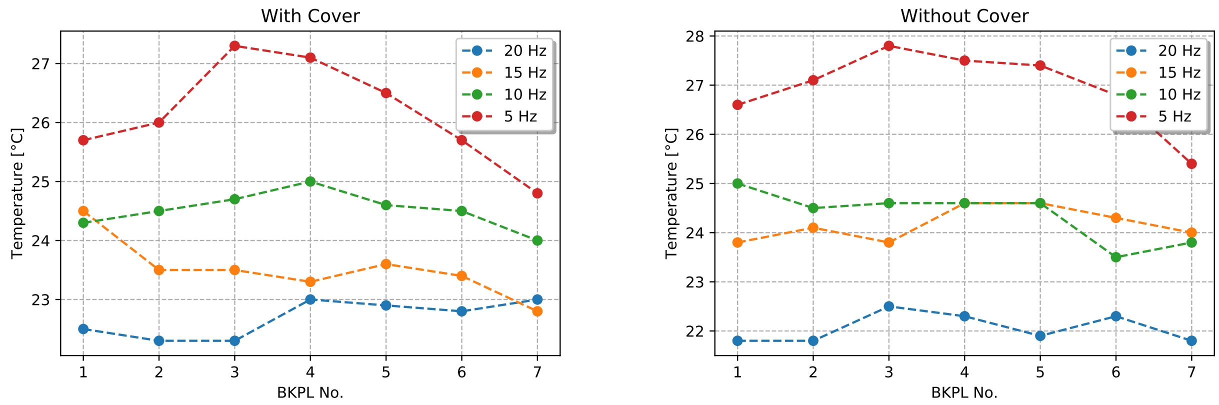

(a) With cover. **(b)** Without cover.

Figure 7.28: MAPMT temperatures at each backplane for different blower frequencies, with active cooling water.

cannot always be guaranteed in terms of air temperature, meaning that it was observed that the air streaming towards the top ADP was slightly colder compared to the air streaming towards the bottom plate. However, it could also be related to effects of the cooling design, e.g. the intermediate piece which could homogenize the air before it is guided to the cooling masks. Both these effects could not be disentangled within the scope of this thesis. The DiRICH temperature evolution (cf. Fig. 7.29) shows pretty much the same behavior as the scenario with cooling water. Notably, by scrutinizing the BKPL4 temperature, it is noticeable that for decreasing MAF the heat is not transported to the backplanes as sufficient as for high MAF, since the distance between the bluish band showing the DiRICH temperature range and the green dots increase for lower MAFs. This effect stood already out for the scenario without cooling water, but is strengthened here. It can be explained by the waste heat being dissipated to the rest of the camera more efficiently. The lower rows of the backplanes exhibit still lower temperatures than the upper rows and the power module represents the largest external heat source for the DiRICH-FEBs. For the lowest frequency setting the DiRICH-FEBs they can get up to 60 °C hot while for f = 20 Hz and MAF = 112 kg/h it is merely up to 37 °C (cf. Fig. B.8 & B.9).

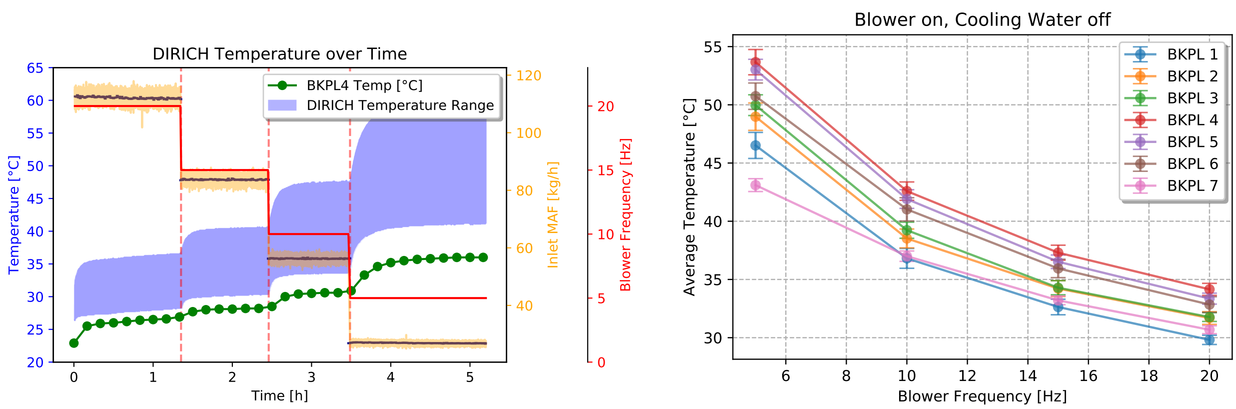

(a) DiRICH temperature evolution without active cooling water measured at different blower frequencies over a total time of five hours.

(b) Average backplane temperature. The middle backplanes are still the warmest ones while the outer backplanes are cooled more efficiently.

Figure 7.29: DiRICH temperature evolution without cooling water.

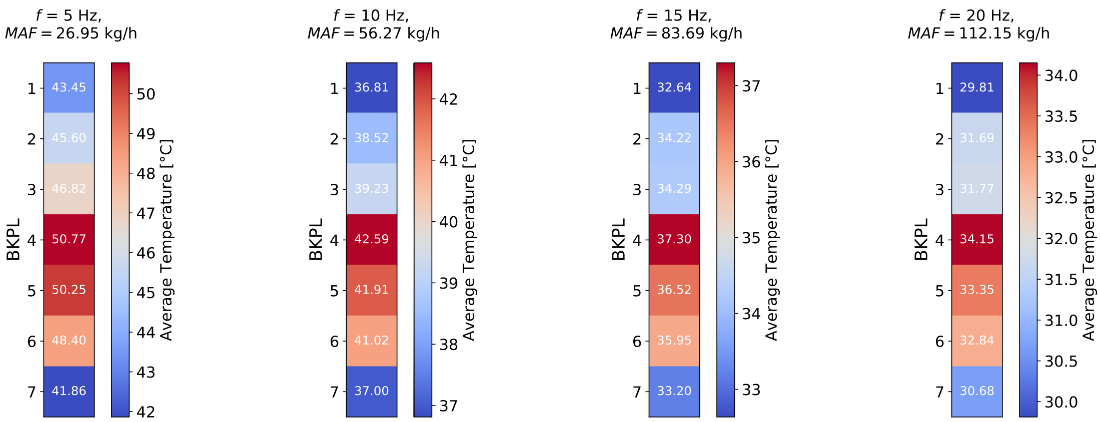

Figure 7.30: Average DiRICH-FEB temperature per backplane presented in a heat map at different blower frequencies, variable color scale.

7.7 Discussion of the Results

One of the most important findings in the CFD simulations is the underestimation of backpressure in the camera. The discrepancy between simulations and measurements is fortunately small in a setup that considers only a single ADP. This is why the simulated and measured lateral air distribution of the ADP outlets are in fairly well agreement, which is reflected by the small consistency parameter c. This is not the case for a fully equipped camera column that is distributed with cooling air by two ADPs from top and bottom side. The vertical air distribution along the column does not match the expectations, as in the simulation the inner backplanes are distributed with more air compared to the outer backplanes, which should be vice versa in reality. Obviously, in the simulation the vertical air distribution depends strongly from the amount of air flow and on the backpressure. The simulation systematically underestimates the real backpressure inside the camera and this was confirmed by a series of test measurements. At small air flows the effect is not visible as the air is guided preferably through the outer cooling masks compared to the inner ones. However, the effects due to the lack of backpressure become more and more dominant with increasing inlet MAFs as the air is pushed more through the slits inner cooling masks. Bernoulli's law states that if the fluid velocity increases, the dynamic pressure decreases as the total pressure remains constant in order to fulfill the pressure conservation:

$$p_{tot} = P + \frac{1}{2}\rho v^2 = \text{const.}, \tag{7.3}$$

where P is the static pressure and the second term is the dynamic pressure. This can lead, for example, to buoyancy forces. As the total air flow increases in the camera, the fluid velocity will increase particularly in vicinity of the outer backplanes (cf. Fig. 7.31a), which causes the dynamic pressure to drop such that less air comes out through the slits of the corresponding cooling masks. Also, the outflow inhomogeneity in a single slit becomes larger (cf. Fig. 7.31b), meaning that the mass flow rate tends to be always higher towards the center. Hence, a large share of the air streaming to the lower and upper outlet 4 is guided towards the center, the upstream and downstream air masses collide and are pushed out. Possible reasons for the mis-modeling of the backpressure can be oversimplified assumptions in the simulation setup that are made. The surface roughness of the ADP and the cooling masks is not modeled explicitly. The rougher a surface is, the more backpressure is generated. Moreover, it can create additional turbulence effects. In regions with high fluid velocity at the outer backplanes additional air vortices might be produced close to the outlet slits which prevents the air from flowing out unhindered. Further, the simulation setup neither includes the backplanes on the PMT-side nor the electronic modules on the other side which can exert additional pressure on the system. In the real measurements the

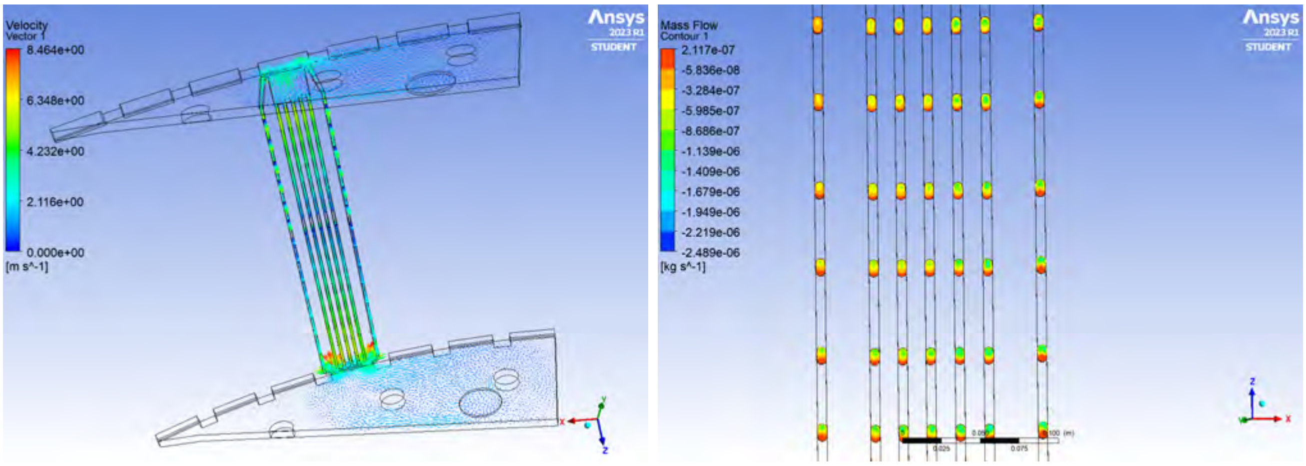

(a) Higher fluid velocities towards outer backplanes. **(b)** Higher outflow inhomogeneity towards outer backplanes.

Figure 7.31: Discussion of the simulation results for a vertical column airflow distribution.

dynamic pressure seems to play a minor role compared to the backpressure. Consequently, the observed vertical air flow distribution is slightly more homogeneous, and more importantly, the air is pushed out through the outer cooling masks. This prediction coincides with the temperature distribution of the backplanes on the electronics and on the PMT-side. As a consequence, the design of the cooling mask can only hardly be assessed by comparing the CFD simulations with the actual heat distribution in a column. However, the measurements showed an asymmetry pronounced as a small heat excess towards the lower backplanes 5-7 compared to backplane 3. This artefact is expressed in disproportionate air flow reaching backplane 3 in the simulations as well, as they both take into consideration the small intermediate piece in the upper ADP. Hence, an implication for an optimized homogenization model of the backplane cooling masks would be to adjust the slit sizes of backplane 3 in particular. A decrease in slit size of the outer cooling masks and an increase for the inner ones did not reveal any improvements in terms of air flow homogenization. Based on these simulations, however, it remains questionable if predictions can be made about improving the design of the cooling mask, because it makes oversimplifying assumptions, as discussed above.

An original estimate was to provide each camera column with 27 kg/h corresponding to $\sim$ 4 kg/h per backplane (see chapter 4). This agrees with the observation of the heat dissipation measurements at the lowest blower frequency setting (f = 5 Hz, MAF = 27 kg/h) as it keeps the MAPMT temperature below 30 °C (cf. Fig. B.16d). In this scenario, the backplane temperatures can reach up to 55 °C. Since a fully commissioned camera with all 14 columns would heat up relatively more, an additional requirement could be to restrict the backplane temperature as well. An inlet MAF of 83 kg/h for a single column is a reasonable setting. Having the inlet MAF at 83 kg/h for one column, this would mean an air flow of 11.85 kg/h per backplane and extended to all columns for one camera half a total inlet MAF of 581 kg/h in this scenario. This implies the need of a blower system with roughly four times the capacity of the cooling prototype in order to cool the full camera to a satisfactory extent. The temperatures of the backplane electronics and of the MAPMT are now kept well below 30 °C (cf. Fig. 7.32a & b). The plot shows the MAPMT and average backplane temperature for the air temperatures that are produced in the two different scenarios with and without the cooling water being switched on. Equivalent plots for all the other frequency settings can be found in the appendix (cf. Fig. B.16).

The cooling water in the CBM cave is about 16–18 °C, thus a cooling air temperature of 18–20°C is to be expected. Since this is a non-linear effect and as there is no model available that describes the relationship between heat generation and air cooling temperature, the data points cannot be linearly extrapolated. However, it can be stated that the average backplane temperatures would be somewhere around 30–34 °C and the MAPMT temperatures around 24–25 °C for air temperatures that are comparable with the conditions in the CBM cave.

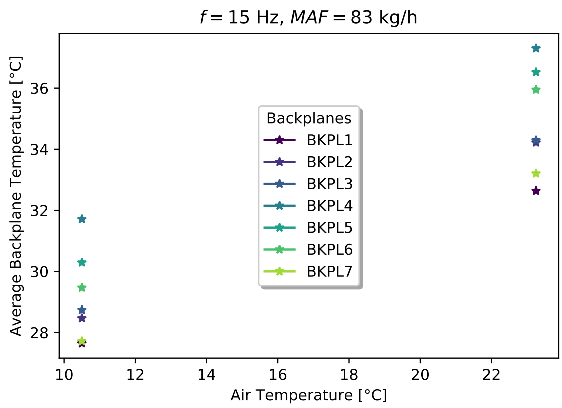

(a) Comparison of the backplane temperatures on the electronics-side at equal inlet MAF but different air temperatures. A realistic air temperature in the CBM cave is around 18–20 °C.

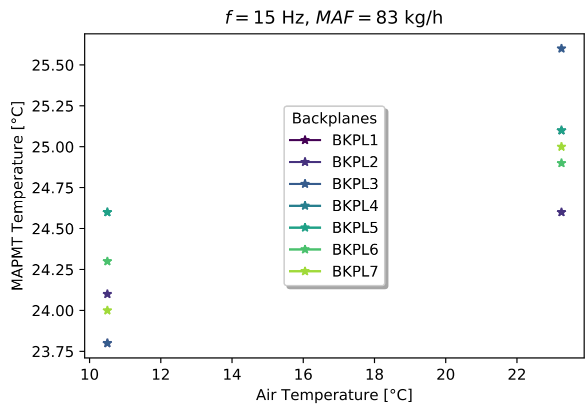

(b) Comparison of MAPMT temperatures at equal inlet MAF but different air temperatures. The spread in MAPMT temperatures is not as large as compared to the backplane temperatures.

Figure 7.32: Comparison of MAPMT temperatures at a MAF of 83 kg/h. Here $f = 15$ Hz, $T_{\text{air, with cooling water}} = 10.5$ °C and $T_{\text{air, no cooling water}} = 23.2$ °C

8
Summary and Outlook

This thesis addressed the issue of optimizing and commissioning a sophisticated air cooling system for the CBM-RICH detector at the future FAIR facility at GSI by means of a camera prototype. Special sensors that are capable to quantify the amount of air at various locations of the camera were tested with regard to their suitability and calibrated in dedicated measurements. The use of simple commercially available MAF sensors that are usually applied in motor vehicles turns out to be a viable solution as their pre-calibration curve can be exploited. Computational fluid dynamics simulations prove to be a powerful tool to predict the air flow for a given geometry at different scenarios. They help for a better understanding of the air flow in non-trivial environments. Further, CFD simulations can be exploited to develop concepts like that for the homogenization of the air flow inside the camera system. However, they turn out to be intractable in terms of the correct choice of flow type, mesh size, solver type and turbulence model. The significant characteristics of the air flow are in sufficient agreement, however not at an high accuracy level. A one-to-one transfer of the experimental setup into the simulation with highly accurate results would include the involvement of many other parameters (just to name a few: a thermodynamic model, a surface roughness estimation for the walls and a proper model of the pressure conditions, for example the consideration of backplane and readout electronics). Another important finding is that the camera prototype does not produce much backpressure and hence fulfills the requirement to stay well below 100 mbar. On the contrary, a small increase of pressure inside the ADP leads itself to an improvement of the outlet air flow homogeneity. This can be achieved for example by reducing the effective size of the ADP outlets by means of little plastic sliders. One camera column including seven backplanes that are equipped with the electronic components of the DiRICH readout chain could be successfully put into operation to get a first feeling on the heat production. Although the backplanes and the MAPMTs attached to them are heated differently, there is no longer a need for high levels of readjustment. The CFD simulations prove the uneven heat distribution and give rise to a modification of the backplane cooling mask. Intuitively one might argue that larger slits for the inner backplanes and smaller slits of the outer backplanes should improve the homogenization. However this turned out to be impossible to prove in the simulations due to significant underestimation of backpressure which leads to an excess of air flow for the middle backplanes and a deficit for the outer backplanes. One of the main questions of this work were to give a rough estimate on how much air should be provided for each column and each backplane, respectively. Hereby, a backplane temperature that does not exceed a critical value of 35 °C can be targeted, such that the MAPMT temperatures stay below 30 °C which is desirable. A blower frequency setting of 15 Hz producing an inlet mass air flow of 83 kg/h into a single readout column, respectively 12 kg/h per backplane turns out to satisfy this requirement. Further measurements with more camera columns are yet to come. With a fully equipped camera, for example, hotspots can be detected that give cause for additional excess heat to be pumped out in a close-cycle air cooling system.

A

More Calculations

Inlet Flow Modeling

The inlet flow modeling is essential when setting up the CFD simulation with a turbulence model. In the later procedure two-equation models will be tested as turbulence models, such that two input turbulence parameters are always required. These parameters are the turbulence intensity $I \equiv TI$ and the eddy viscosity ratio $\frac{\mu}{\mu_t}$. They are both connected to the turbulence kinetic energy (TKE) and depend on either the TKE dissipation rate ε for the k-ε model or on the specific dissipation rate ω for the k-ω model. For an example calculation, let us assume the following parameters: the inlet MAF $\dot{m} = 100$ kg/h, the pipe diameter $d = 75$ mm and the fluid is air at normal conditions: $\mu = 1.511 \cdot 10^{-5}$ kg/ms the dynamic viscosity and $\rho = 1.225$ kg/m^3 the air density. The k-ε turbulence model will be used. As already discussed above, the turbulence intensity TI is defined as (cf. Eq. 3.15):

$$TI = 0.16 \cdot Re_h^{-1/8}, \tag{A.1}$$

where the Reynolds number can be calculated through

$$Re_h = \frac{\rho \cdot \bar{u} \cdot d}{\eta} = \frac{\bar{u} \cdot d}{\nu} = \frac{4\dot{m}}{\pi \cdot d \cdot \eta} = 26053 > 2300 \tag{A.2}$$

Hence, the TI is:

$$TI = 0.0448 = 4.48\,\% \tag{A.3}$$

Once the TI is defined, the TKE can be derived:

$$k = \frac{3}{2}(\bar{u} \cdot TI)^2 = 0.0796\,\mathrm{m}^2/\mathrm{s}^2 \tag{A.4}$$

where the average velocity along the flow direction was calculated from the following relation:

$$\dot{m} = \rho \cdot A \cdot u \Longleftrightarrow u = \frac{\dot{m}}{\rho \cdot A} = \frac{4\dot{m}}{\rho \cdot \pi \cdot d^2} = 5.1327\,\mathrm{m/s}, \quad u \equiv \bar{u}. \tag{A.5}$$

With the TKE known, the dissipation rate ε can be obtained (cf. Eq. 3.18):

$$\varepsilon = C_\mu k^{3/2} l^{-1} = 0.3851\,\mathrm{m}^2/\mathrm{s}^3 \tag{A.6}$$

As a way of determining the eddy viscosity ratio, the dissipation rate can be utilized as they are related through the following equation:

$$\varepsilon = \rho C_\mu \frac{k^2}{\mu} (\frac{\mu_t}{\mu})^{-1}, \tag{A.7}$$

Finally, it is found that (cf. Eq. 3.16):

$$\frac{\mu_t}{\mu} = \mu_r = \frac{\rho C_\mu k^2}{\varepsilon \mu} = 100.1643 \tag{A.8}$$

Both turbulence parameters that were obtained are in well agreement with the empirical ranges for internal flows given in 3.2.3. The calculated eddy viscosity ratio suggests turbulence components of the flow that are not negligible. This approach is applicable in a very similar way for the k-ω model and for any mass air flows, but their calculations are not further elaborated here.

Calibration Setup

The pipes that connect the hose to the input MAF sensor, respectively the input MAF sensor to the three-way splitter has a diameter of 75 mm and a length of 1 m. In order to operate the BOSCH sensors in a most accurate way, the entrance length l_a should not exceed the pipe length l_p. To assure that, first look at the Reynolds number for an exemplary inlet MAF value of 100 kg/h as above, which prompts to use Eq. 3.20 for the entrance length. Thus, the pipe dimensions should be

$$10 \cdot 75\,\text{mm} = 0.75\,\text{m} < l_p < 4.5\,\text{m} < 60 \cdot 75\,\text{mm} \tag{A.9}$$

which is the case so it is to be expected that the MAF sensors work reliably.

Finite Volume Method

To give a rough idea about the procedure, a small mathematical sketch will be drawn. First start considering the conservation equation for a general scalar φ:

$$\frac{\partial(\rho\varphi)}{\partial t} + \nabla \cdot (\rho \vec{u} \varphi) = \nabla \cdot (\Gamma^\varphi \nabla \varphi) + Q^\varphi \tag{A.10}$$

where on the left side there is the transient and convective term and on the right side there is the diffusive and source term. For a steady-state problem, the transient term vanishes. If a control volume C is introduced the integrated equation looks like [19]:

$$\int_{V_C} dV\, \nabla(\rho \vec{u} \varphi) = \int_{V_C} dV\, \nabla \cdot (\Gamma^\varphi \nabla \varphi) + \int_{V_C} dV\, Q^\varphi. \tag{A.11}$$

As it is dealt with volume integrals now, the Gaussian divergence theorem can be applied such that volume integrals are replaced by surface integrals. There is a surface flux term and a volume source term left:

$$\int_{\partial V_C} d\vec{S}\, \nabla(\rho \vec{u} \varphi) = \int_{\partial V_C} d\vec{S}\, (\Gamma^\varphi \nabla \varphi) + \int_{V_C} dV\, Q^\varphi. \tag{A.12}$$

This is the so-called conservative form of the PDE which is solved by the FVM solver. The fluxes are integrated over the element faces. The total flux can be written as the sum of convective and diffusive flux:

$$\vec{J}^{\varphi} = \vec{J}^{\varphi,C} + \vec{J}^{\varphi,D} = \rho\vec{v}\varphi - \Gamma^{\varphi}\nabla\varphi. \tag{A.13}$$

The surface integral of the control volume can be approximated by the summation of the flux terms at each face.

$$\int_{\partial V_C} d\vec{S} \cdot \vec{J}^{\varphi} = \sum_{\text{faces}(V_C)} \left(\int_{\text{faces}} \vec{J}^{\varphi}_{\text{face}} \right) \tag{A.14}$$

Both, surface and volume fluxes can be solved by means of Gaussian quadrature.

B

More Figures

Preliminary Studies

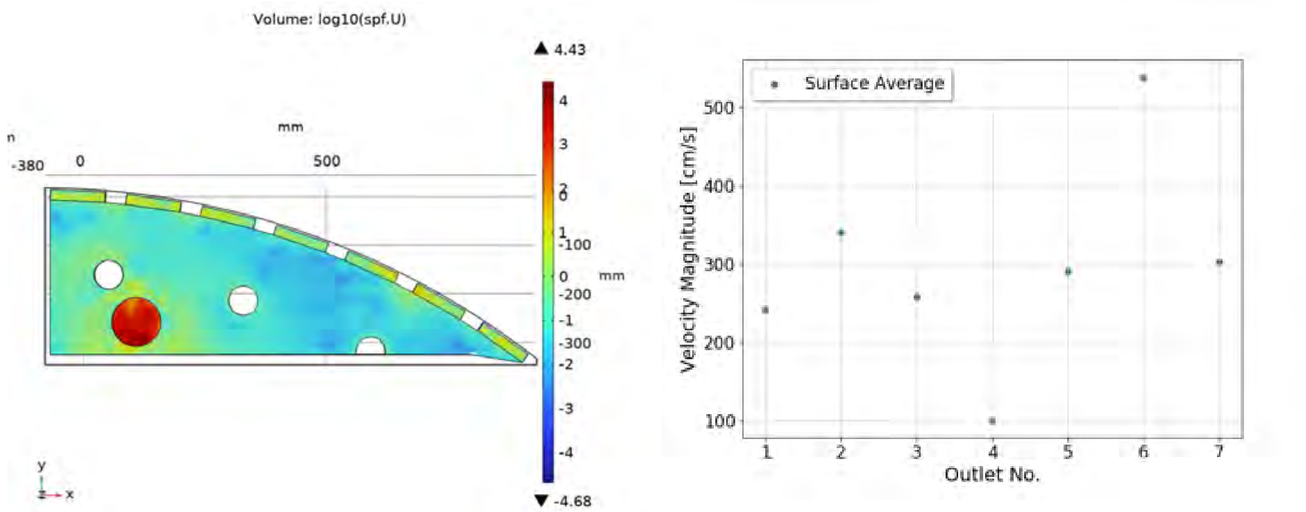

(a) Average surface velocity of the ADP.

(b) Outlet velocity magnitude distribution for an arbitrary inlet MAF.

Figure B.1: Preliminary results obtained with Comsol Multiphysics.

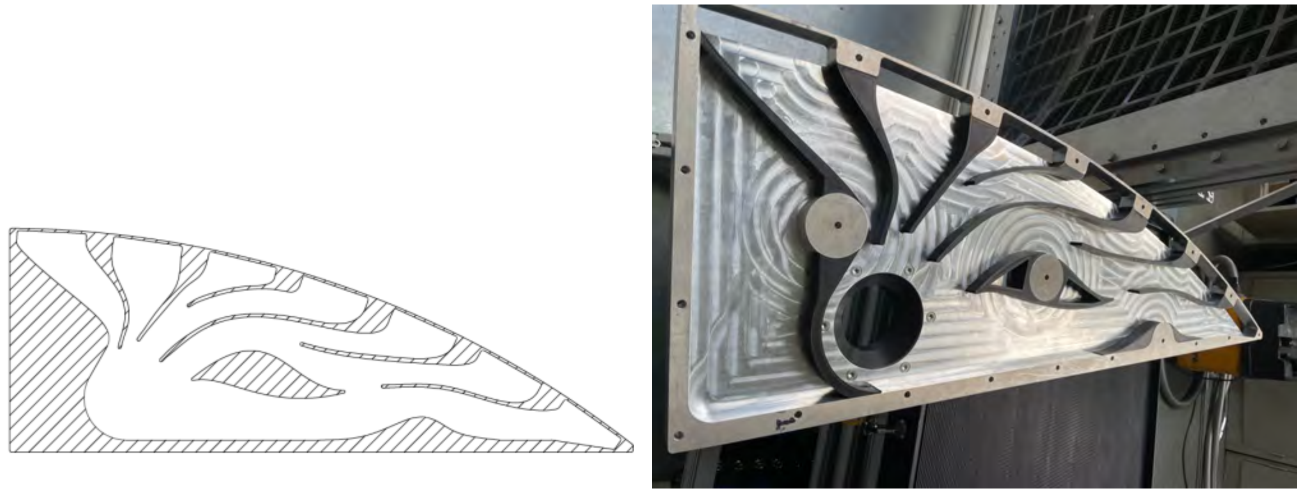

(a) Sketch of the modified air distribution plate. White areas represent the fluid domain.

(b) Air distribution plate modified with small 3d-printed pieces.

Figure B.2: Test of the homogenization concept provided by a research group of Warsaw.

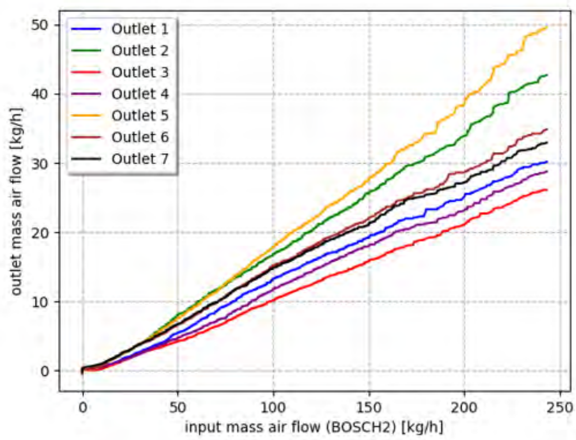

Figure B.3: Outlet MAF distribution with a modified ADP.

Blower Characteristics and Air Tempeature Evolution

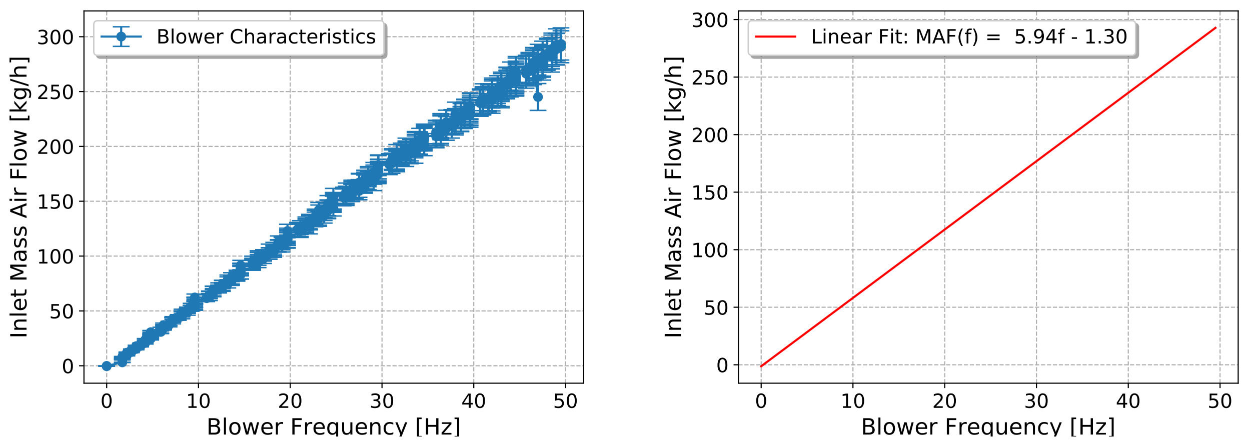

Figure B.4: Blower characteristics with one fully-equipped column.

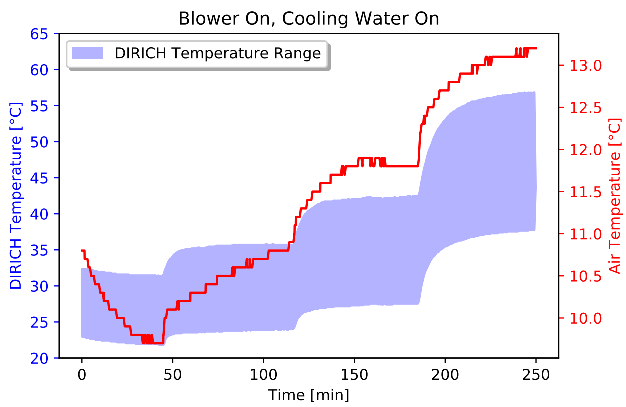

(a) Without active cooling water.

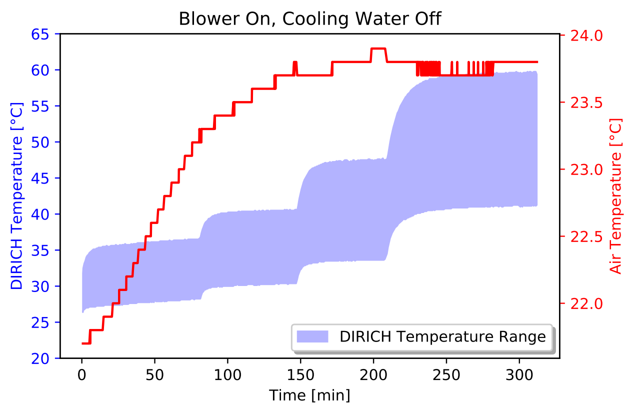

(b) With active cooling water.

Figure B.5: Air temperature evolution over time.

DiRICH Heat Maps

The temperature of each DiRICH-FEB was read out and saved in a csv-file. The DiRICH heat maps show the respective DiRICH temperatures with the corresponding address in the TrbNet. The heat maps shown here in the appendix have a fix color scale in order to get an idea on the temperature evolution in time, respectively in frequency and inlet mass air flow. During the measurement, up to 4 DiRICH-FEBs failed or were sorted out in advance. These appear with a white area in the heat map.

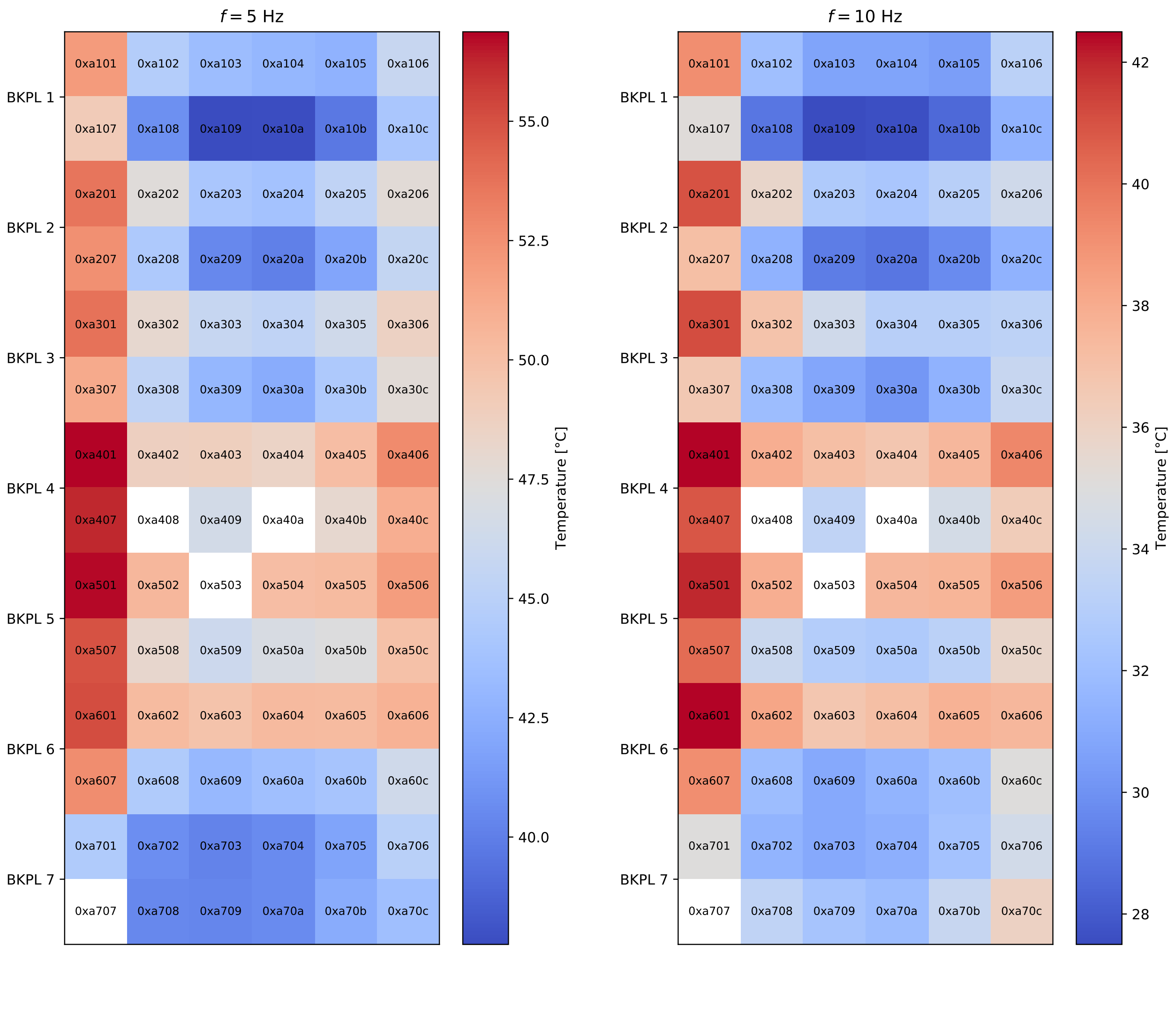

(a) MAF = 26.99 kg/h

(b) MAF = 56.21 kg/h

Figure B.6: DiRICH heat map with active cooling water for blower frequencies of 5 and 10 Hz, variable scale.

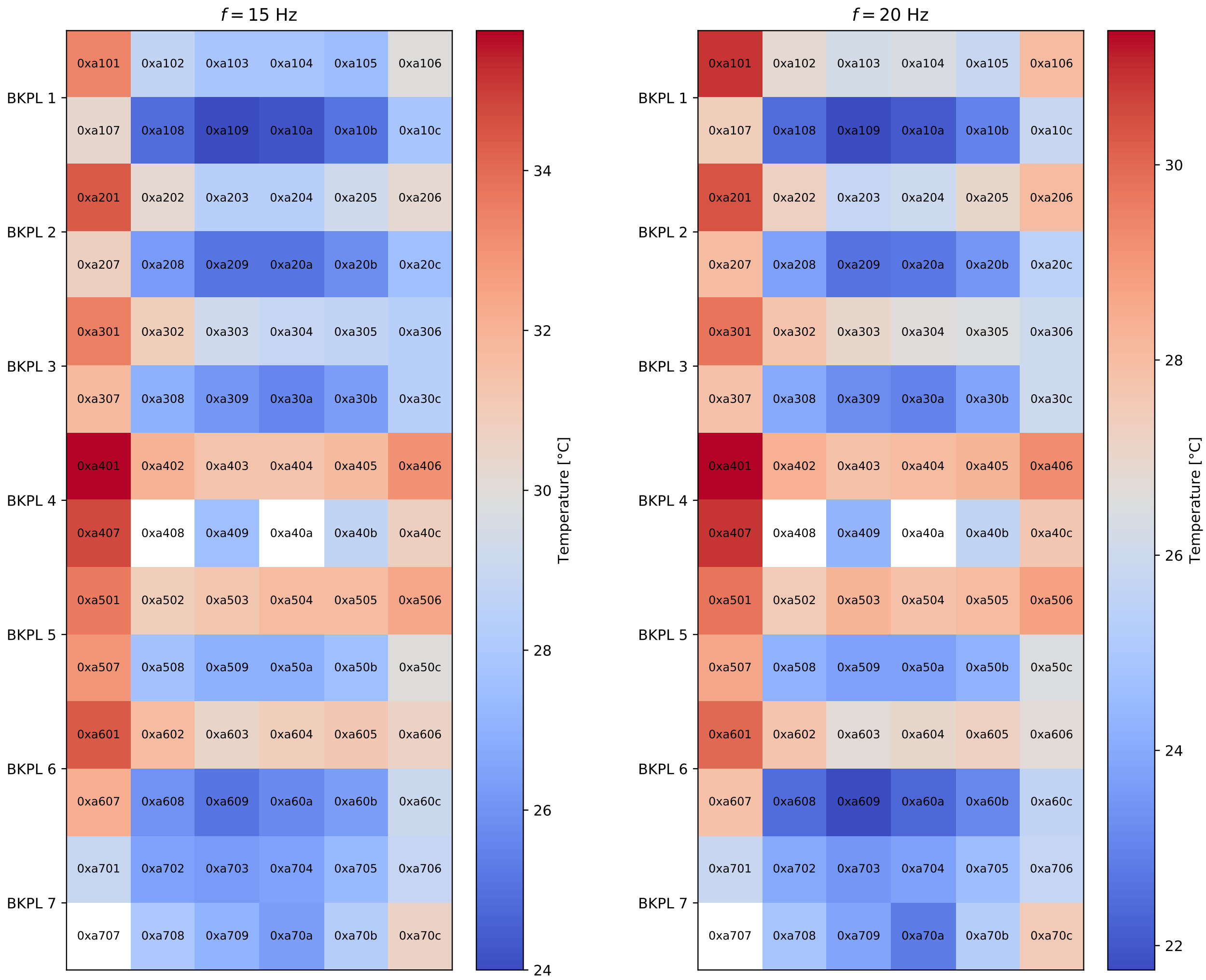

(a) MAF = 83.71 kg/h

(b) MAF = 112.24 kg/h

Figure B.7: DiRICH heat map with active cooling water for blower frequencies of 15 and 20 Hz, variable scale.

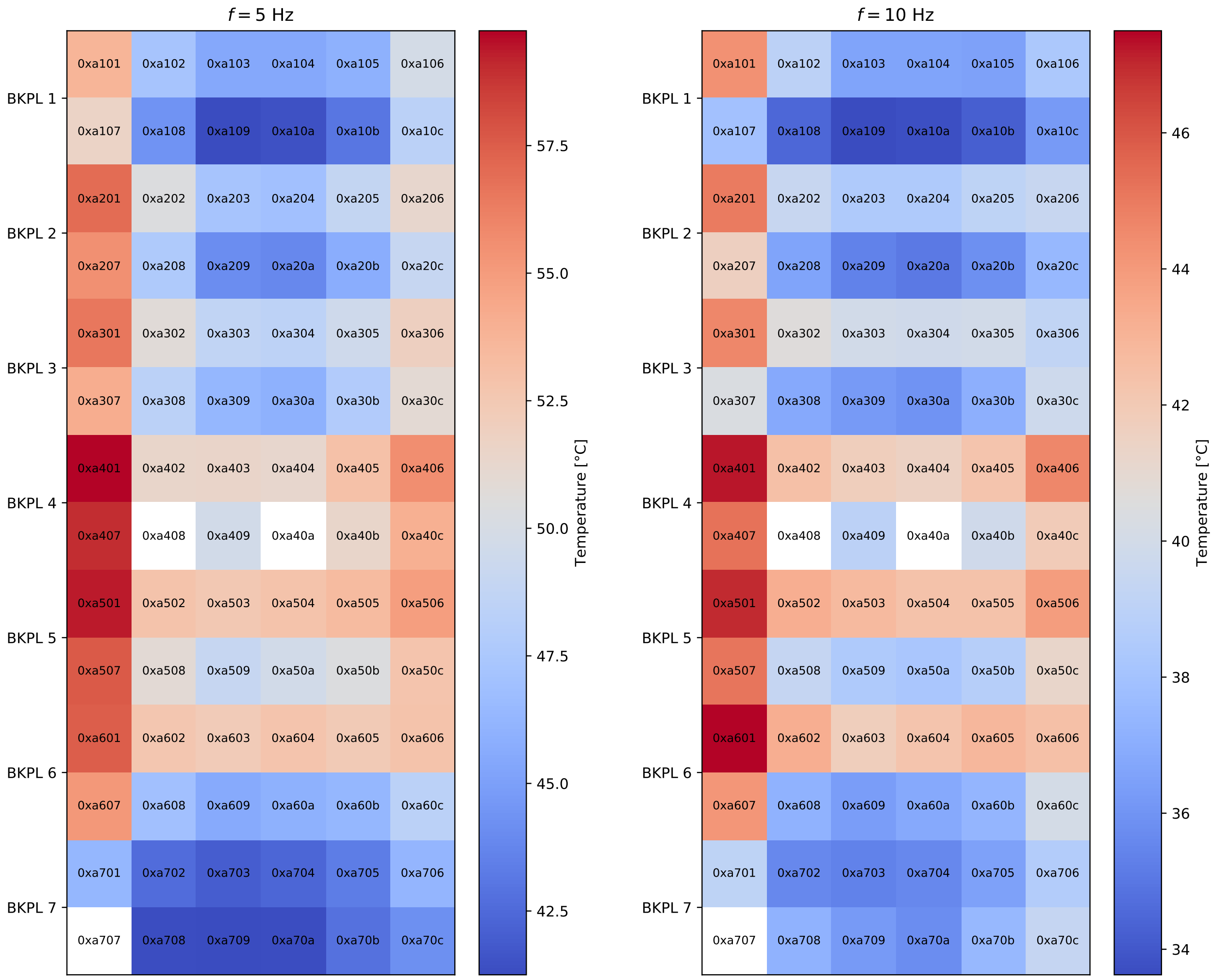

Figure B.8: DiRICH-FEB temperature presented in a heat map without active cooling water for blower frequencies of 5 and 10 Hz, variable color scale.

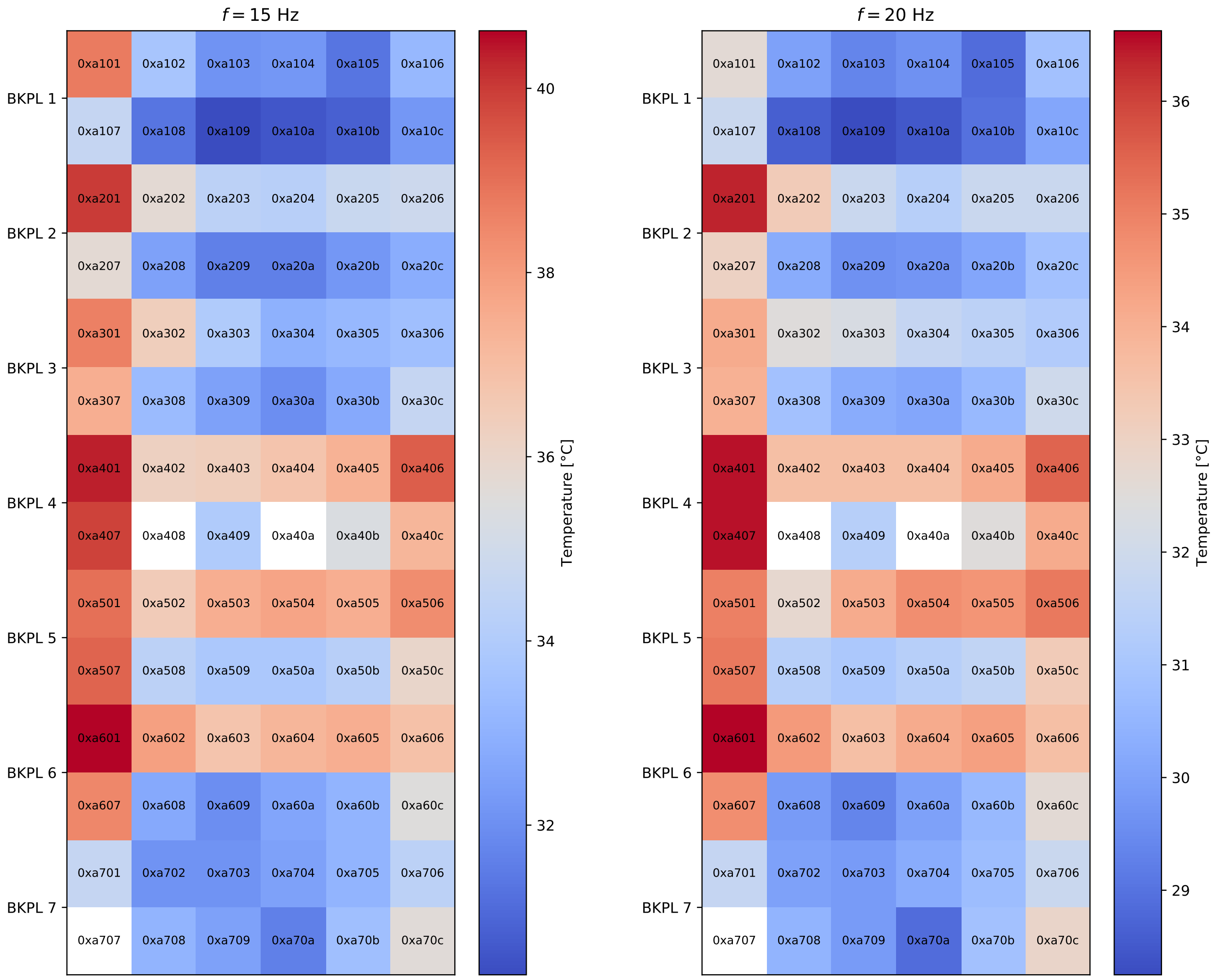

Figure B.9: DiRICH-FEB temperature presented in a heat map without active cooling water for blower frequencies of 15 and 20 Hz, variable color scale.

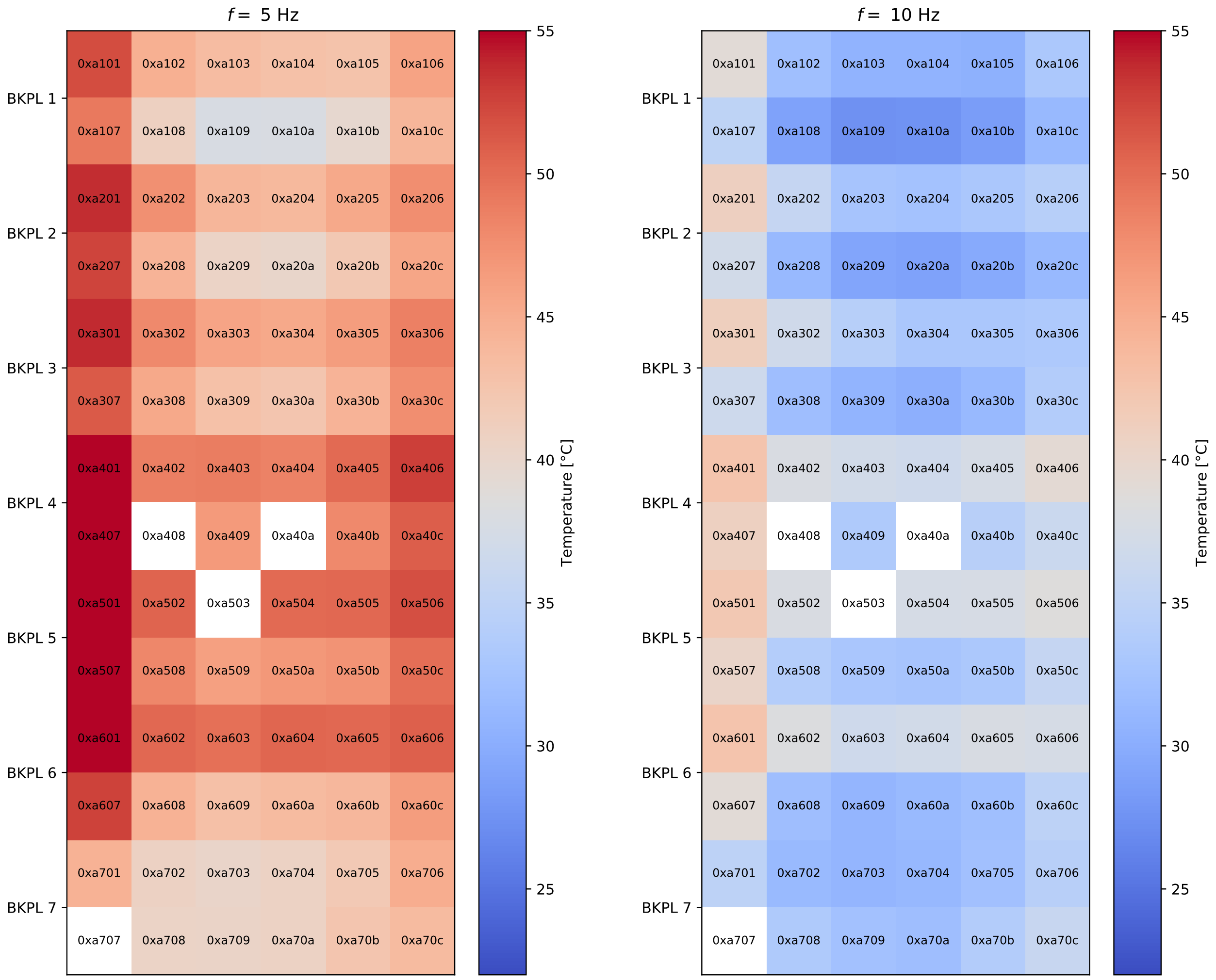

Figure B.10: DiRICH heat map with active cooling water for blower frequencies of 5 and 10 Hz, fixed scale.

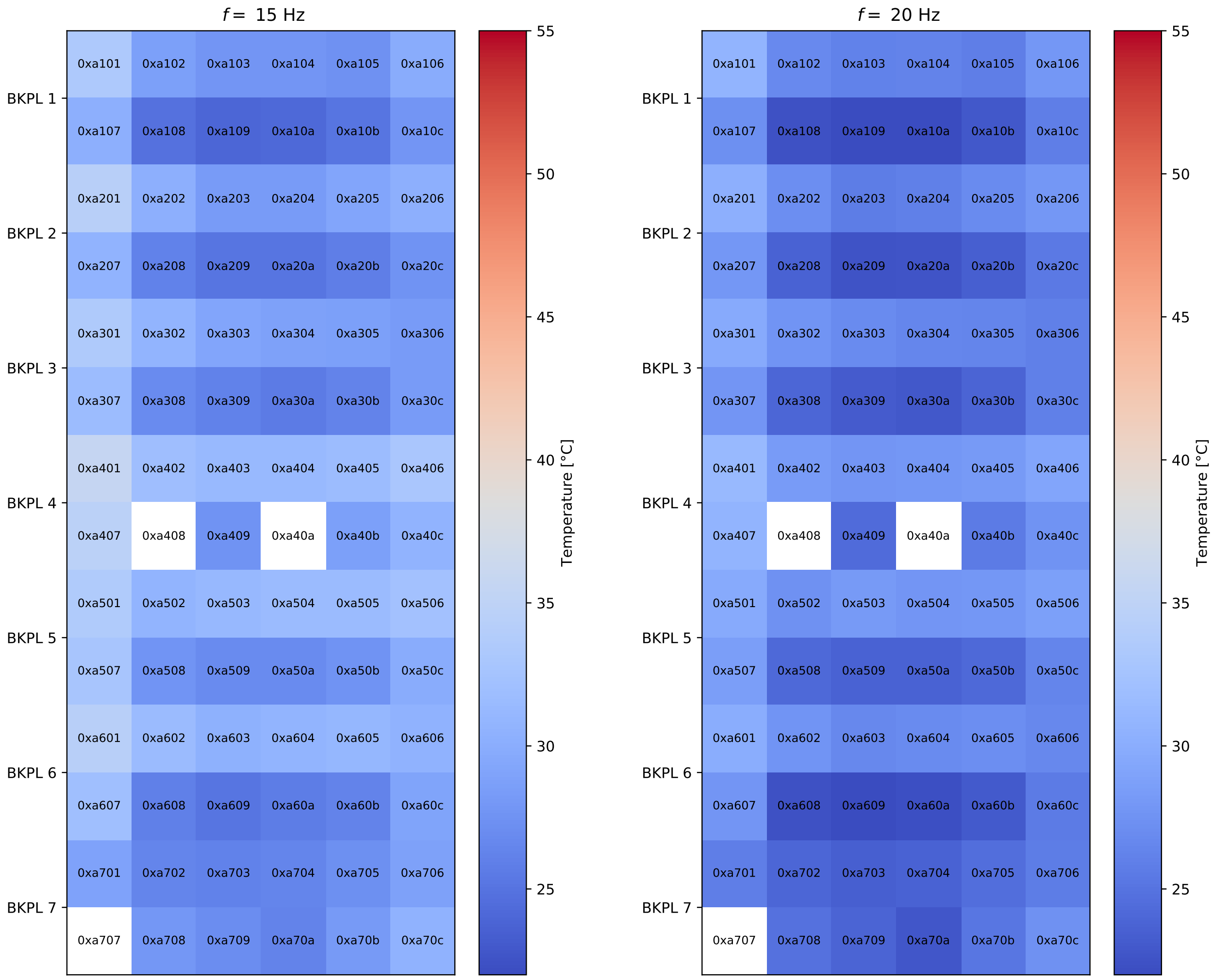

Figure B.11: DiRICH heat map with active cooling water for blower frequencies of 15 and 20 Hz, fixed scale.

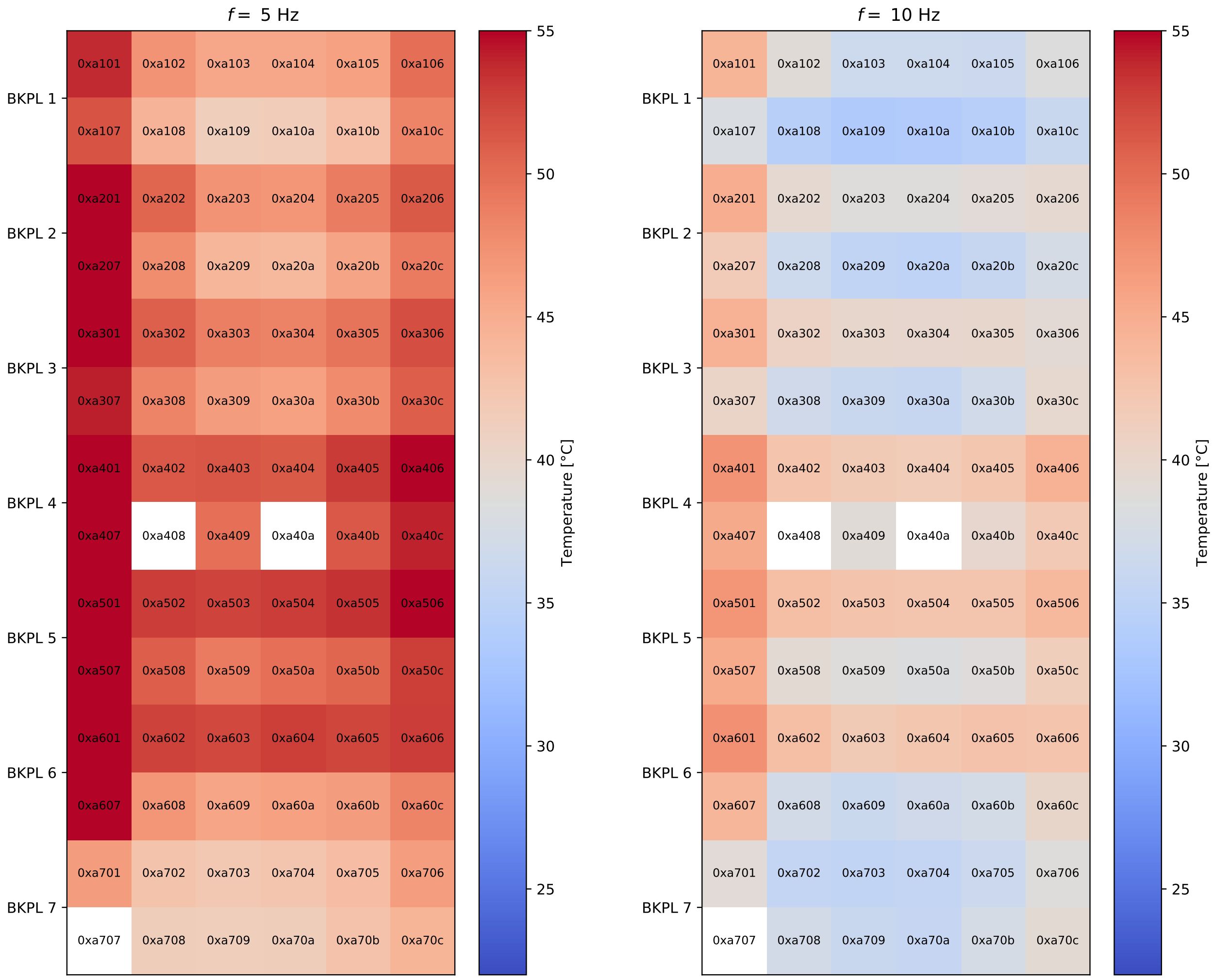

Figure B.12: DiRICH heat map without active cooling water for blower frequencies of 5 and 10 Hz, fixed scale.

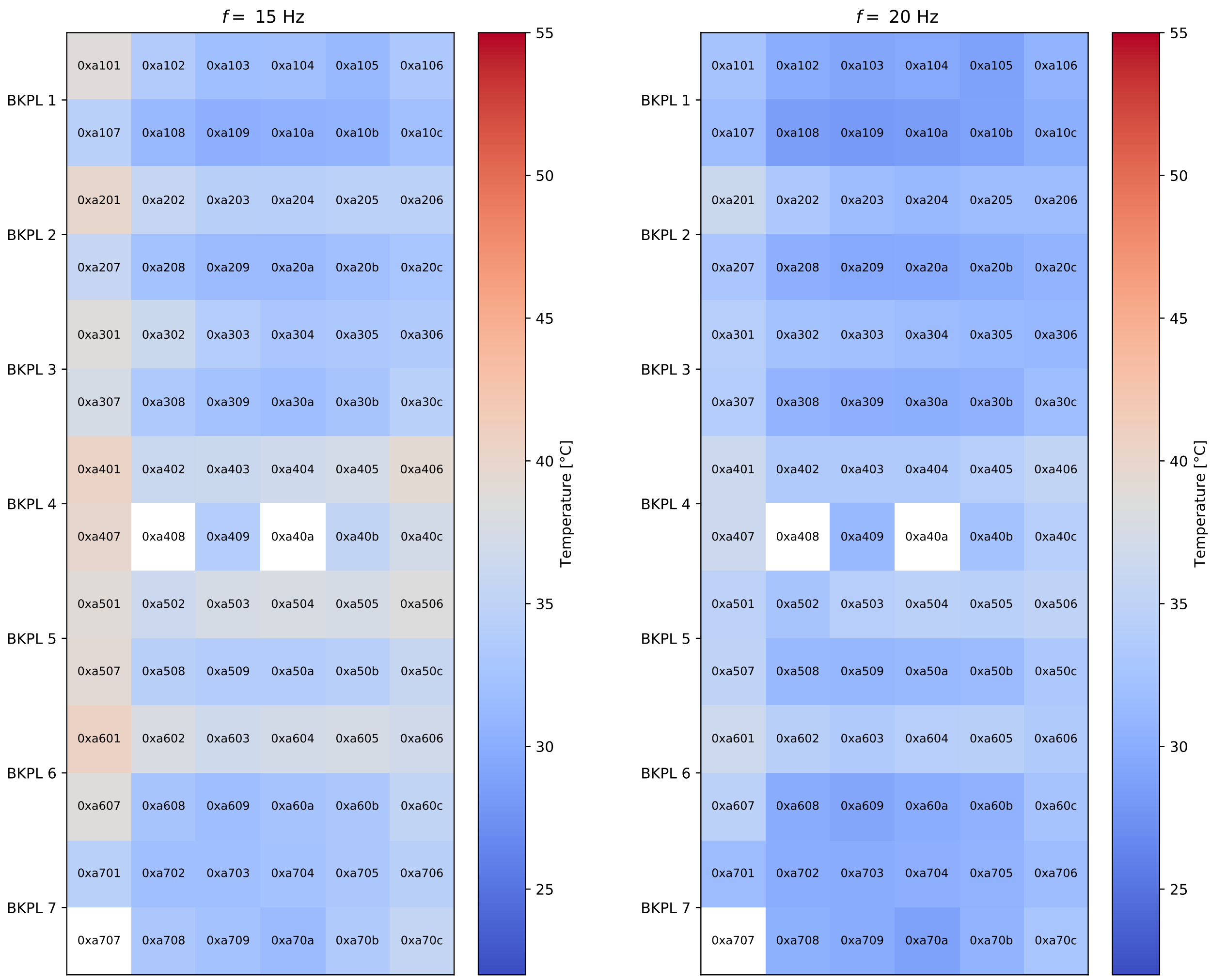

Figure B.13: DiRICH heat map without active cooling water for blower frequencies of 15 and 20 Hz, fixed scale.

Backplane and MAPMT Temperatures

The temperature of each backplane is determined by taking the average of all DiRICH-FEB temperatures that are assigned to the corresponding backplane (frequency-dependent heat map trend shown in Fig. 7.30 and average backplane temperature comparisons at two different cooling air temperatures shown in Fig. B.16). Hereby, the MAPMT temperatures are extracted from the thermal images shown in Fig. B.18–B.26. An overview of the MAPMT temperature measured with and without device cover for each backplane is shown in Fig. B.15, here for the case of missing active cooling water.

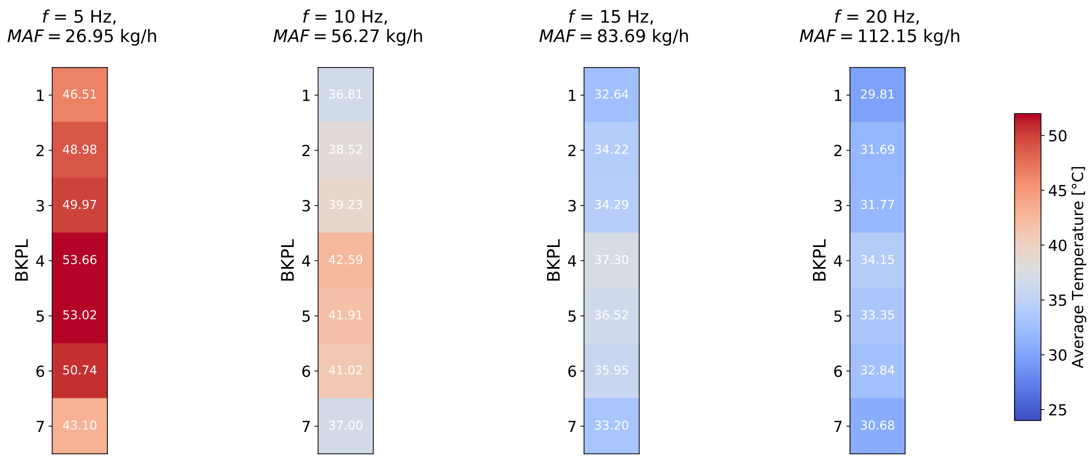

Figure B.14: Backplane average temperature heat map at different blower frequencies, fixed color scale.

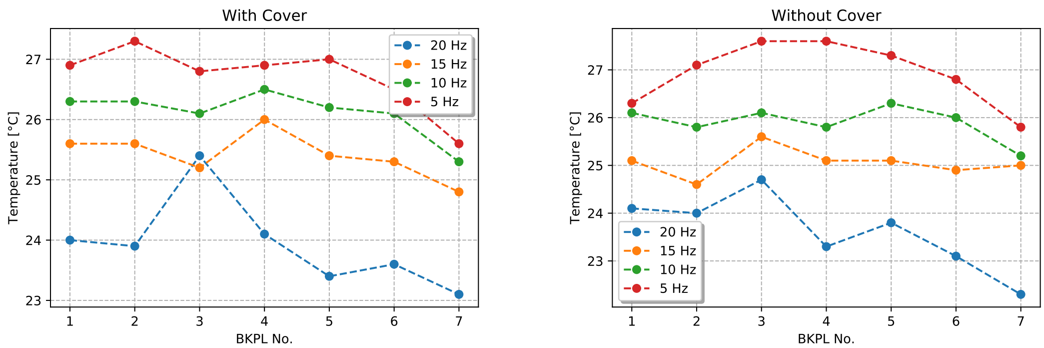

Figure B.15: MAPMT temperatures at each backplane for different blower frequencies, without active cooling water.

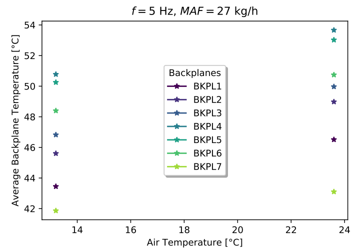

(a) BKPL at 5 Hz.

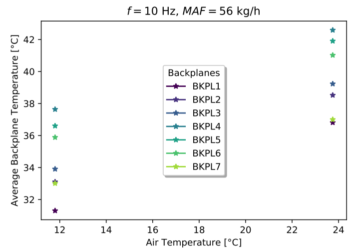

(b) BKPL at 10 Hz.

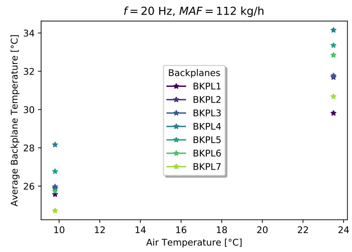

(c) BKPL at 20 Hz.

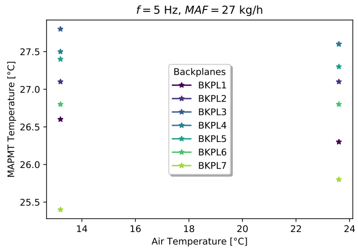

(d) MAPMT at 5 Hz.

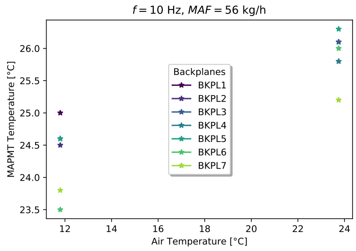

(e) MAPMT at 10 Hz.

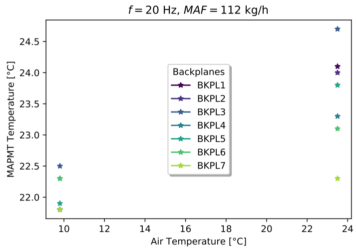

(f) MAPMT at 20 Hz.

Figure B.16: Comparison of MAPMT temperatures at equal blower frequency but different air temperatures.

Thermal Images of the MAPMTs

All infrared images of the MAPMTs, the PMT-side and the electronics-side of the camera were taken with a FLIR thermal imaging camera. The temperature distribution over the rectangular MAPMT shape was largely homogeneous. The camera was operated in measuring mode. Within the scope of the temperature measurements, an attempt was always made to target a reproducible measuring point. This method was proven as justified by comparative measurements with a digital thermometer. Each thermal image was taken twice: one with the plastic cap that covers the photocathode of the MAPMT and one without, such that possible reflections of the MAPMT glass can be excluded.

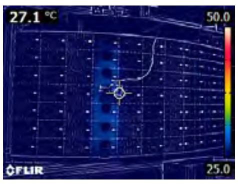

(a) 20 Hz

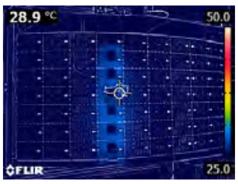

(b) 15 Hz

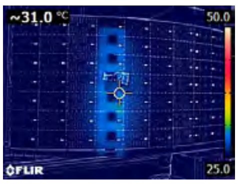

(c) 10 Hz

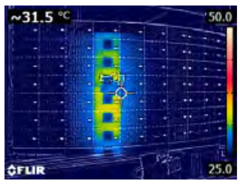

(d) 5 Hz

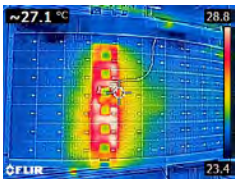

(e) 20 Hz

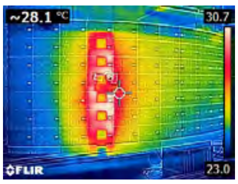

(f) 15 Hz

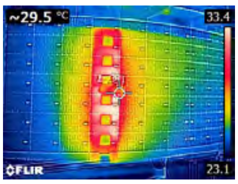

(g) 10 Hz

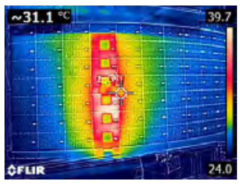

(h) 5 Hz

Figure B.17: Thermal images of the back of the RICH camera prototype taken with an infrared camera for 4 different fan frequencies with no active cooling water. (a)-(d) illustrates the temperature at a fixed scale, (e)-(h) for a variable scale. Compared to Fig. 7.23 where the cooling water was turned on, a significant increase in temperatures is recorded.

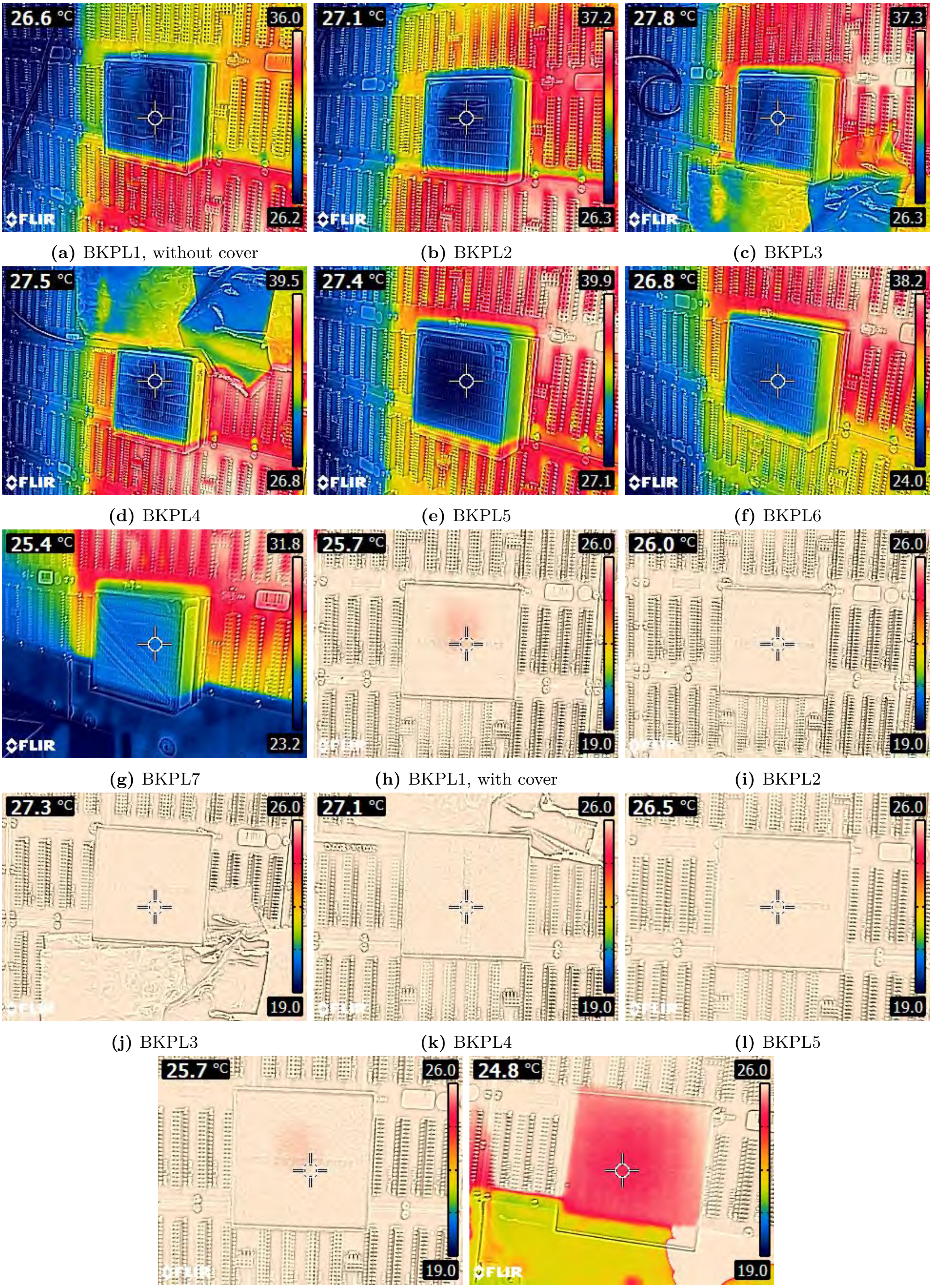

(a) BKPL1, without cover **(b)** BKPL2 **(c)** BKPL3

(d) BKPL4 **(e)** BKPL5 **(f)** BKPL6

(g) BKPL7 **(h)** BKPL1, with cover **(i)** BKPL2

(j) BKPL3 **(k)** BKPL4 **(l)** BKPL5

(m) BKPL6 **(n)** BKPL7

Figure B.18: Thermal images of the MAPMTs, $f = 5$ Hz, blower on, cooling water on.

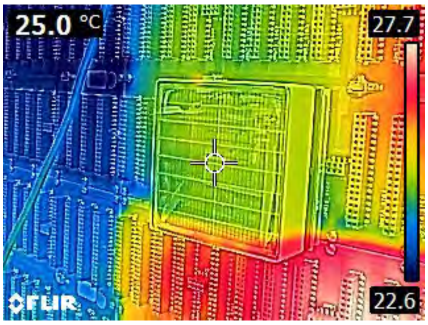

(a) BKPL1, without cap

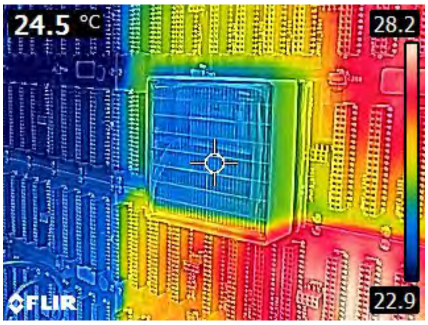

(b) BKPL2

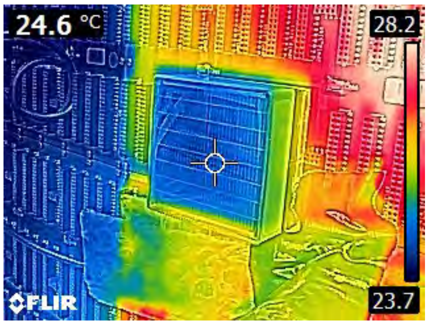

(c) BKPL3

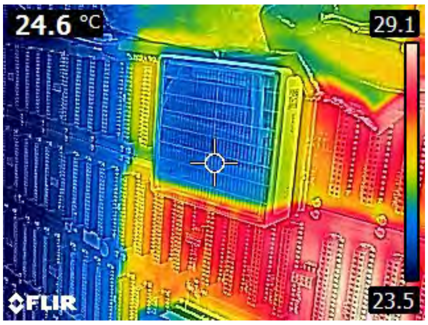

(d) BKPL4

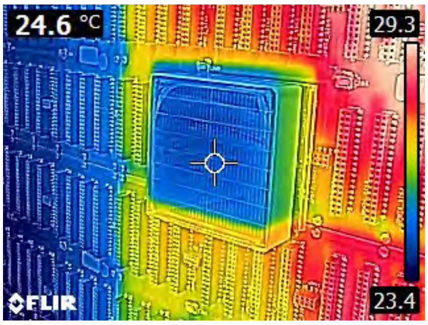

(e) BKPL5

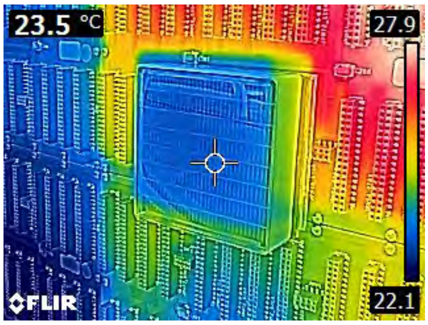

(f) BKPL6

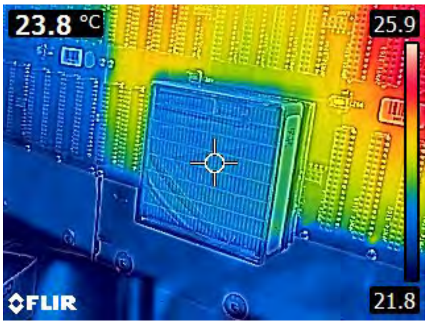

(g) BKPL7

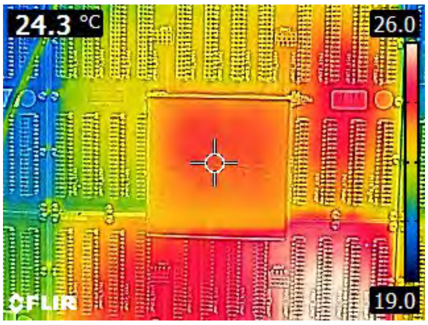

(h) BKPL1, with cap

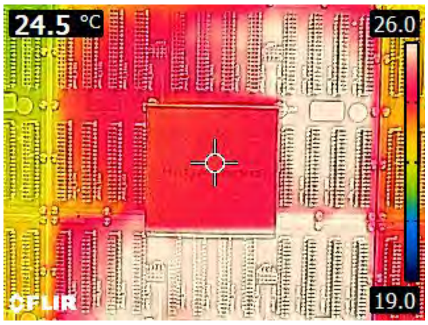

(i) BKPL2

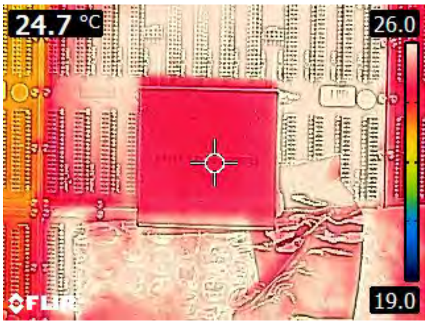

(j) BKPL3

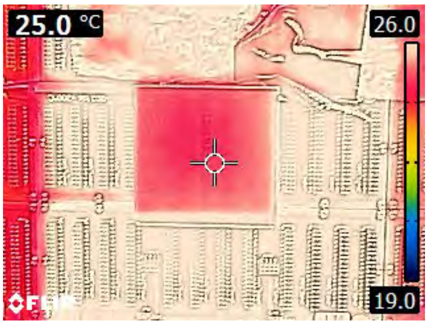

(k) BKPL4

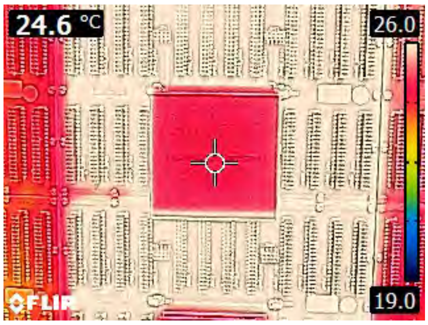

(l) BKPL5

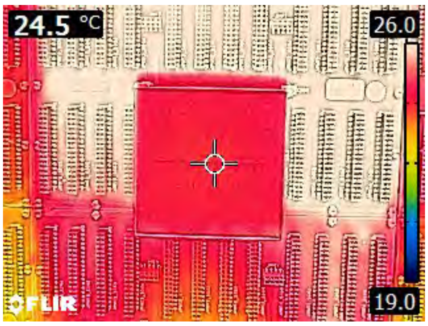

(m) BKPL6

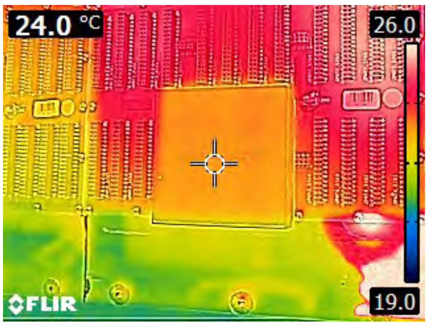

(n) BKPL7

Figure B.19: Thermal images of the MAPMTs, $f = 10$ Hz, blower on, cooling water on.

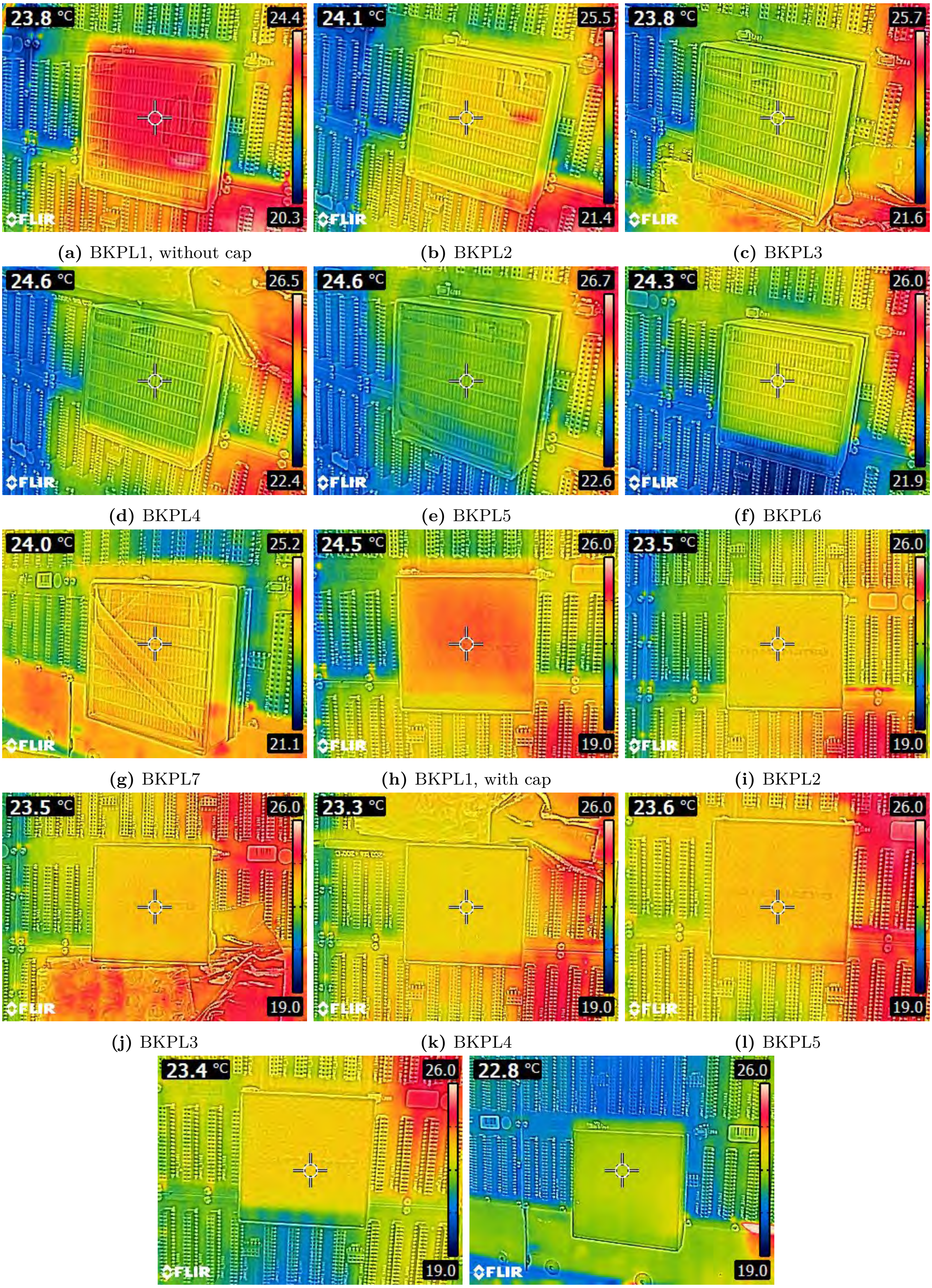

(a) BKPL1, without cap **(b)** BKPL2 **(c)** BKPL3

(d) BKPL4 **(e)** BKPL5 **(f)** BKPL6

(g) BKPL7 **(h)** BKPL1, with cap **(i)** BKPL2

(j) BKPL3 **(k)** BKPL4 **(l)** BKPL5

(m) BKPL6 **(n)** BKPL7

Figure B.20: Thermal images of the MAPMTs, $f = 15$ Hz, blower on, cooling water on.

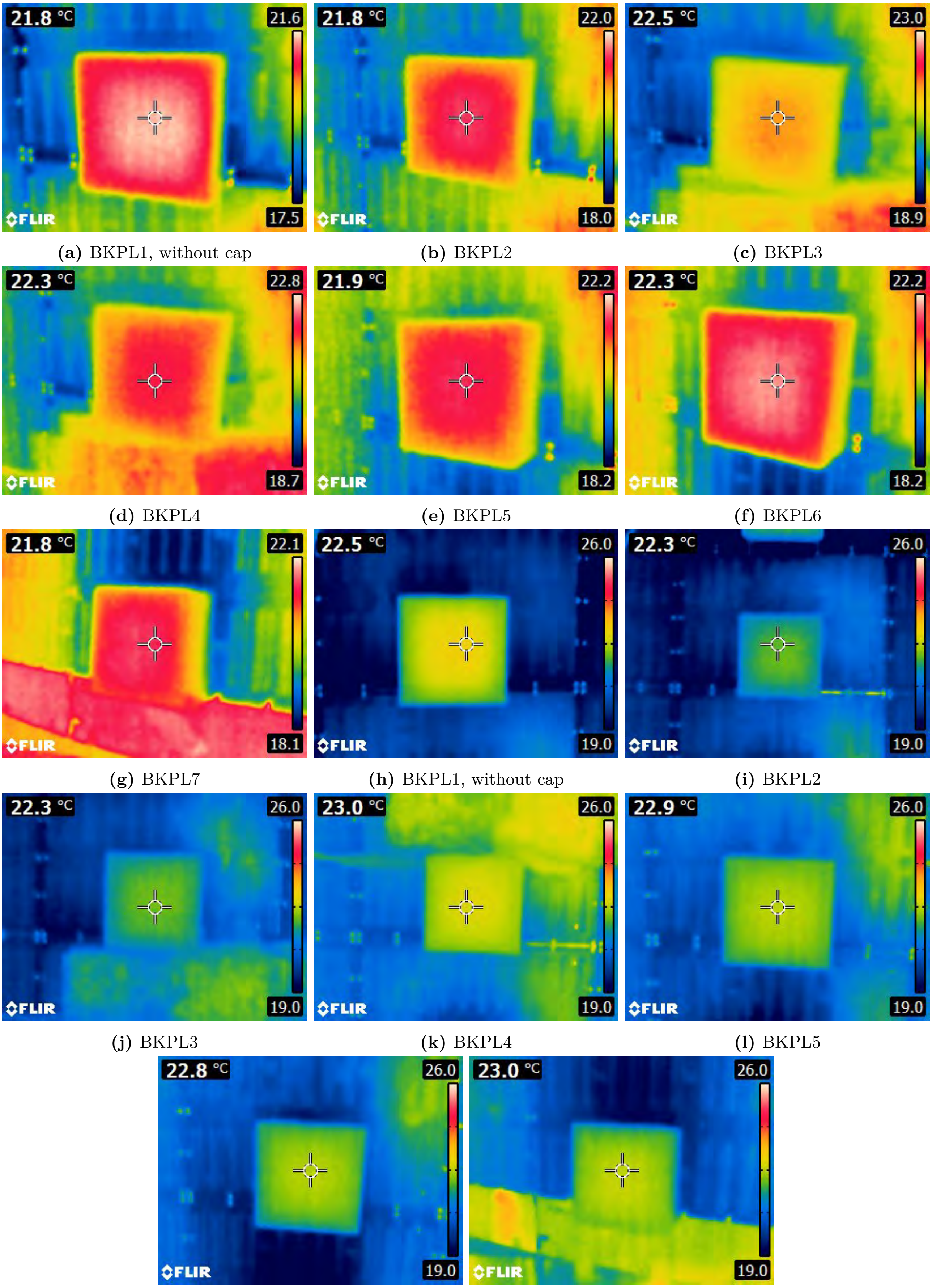

(a) BKPL1, without cap **(b)** BKPL2 **(c)** BKPL3

(d) BKPL4 **(e)** BKPL5 **(f)** BKPL6

(g) BKPL7 **(h)** BKPL1, without cap **(i)** BKPL2

(j) BKPL3 **(k)** BKPL4 **(l)** BKPL5

(m) BKPL6 **(n)** BKPL7

Figure B.21: Thermal images of the MAPMTs, $f = 20$ Hz, blower on, cooling water on.

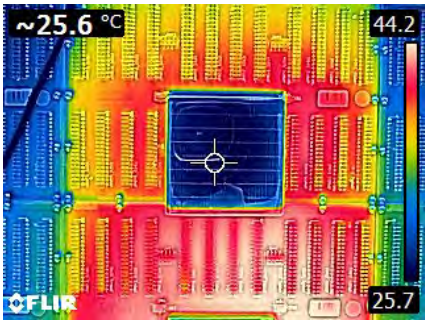

(a) BKPL1

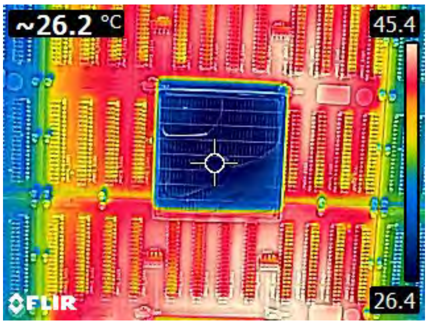

(b) BKPL2

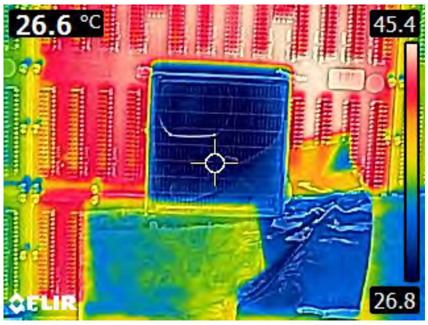

(c) BKPL3

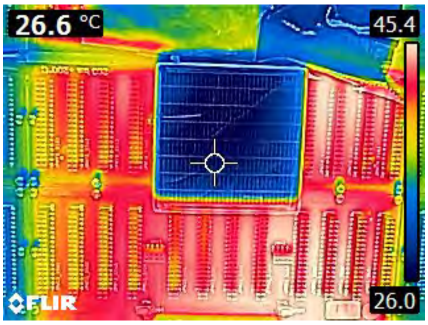

(d) BKPL4

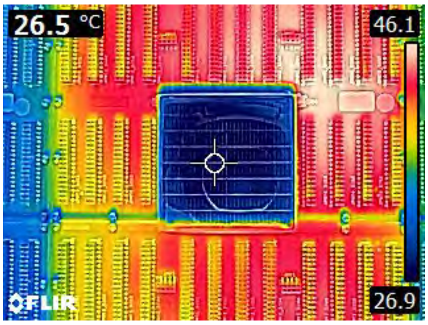

(e) BKPL5

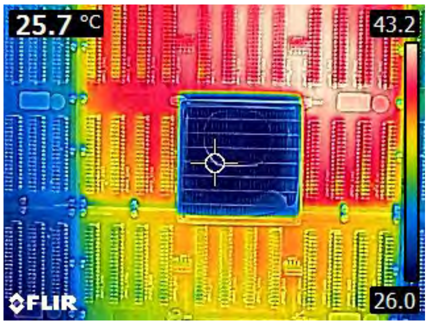

(f) BKPL6

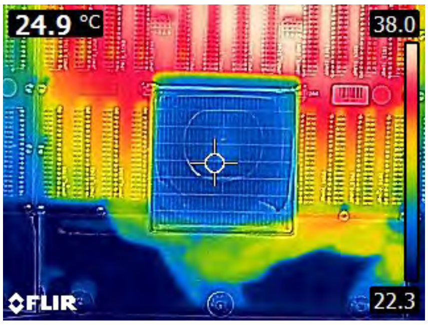

(g) BKPL7

Figure B.22: Thermal images of the MAPMTs, $f = 0$ Hz, blower off, cooling water off. Images are taken only with the plastic caps.

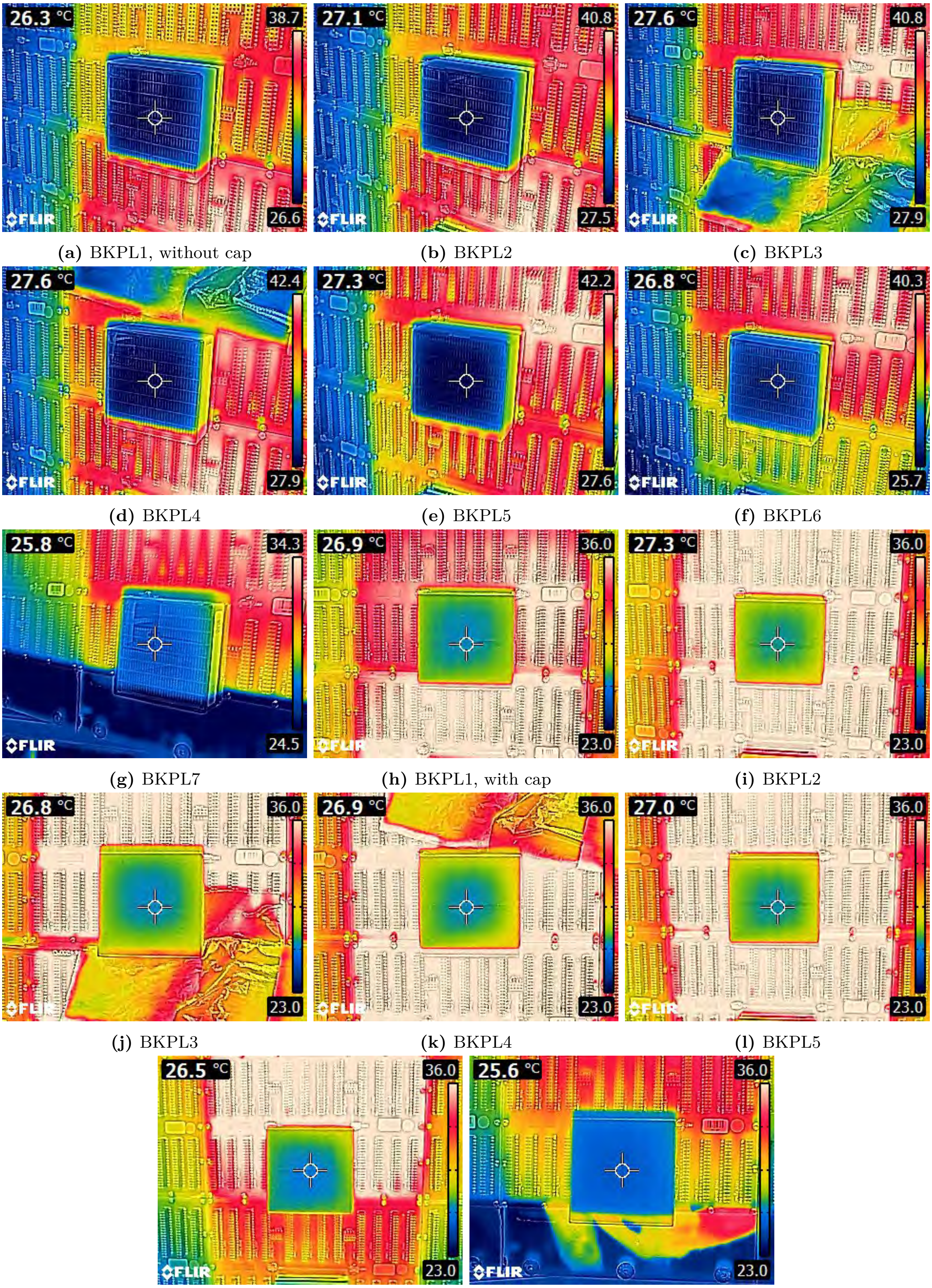

(a) BKPL1, without cap **(b)** BKPL2 **(c)** BKPL3

(d) BKPL4 **(e)** BKPL5 **(f)** BKPL6

(g) BKPL7 **(h)** BKPL1, with cap **(i)** BKPL2

(j) BKPL3 **(k)** BKPL4 **(l)** BKPL5

(m) BKPL6 **(n)** BKPL7

Figure B.23: Thermal images of the MAPMTs, $f = 5$ Hz, blower on, cooling water off.

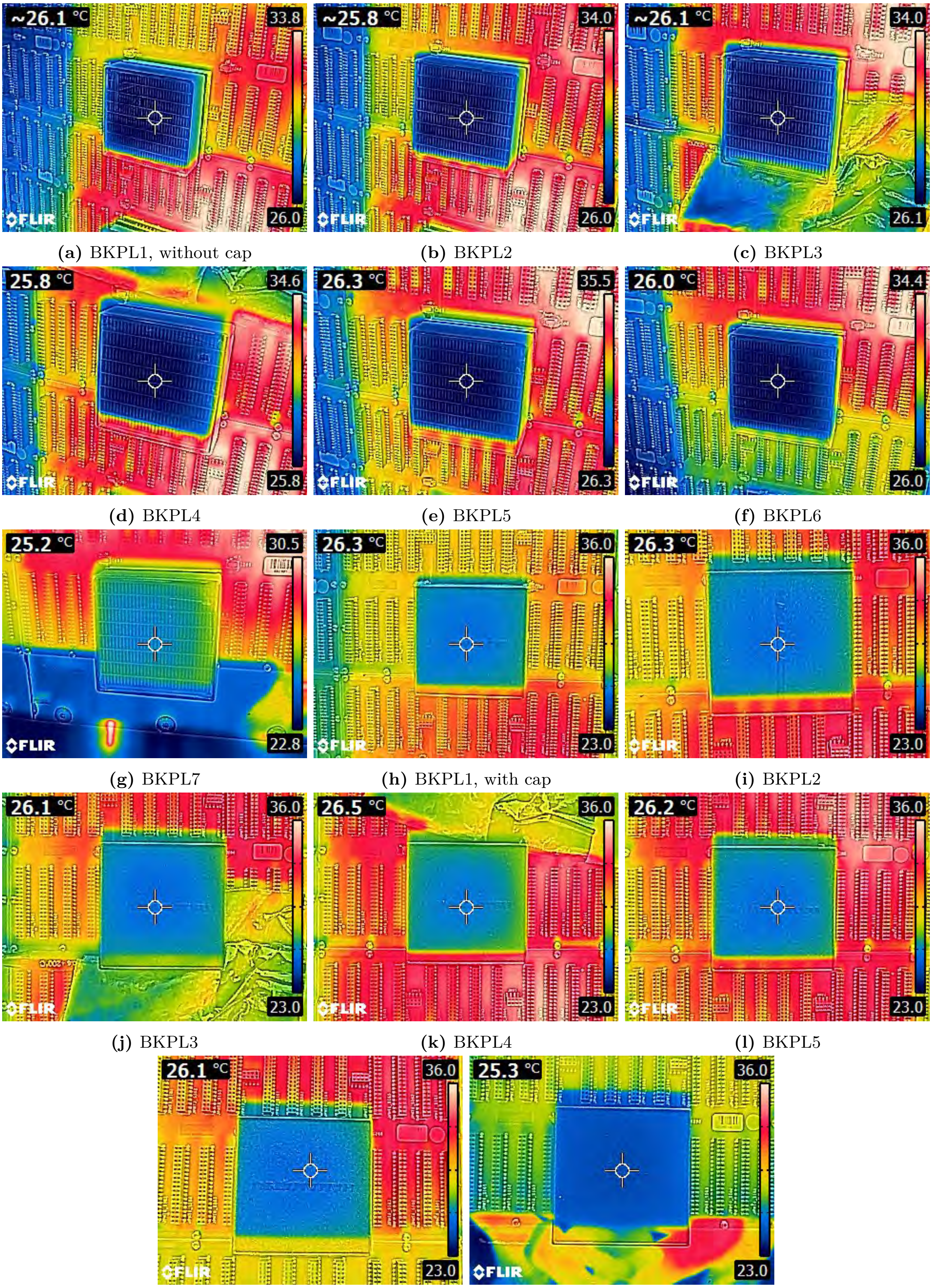

(a) BKPL1, without cap **(b)** BKPL2 **(c)** BKPL3

(d) BKPL4 **(e)** BKPL5 **(f)** BKPL6

(g) BKPL7 **(h)** BKPL1, with cap **(i)** BKPL2

(j) BKPL3 **(k)** BKPL4 **(l)** BKPL5

(m) BKPL6 **(n)** BKPL7

Figure B.24: Thermal images of the MAPMTs, $f = 10$ Hz, blower on, cooling water off.

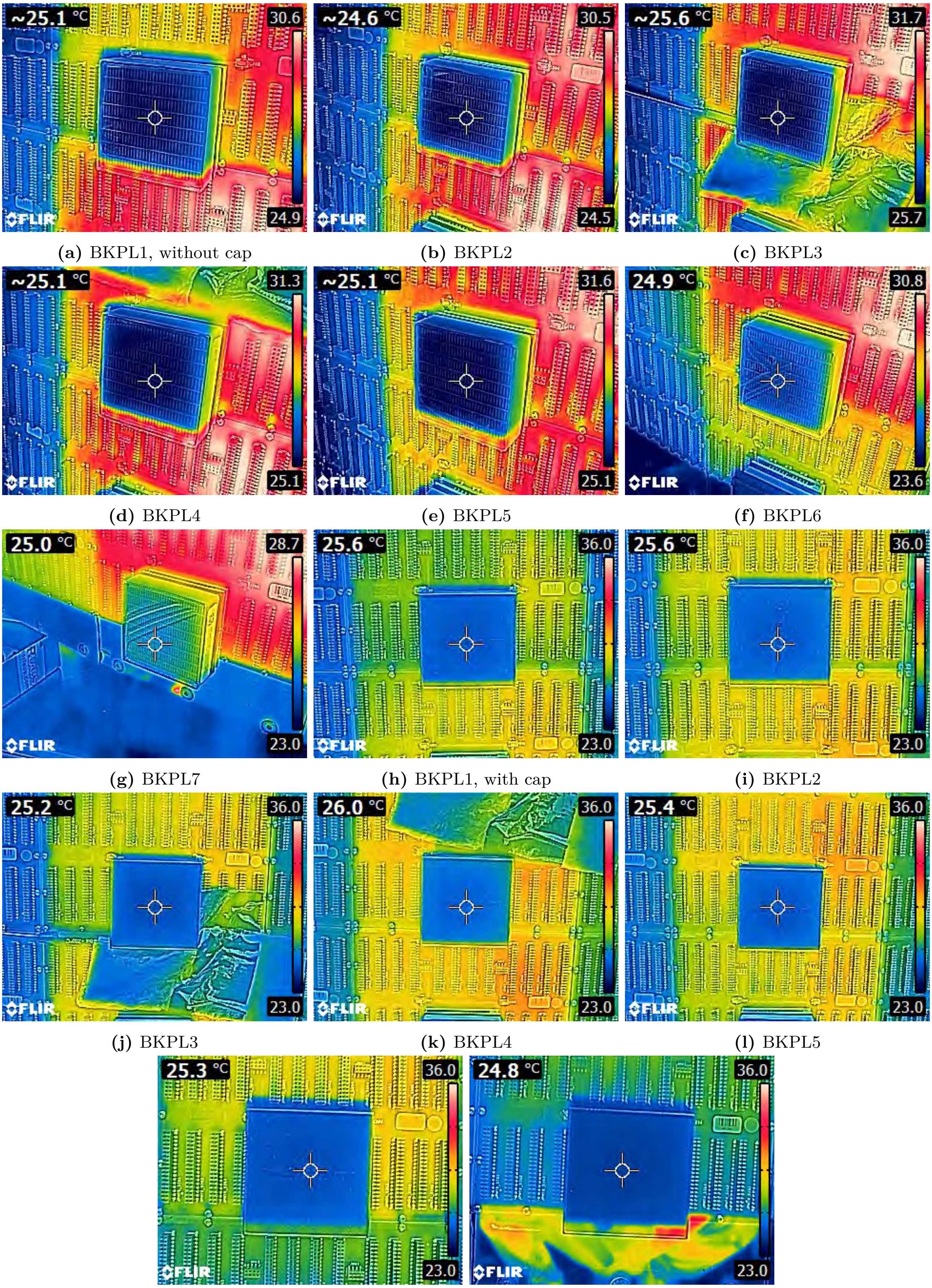

(a) BKPL1, without cap **(b)** BKPL2 **(c)** BKPL3

(d) BKPL4 **(e)** BKPL5 **(f)** BKPL6

(g) BKPL7 **(h)** BKPL1, with cap **(i)** BKPL2

(j) BKPL3 **(k)** BKPL4 **(l)** BKPL5

(m) BKPL6 **(n)** BKPL7

Figure B.25: Thermal images of the MAPMTs, $f = 15$ Hz, blower on, cooling water off.

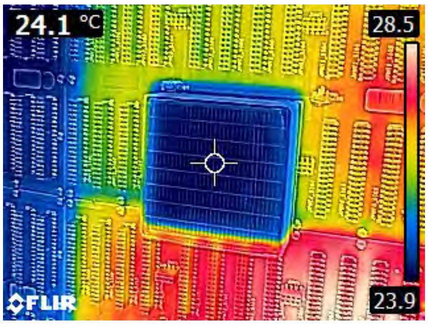

(a) BKPL1, without cap

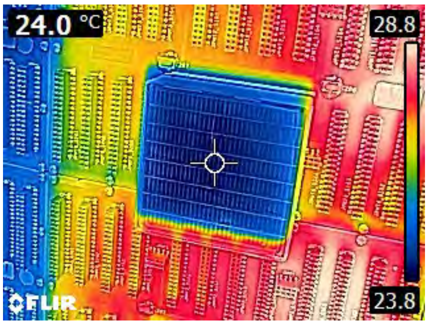

(b) BKPL2

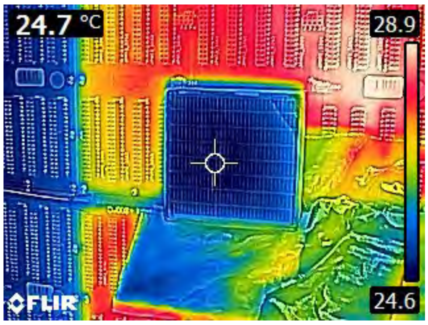

(c) BKPL3

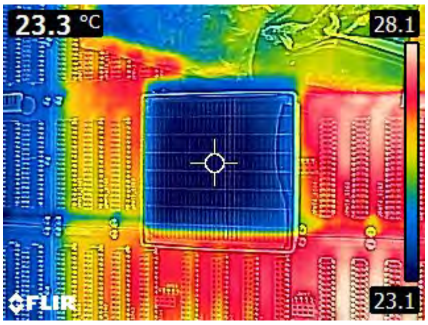

(d) BKPL4

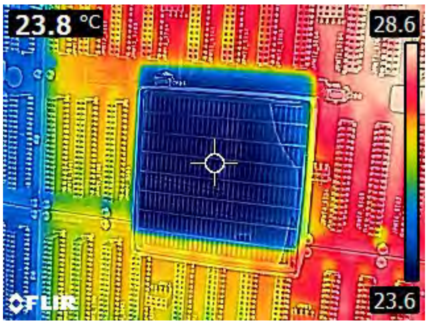

(e) BKPL5

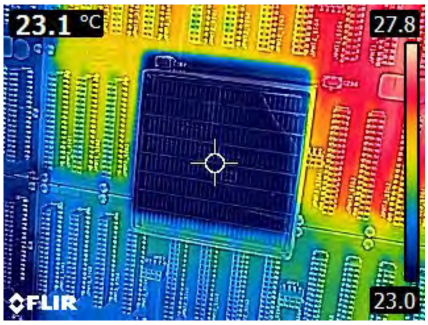

(f) BKPL6

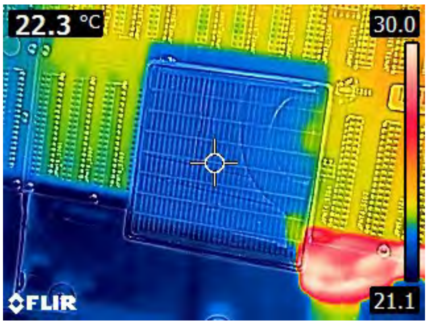

(g) BKPL7

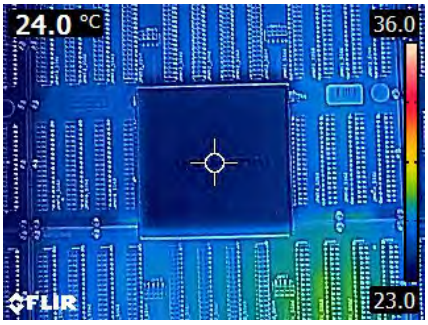

(h) BKPL1, with cap

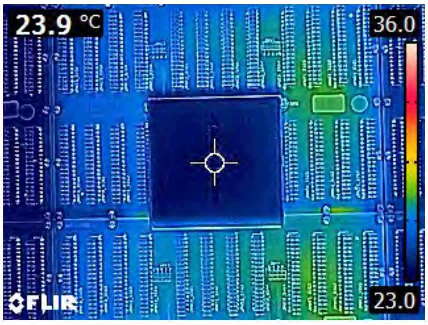

(i) BKPL2

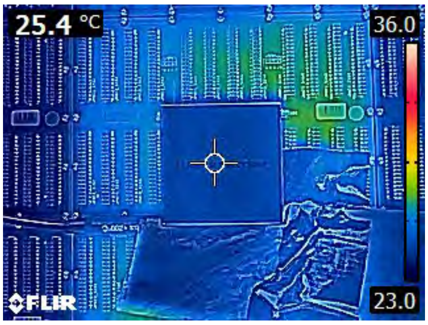

(j) BKPL3

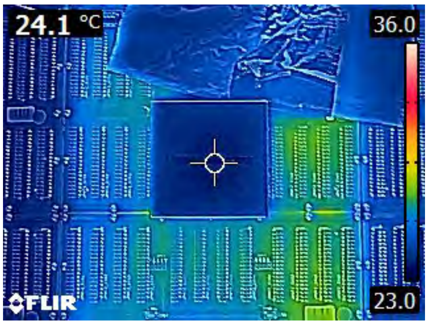

(k) BKPL4

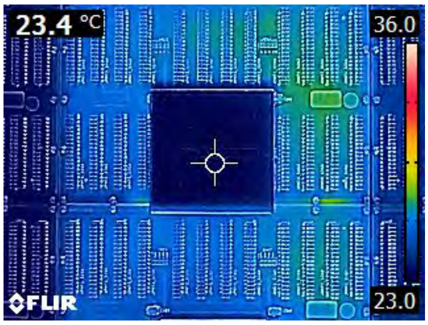

(l) BKPL5

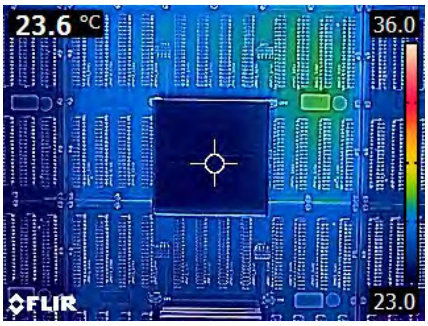

(m) BKPL6

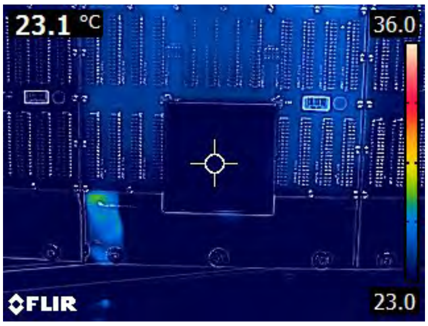

(n) BKPL7

Figure B.26: Thermal images of the MAPMTs, $f = 20$ Hz, blower on, cooling water off.

C
Bibliography

[1] Technical Design Report for the CBM Ring Imaging Cherenkov Detector. Technical report, 2013. URL `https://repository.gsi.de/record/65526`.

[2] Ansys Fluent 12.0. Standard k-ε Model. `https://www.afs.enea.it/project/neptunius/docs/fluent/html/th/node58.htm`, . online; last retrieved on 2023/10/19.

[3] Ansys Fluent 12.0. Shear-Stress (SST) k-ω Model. `https://www.afs.enea.it/project/neptunius/docs/fluent/html/th/node67.htm`, . online; last retrieved on 2023/10/19.

[4] Gert Aarts. Introductory lectures on lattice qcd at nonzero baryon number. In *Journal of Physics: Conference Series*, volume 706, page 022004. IOP Publishing, 2016.

[5] Altair AcuSolve. General Form of Turbulence Models. `https://2021.help.altair.com/2021/hwsolvers/acusolve/topics/acusolve/training_manual/gen_form_of_turb_models_r.htm/`, . online; last retrieved on 2023/10/19.

[6] Altair AcuSolve. Reynolds-Averaged Navier-Stokes (RANS) Simulations. `https://2021.help.altair.com/2021/hwsolvers/acusolve/topics/acusolve/training_manual/rans_simulations_r.htm/`, . online; last retrieved on 2023/10/19.

[7] Altair AcuSolve. Turbulence Modeling. `https://2021.help.altair.com/2021/hwsolvers/acusolve/topics/acusolve/training_manual/turbulence_modeling_r.htm`, . online; last retrieved on 2023/10/19.

[8] J Adamczewski-Musch, O Arnold, C Behnke, A Belounnas, A Belyaev, JC Berger-Chen, Jacek Biernat, A Blanco, C Blume, M Böhmer, et al. Probing dense baryon-rich matter with virtual photons. *Nature Physics*, 15(10):1040–1045, 2019.

[9] Kshitij Agarwal. Status of the Compressed Baryonic Matter (CBM) Experiment at FAIR. *arXiv preprint arXiv:2207.14585*, 2022.

[10] Abobaker Mohammed Alakashi, Bambang Basuno, and Hasan Taher M Elkamel. Comparison between finite volume method (FVM) based on inviscid and viscous flow with experimental and fluent results. *Applied and Computational Mathematics*, 4(1-1):12–17, 2015.

[11] Argonne National Laboratory (ANL). Experimental physics and industrial control system. `https://epics.anl.gov/`. online; last retrieved on 2023/10/19.

[12] HD Baehr and K Stephan. Heat and mass transfer. ; Waerme-und Stoffuebertragung. 2006.

[13] BOSCH. Sensors air-mass, lambda, pressure, rotational-speed, structure-borne sound, temperature. https://www.boschoffhighway.com/xc/media/ledi/news/download_pdf/2022_01_sensors_ibusiness_en.pdf. online; last retrieved on 2023/10/19.

[14] Yunus Cengel and John Cimbala. *Ebook: Fluid mechanics fundamentals and applications (si units).* McGraw Hill, 2013.

[15] PA Cerenkov et al. Visible emission of clean liquids by action of γ radiation. *Dok Akad Nauk SSSR*, 2:451–454, 1934.

[16] Pavel Alekseevič Čerenkov. Visible radiation produced by electrons moving in a medium with velocities exceeding that of light. *Physical Review*, 52(4):378, 1937.

[17] SNS Controls CS-Studio. CS-Studio (Phoebus). https://controlssoftware.sns.ornl.gov/css_phoebus/. online; last retrieved on 2023/10/19.

[18] CSstudio. Control system studio. https://www.controlsystemstudio.org/. online; last retrieved on 2023/10/19.

[19] Marwan Darwish and Fadl Moukalled. *The finite volume method in computational fluid dynamics: an advanced introduction with OpenFOAM and Matlab.* Springer, 2016.

[20] John F Douglas. *Fluid mechanics.* Pearson education, 2005.

[21] Ansys Fluent. Ansys Fluent User Manual. https://www.fluid.tuwien.ac.at/322057?action=AttachFile&do=get&target=flu_ug.pdf, .

[22] Ansys Fluent. Ansys Fluent User Manual. https://www.fluid.tuwien.ac.at/322057?action=AttachFile&do=get&target=flu_ug.pdf, . p. 147, chapter 6.2.2.2 Cell Quality.

[23] Ansys Fluent. Logo CBM Experiment. https://sf.gsi.de/f/3a7f012186d74051ac8f/, .

[24] Jörg Förtsch. *Upgrade of the HADES RICH photon detector and first performance analyses.* PhD thesis, Dissertation, Wuppertal, Bergische Universität, 2021, 2021.

[25] I Frank and I Tamm. Coherent visible radiation of fast electrons passing through matter. In *Selected Papers*, pages 29–35. Springer, 1991.

[26] GSI Helmholtzzentrum für Schwerionenforschung GmbH. The particle accelerator facility of FAIR and GSI. https://www.gsi.de/fileadmin/_processed_/7/b/csm_FAIR-beschriftet_MSV_EN_Aug_2021_87549c53c0.jpg. Online; last retrieved on 2023/10/19.

[27] B+B Thermo-Technik GmbH. DATA SHEET Flow sensor element. https://shop.bb-sensors.com/out/media/Datasheet_Flow_sensor_FLW-122_new.pdf, . online; last retrieved on 2023/10/19.

[28] B+B Thermo-Technik GmbH. DATA SHEET Flow module Optimal for gas flow sensor evaluation Suitable for gas and liquid flow sensors. https://shop.bb-sensors.com/out/media/Operation_manual_flow_module_0555%200001.pdf, . online; last retrieved on 2023/10/19.

[29] Ulrich Heinz and Maurice Jacob. Evidence for a new state of matter: An assessment of the results from the CERN lead beam programme. *arXiv preprint nucl-th/0002042*, 2000.

[30] idealsimulations. Turbulence Models In CFD. `https://www.idealsimulations.com/resources/turbulence-models-in-cfd/`. online; last retrieved on 2023/10/19.

[31] JV Jelley. Čerenkov radiation: Its origin, properties and applications. *Contemporary Physics*, 3(1): 45–57, 1961.

[32] Gabriele Carcassi Kay Kasemir. Control System Studio Guide - For installers and maintainers of CSS. `https://www-lcls.slac.stanford.edu/web/epics_2012_04/presentations/Kasemir_Carcassi_css_guide.pdf`. online; last retrieved on 2023/10/19.

[33] Hermann Kolanoski and Norbert Wermes. *Teilchendetektoren*. Springer, 2016.

[34] Brian Edward Launder and Dudley Brian Spalding. The numerical computation of turbulent flows. In *Numerical prediction of flow, heat transfer, turbulence and combustion*, pages 96–116. Elsevier, 1983.

[35] Dan B Marghitu. *Mechanical engineer's handbook*. Elsevier, 2001. pp. Section 402.1 Page 6.

[36] CFD Online. Standard k-epsilon model. `https://www.cfd-online.com/Wiki/Standard_k-epsilon_model`, . online; last retrieved on 2023/10/19.

[37] CFD Online. SST k-omega model. `https://www.cfd-online.com/Wiki/Wilcox%27s_k-omega_model`, . online; last retrieved on 2023/10/19.

[38] Control-System-Studio Phoebus. Phoebus 1.0 documentation. `https://control-system-studio.readthedocs.io/en/latest/`. online; last retrieved on 2023/10/19.

[39] Martin Rein. *Einführung in die Strömungsmechanik*. Universitätsverlag Göttingen, 2020.

[40] Craig D Roberts. Perspective on the origin of hadron masses. *Few-Body Systems*, 58:1–12, 2017.

[41] Krystian Roslon. CFD calculations for airflow in camera cooling system. Warsaw University of Technology, 2022.

[42] Yury Ryabov. CBM RICH mechanical design. `https://indico.gsi.de/event/3620/contributions/16110/attachments/11687/14326/YuRyabov_CbmWeek_MechDesign.pdf`.

[43] Peter Senger. Status of the Compressed Baryonic Matter experiment at FAIR. *International Journal of Modern Physics E*, 29(02):2030001, 2020.

[44] Peter Senger and Volker Friese. CBM progress report 2020. 2021. doi: 10.15120/GSI-2021-00421.

[45] Peter Senger and Volker Friese. CBM progress report 2021. 2022. doi: 10.15120/GSI-2022-00599.

[46] Cahit Uğur, Grzegorz Korcyl, Jan Michel, Manuel Penschuk, and Michael Traxler. 264 channel tdc platform applying 65 channel high precision (7.2 psrms) fpga based tdcs. In *2013 IEEE Nordic-Mediterranean Workshop on Time-to-Digital Converters (NoMe TDC)*, pages 1–5. IEEE, 2013.

[47] Bronkhorst Mess und Regeltechnik. Funktionsprinzip der Constant Temperature Anemometry. `https://www.bronkhorst.com/de-de/service-und-support/theorien-und-technologien/thermischer-massendurchflusssensor-fur-gase-inline-cta-prinzip/`. online; last retrieved on 2023/10/19.

[48] Adrian Amatus Weber. Development of readout electronics for the RICH detector in the HADES and CBM experiments-HADES RICH upgrade, mRICH detector construction and analysis. Technical report, HADES, 2021.

[49] David C Wilcox. Formulation of the kw turbulence model revisited. *AIAA journal*, 46(11):2823–2838, 2008.

[50] Anthony G Wright. *The photomultiplier handbook*. Oxford University Press, 2017.

Acknowledgements

To conclude this work, I would like to mention all the people, without whom this thesis would not even exist as it is.

First of all, I would like to express my deepest appreciation for *Prof. Dr. Karl-Heinz Kampert* for giving me the opportunity to write the thesis in his beautiful working group. I would also like to thank *Prof. Dr. Christian Zeitnitz* for being my second referee.

Words cannot express my gratitude to my supervisor *Dr. Christian Pauly* for his invaluable patience and feedback, with which he provided me with expertise and knowledge. Without him I could not have undertaken this endeavour. Special thanks also to *Dr. Jörg Förtsch*, who always had an open ear for me, answering every question and stimulating interesting discussions. Furthermore, I would be remiss if I did not mention *Dennis Pfeifer* who helped me with a lot of things throughout the thesis, from working on the simulations to providing technical and engineering support for the experimental setup.

I am also grateful to all my colleagues of the Astroparticle group, especially to all members of the CBM/HADES group: Simon, Tetiana, Pavish, Sukyung and Jesus. Thank you for pleasant conversations in the office and for the wonderful and funny time we had at the Collaboration Meeting and at the DPG Spring Meeting. I also had the pleasure of working with *Fabian* and *Alex*, who I have known best from the first day in this group and who have also helped me with many things as well.

I would like to thank all my friends who accompanied me on this journey and without whom it would only have been half as fun and bearable, especially emphasizing *Max*, *Marvin*, *Samuel*, *Max* and *Maurice*.

Ringrazio infinitamente mia madre *Josiane*, mio padre *Antonio* e mia sorella *Maria*, senza i loro insegnamenti e senza il loro supporto, questo lavoro di tesi non esisterrebbe nemmeno. Grazie per essermi stato accanto, sostenendomi ed incoraggiandomi a raggiungere questo immenso traguardo.

Declaration of Authorship / Eidesstattliche Erklärung

according to §15(6) of the examination regulations of 11/25/2019
gem. §15 Abs. 6 der Prüfungsordnung vom 25.11.2019

Surname (Name), First name (Vorname): Boccarella, Gianluca

English

I hereby declare in lieu of oath that the thesis submitted is my own unaided work. All direct or indirect sources used are acknowledged as references.

This thesis was not previously presented to another examination board and has not been published.

I hereby also agree that my thesis (Master's thesis) may be made available for inspection by academically interested persons or institutions and within the framework of external quality assurance measures of the degree programme. Correction or evaluation notes in my thesis may not be quoted.

Deutsch

Hiermit versichere ich an Eides Statt, die vorliegende Arbeit selbstständig und unter ausschließlicher Verwendung der angegebenen Literatur und Hilfsmittel erstellt zu haben, sowie Zitate kenntlich gemacht habe.

Die Arbeit wurde bisher in gleicher oder ähnlicher Form keiner anderen Prüfungsbehörde vorgelegt und auch nicht veröffentlicht.

Hiermit erkläre ich mich auch damit einverstanden, dass meine Abschlussarbeit (Master-Thesis) wissenschaftlich interessierten Personen oder Institutionen und im Rahmen von externen Qualitätssicherungsmaßnahmen des Studienganges zur Einsichtnahme zur Verfügung gestellt werden kann. Korrektur- oder Bewertungshinweise in meiner Arbeit dürfen nicht zitiert werden.

Wuppertal, den ________________ ____

(Gianluca Boccarella)